DOE-ER-0313/53
Distribution
Categories
UC-423, -424

FUSION MATERIALS SEMIANNUAL PROGRESS REPORT FOR THE PERIOD ENDING

December 31, 2012

Prepared for
DOE Office of Fusion Energy Sciences
(AT 60 20 10 0)

DATE PUBLISHED: April 2013

Prepared by
OAK RIDGE NATIONAL LABORATORY
Oak Ridge, Tennessee 37831
Managed by
UT-Battelle, LLC
For the
U.S. DEPARTMENT OF ENERGY

FOREWORD

This is the fifty-third in a series of semiannual technical progress reports on fusion materials science activity supported by the Fusion Energy Sciences Program of the U.S. Department of Energy. It covers the period ending December 31, 2012. This report focuses on research addressing the effects on materials properties and performance of exposure to the neutronic, thermal and chemical environments anticipated in the chambers of fusion experiments and energy systems. This research is a major element of the national effort to establish the materials knowledge base for an economically and environmentally attractive fusion energy source. Research activities on issues related to the interaction of materials with plasmas are reported separately.

The results reported are the products of a national effort involving a number of national laboratories and universities. A large fraction of this work, particularly in relation to fission reactor irradiations, is carried out collaboratively with partners in Japan, Russia, and the European Union. The purpose of this series of reports is to provide a working technical record for the use of program participants, and to provide a means of communicating the efforts of fusion materials scientists to the broader fusion community, both nationally and worldwide.

This report has been compiled under the guidance of F. W. (Bill) Wiffen and Betty Waddell, Oak Ridge National Laboratory. Their efforts, and the efforts of the many persons who made technical contributions, are gratefully acknowledged.

Peter J. Pappano
Research Division
Office of Fusion Energy Sciences

TABLE OF CONTENTS

1. FERRITIC/MARTENSITIC STEEL DEVELOPMENT

1.1 Stability of Nanoprecipitates in Fe-Base Model Alloys — 1
L. Tan, Y. Katoh, and L. L. Snead (Oak Ridge National Laboratory)

The stability of VN, TaC, and TaN under thermal, stress, and radiation conditions is being investigated. Isothermal aging experiments at 600 and 700°C for 100, 1000, and 5000 h have been completed. VN and TaC showed similar resistance to thermal aging at 600 and 700°C. TaC may be slightly more resistant. Further study is in progress including TaN particles. The samples have been subjected to creep tests at 600°C and 170 MPa for TaC and TaN and 100 MPa for VN. Unlike VN and TaC, TaN was not resistant to the creep, which was broken into small pieces. Irradiation experiments, using Fe^{2+} ions at 500°C for 20 and 200 dpa and neutron at 300, 500, and 650°C for up to about 20 dpa, are in progress. Post-irradiation examination will be pursued.

1.2 Recent Observations of Helium Effects on Cavity Evolution in Tempered Martensitic Steels and Nanostructured Ferritic Alloys — 5
G. R. Odette, T. Yamamoto, and Y. Wu (University of California - Santa Barbara), S. Kondo and A. Kimura (Kyoto University)

Additional dual ion (Fe^{3+} and He^+) beam irradiation (DII) was performed at 500°C on previously irradiated alloys up to a nominal dpa and He levels of 80 dpa and ≈ 3400 appm, respectively. The irradiations were performed at dual ion beam facility, DuET, located at Kyoto University in Japan. The actual dpa, He and He/dpa vary with depth in the sample. The alloys studied include a normalized and tempered martensitic steel, (TMS) F82H mod.3 and a nanostructured ferritic alloy (NFA), MA957. TEM observations have been performed at a location where total dpa and He levels are estimated to be ≈ 220 dpa and ≈ 3400 appm He. These same locations had been previously irradiated to ≈ 70 dpa and ≈ 900 appm He. Cavity evolutions during the incremental irradiation were distinctly different in the two alloys. In F82H the number density of the cavities (N) remained at ≈ $5 \times 10^{22}/m^3$ while average diameter (d) of all cavities grew from 3.5 to 4.9 nm, with corresponding increases in the void fraction of cavities from 67 to 87% (defined as d > 2 nm) and in growth of the average d of voids (d_v) from 3.9 to 5.3 nm. The cavity volume fraction (f) in F82H increased from 0.23% to 0.43%. In the case of MA957, the number density of the cavities increased by about a factor of 4 reaching $N \approx 4.4 \times 10^{23}/m^3$; this is very similar to the typical number density of nm-scale oxide features in the alloy. The average d of cavities in MA957 also increased from 1.38 to 1.80 nm, including 22% that are larger than 2 nm. However, it is not known if these cavities are bubbles or voids. The cavity f in MA957 increased from 0.016% to 0.16%. Note the highest dpa and He irradiation conditions exceed the end of life conditions of even an aggressive fusion demonstration reactor.

TABLE OF CONTENTS

2. ODS AND NANOCOMPOSITED ALLOY DEVELOPMENT

See also Sections 1.2 and 8.3.

2.1 **Development of ODS FeCrAl for Fusion Reactor Applications** — 10
B. A. Pint, D. T. Hoelzer, D. Shin, J. O. Kiggans, Jr., and K. A. Unocic (Oak Ridge National Laboratory)

Capsule testing was completed on six cast FeCrAl alloys for 1,000h at 700°C. The alloys with 3%Al all showed mass losses similar to 9Cr steel under these conditions while those with 5%Al all showed little or no mass gain. In all cases, a LiAlO2 reaction product formed but it was thinner for the 3%Al alloys and the surface was rougher. For the oxide stability, the thermodynamic model of HfO2 -Y2 O3 was combined with the other two constituent pseudo-binaries of Al2 O3 -Y2 O3 and Al2 O3 -HfO2. Isothermal and isoplethal data from the experimentally assessed phase diagram of Al2 O3 -Y2 O3 -HfO2 were used to adjust the ternary model parameters. Diffusion couple experiments at 1250° and 1650°C showed that Ti was very reactive with Al2 O3 and Y2 O3. Much less reaction occurred with HfO2 and ZrO2.

2.2 **Characterization of 14W NFA Micro-Alloyed with Y, Ti, Hf, and Zr** — 16
Y. Wu, V. Ravula and G. R. Odette (University of California - Santa Barbara)

Nanostructured ferritic alloys (NFAs) have applications in advanced fission and fusion reactors and are strengthened and made irradiation tolerant by a high number density of Y-Ti-O nanofeatures (NFs) that are very stable up to 1000ºC [1]. We briefly report preliminary results on the effects of various additions of Y, Ti, Hf and Zr to a baseline NFA composition of 14Cr, 3W and 0.3 Y_2O_3 (wt.%) on the microstructure and strength of NFAs. These alloys were characterized by microhardness (µH) and transmission electron microscopy (TEM) measurements. Alloys with additions of Ti (≈ 0.47 at.%) plus Hf (≈ 0.13 at.%) or Y(≈ 0.25 at%) had the highest µH and smallest grain sizes after hot consolidation at 1150°C. The corresponding hardness was lower in alloys alloyed with Zr (≈ 0.25 at. %) and Ti. The µH was lowest in alloys with Hf and Zr but without Ti; Hf again resulted in higher µH in this case than Zr. The alloy alloyed with Hf but without Ti had larger grains than those alloyed with either Hf or Y and Ti.

The alloys with Ti and Hf or Y added had extremely small grain sizes, especially for the consolidation temperature of 1150°C. The average NF size (<d>), number density (N) and volume fraction (f) ranged from 2.8 to 3.9 nm, 1.3 to $1.7 \times 10^{23}/m^3$ and 0.7 to 1.8 %, respectively. The NF oxides appear to be consistent with pyrochlore structures observed in reference NFA MA957, which are Y_2Ti_2O7 in this case. The NFs in alloys without Ti appear to contain large quantities of Cr.

TABLE OF CONTENTS

2.3 Characterization of the Final Precursor Alloy to a Larger Best Practice Heat of 14YWT — **21**
N. J. Cunningham, Y. Wu, G. R. Odette, D. Gragg, and K. Fields (University of California - Santa Barbara), D. T. Hoelzer (Oak Ridge National Laboratory), S. A. Maloy (Los Alamos National Laboratory)

We describe our characterization of a new, extruded and cross-rolled nanostructured ferritic alloy (NFA) designated 14YWT-PM2 (PM2). Atomized Fe14Cr powders containing Y, Ti, and W were milled for 40 h with FeO, extruded at 850°C, and cross-rolled at 1000°C. The consolidated alloy was characterized by transmission electron microscopy (TEM) and atom probe tomography (APT), as well as by various mechanical property tests. A summary of the TEM, APT, and mechanical testing results are shown in Table 1. PM2 contains a high number density of N = $8.4 \pm 2.6 \times 10^{23}$ m^{-3}, small <d> = 1.75 ± 0.35 nm Y-Ti-O nanofeatures (NFs). The balance of the microstructure consists of: a) a fine, nearly unimodal size distribution of grains with approximately equiaxed cross sections, that are moderately extended in the extrusion direction, with an average effective diameter $d_g \approx 424$ nm; and, b) a high dislocation density of $r \approx 1.2 \times 10^{15} m^{-2}$. Larger Ti oxi-nitride precipitate phases are also observed. The corresponding μH = 401±15 kg/mm^2, is consistent with yield and ultimate strengths of 1125 and 1298 MPa, respectively. The cleavage fracture toughness of PM2 increases in the temperature regime from ≈ -200 to -100°C up to a ductile tearing upper shelf transition at ≈ 80 MPa√m. A limited number of strain rate jump creep tests also showed high strength, comparable to that of the strongest NFA, in spite of the formation of edge cracks and possible necking during loading.

In addition, milled powders annealed at 850ºC, 1000ºC, and 1150ºC were characterized by small angle neutron scattering (SANS) and TEM. They also contained a high number density of NFs with increasing <d> and decreasing (N) and volume fraction (f) with increasing temperature.

3. CERAMIC COMPOSITE STRUCTURAL MATERIAL DEVELOPMENT

See also Sections 8.1 and 8.2.

3.1 Determination of Interfacial Mechanical Properties of Ceramic Composites by the Compression of Micro-Pillar Test Specimens — **34**
C. Shih, Y. Katoh, K. J. Leonard, H. Bei, and E. Lara-Curzio (Oak Ridge National Laboratory)

The interfacial debond shear strength and the coefficient of internal friction between the fiber and pyrocarbon interface of a SiC fiber reinforced CVI SiC matrix composite are determined using a novel method, which involves micro compression of micro sized pillars containing an inclined fiber/matrix interface. The interfacial debonds shear strength and the coefficient of internal friction was determined to be 100 MPa and 0.73, respectively. This new test method with simple geometry showed high data reproducibility; moreover, the results fit the proposed Coulomb fracture criterion well. The determined interfacial properties are compared with those determined from fiber push out tests.

TABLE OF CONTENTS

3.2 **Process Development and Optimization for Silicon Carbide Joining and Irradiation Studies** — 42
T. Cheng, J. O. Kiggans, Jr., Y. Katoh, and L. L. Snead (Oak Ridge National Laboratory)

The candidate joint materials for the ongoing work to evaluate the neutron irradiation effects on chemically vapor-deposited (CVD) SiC includes bonds produced by the NITE (nano-infiltration and transient eutectic-phase) – like transient eutectic phase processes, diffusion bonding utilizing active titanium or molybdenum inserts, calcia-alumina (CA) glass/ceramics, and Ti-Si-C MAX phase through displacement reaction. During the present reporting period, joint specimens were successfully produced through the active metal insert methods and the NITE-like process, and then evaluated for as-fabricated properties.

4.0 **HIGH HEAT FLUX MATERIALS AND COMPONENT TESTING**

4.1 **High-Heat Flux Testing Using Plasma Arc Lamps of Low-Level Irradiated Materials** — 55
A. S. Sabau, E. Ohriner, Y. Katoh, and L. L. Snead (Oak Ridge National Laboratory)

The high-heat flux testing facility using Plasma Arc Lamps was demonstrated at ORNL for W samples during a visit of the Japanese delegation of a PHENIX planning workshop. The second generation test section, which was designed by taking into account safety and materials compatibility requirements in order to handle the testing of low levels irradiated tungsten articles, was fabricated. The test sections were assembled and all the steps during the high heat flux runs were tested, including the air evacuation, backfill with Ar, and Ar pressure monitoring during the high heat flux testing, demonstrating the readiness of the new facility for irradiated samples.

4.2 **Effect of Ti and TiC Additives on Sintering Behavior of Nano W** — 60
X. Wang and Z. Zak Fang (University of Utah)

Ti and TiC were added as grain growth inhibitors during sintering of nano W alloys. The sintering of nano W, W-1Ti, W-1Ti-0.5TiC, W-1TiC powders were investigated to understand the effect of Ti and TiC addition on grain growth and densification. The results show that both Ti and TiC can effectively prevent W grain growth during sintering. However, the additives also adversely affect densification. The combinations of Ti and TiC appear to have promise to be used for achieving high density while retaining nanoscale grain size.

TABLE OF CONTENTS

5. MAGNET AND DIAGNOSTIC SYSTEM MATERIALS

TABLE OF CONTENTS

HfO_2/SiO_2 and Al_2O_3/SiO_2 mirrors. At the time of this writing, irradiation capsules have completed $1x10^{21}$ and $4x10^{21}$ n/cm^2 (E>0.1 MeV) exposures at 448 K, corresponding to approximately 1 and 4 displacements per atom (dpa). Post irradiation examination of the high dose mirrors will begin at the start of 2013.

6. FUSION CORROSION AND COMPATIBILITY SCIENCE

Additional results are presented on the characterization of a dual layer (Y2 O3 /V) MHD coating exposed to flowing Li at ~688°C. This coating was exposed at the highest temperature and had the largest volume of a “new” phase formed at the V-4Cr-4Ti substrate-Y2 O3 interface. Extensive analytical transmission electron microscopy has not definitively identified the phase, partly because it is unstable under the electron beam. However, it is assumed to be LiYO2 that formed due to Li ingress along the substrate-V overlay coating interface.

Isothermal capsule experiments were completed on coated and uncoated Grade 92 (9Cr-2W) specimens for 5,000 h in Pb-Li to determine the long-term stability of the coating at 600° and 700°C. Thin ~50**μ** m Alrich diffusion coatings showed similar low mass changes at both temperatures. However, extensive Al loss was observed after 5,000h at 700°C. In contrast, a thicker diffusion coating where intermetallic aluminide phases formed showed a mass loss after 5,000h at 700°C due to partial spallation of the aluminide coating outer layer. Characterization of the 5,000h specimens is still in progress. These results indicate that (1) Al-rich coatings greatly reduce dissolution at 700°C in Pb-Li but do not prevent it and (2) the effectiveness of coating strategies to improve compatibility are limited. In order to further evaluate the coating concept and wrought and oxide dispersion strengthened (ODS) FeCrAl alloys, plans are being made to build a Pb-Li thermal convection loop of Fe-9Cr or FeCrAl tubing.

7. MECHANISMS AND ANALYSIS

A large series of molecular dynamics simulations have been completed to map out the pressure-temperature relationship for helium in iron to provide the basis for fitting of a new equation of state for helium bubbles. The behavior of helium is described by the three-body Fe-He potential developed at ORNL under the fusion program.

TABLE OF CONTENTS

TABLE OF CONTENTS

longer propagation ranges expected from the nonlinear theory and demonstrated experimentally [8, 9]. This points to the necessity of the modification of the chemical rate theory to account for the quodon-induced energy deposition to the reaction area. Accordingly, the rate theory of microstructure evolution in solids has been modified to account for the production of Schottky defects at surfaces of extended defects due to their interaction with the radiation-induced lattice excitations [3, 5-8]. The modified theory predictions include important phenomena, which have not been properly understood before, such as irradiation creep [5, 6], radiation-induced annealing of voids [3, 7], saturation of void growth under high dose irradiation and void lattice formation [8].

8. MODELING PROCESSES IN FUSION SYSTEM MATERIALS

A set of atomic displacement cascades was simulated using popular SiC Tersoff interatomic potentials. The types of created defects and their dynamics were analyzed. The validity of existing interatomic potentials was investigated by comparison of typical point defect diffusion barriers obtained using these potentials with first principles results.

The study, measurement, prediction, and control of thermal conductivity of SiC/SiC composites are a critical issue for Fusion. Both high conductivity (first wall) and reduced conductivity (flow channel insert) materials appear to be required for specific fusion reactor applications so that low-activation goals are achieved. This study has applied an Eshelby-Mori-Tanaka approach (EMTA) implemented in PNNL EMTA software to predict thermal conductivities of SiC/SiC composites. The EMTA homogenization procedure is structured in three steps to capture the effects of the constituent materials including the fiber-coating layer on the thermal conductivities of the as-formed composites. The results show that when perfectly bonded to the fibers a thicker fiber coating layer with higher thermal conductivity than that of the fibers leads to increased thermal conductivities for the composite. EMTA can be effectively used to identify the interfacial thermal conductance by correlating the EMTA predicted thermal conductivities with the measured values. A reverse engineering procedure in EMTA is useful to determine the thermal conductivities of the constituents if the actual measured values are not available or is unknown.

Nanostructured ferritic alloys (NFAs) have applications in advanced fission and fusion reactors and are strengthened by a high number density of Y-Ti-O nanofeatures (NFs) that

TABLE OF CONTENTS

are very stable up to 1000ºC [1]. Previously reported long and short-term aging studies from between 800ºC and 1400ºC on NFA MA957 for times up to 32.4 kh were used to develop a coarsening model in the form:

$$[d(t)^p - d_o^p] = [k_p(T)t]$$

Here t is the aging time and d is the average NF diameter starting at d_o. Simple models predict p ranging from 2 to 5, depending on the operative coarsening mechanism. Our data is most consistent with a pipe diffusion mechanism (p=5) [2]. However, a least square fit of all the data gives a higher p values of 6.26, possibly suggesting that combinations of complex phenomena operate during aging; for example, rather than random pipe diffusion processes, coarsening and other stages of NF evolution may involve highly correlated multispecies mechanisms.

In this short report we present TEM data for 1000ºC aging to 21.9 kh that provides strong support for pipe diffusion coarsening (p = 5), since most of the NFs are associated with dislocations. Additional aging studies at intermediate temperatures (1075ºC to 1200ºC) and times (<10 kh) are underway to help more accurately identify the coarsening mechanisms and kinetics.

9. IRRADIATION METHODS, EXPERIMENTS, AND SCHEDULES

The impact of He and H transmutation products on material damage from 14.1 MeV neutrons is a critical unresolved issue which is being addressed by combining numerical models and specialized ion and neutron irradiation experiments. Because of the uncertainties associated with both modeling and ion irradiation experiments, there is a clear need for an accessible irradiation facility that can provide near prototypic levels of transmuted helium and hydrogen. The scientific understanding obtained would also enable more effective use of a future large-volume fusion engineering irradiation facility (such as IFMIF) when it becomes available.

A design study [1,2,3] for a fusion materials irradiation test station (FMITS) for installation at the Spallation Neutron Source (SNS) has been completed. Samples would be located within two horizontal tubes in front of the mercury target. For these specimen locations, the back-scattering neutron flux spectra should be close to the ITER fusion spectrum. The PKA spectra at the FMITS samples were also compared to those for ITER, and the results show good agreement. Material damage rates would be 1.6–5.5 dpa/yr for steel, and 1.8–3.4 dpa/yr for SiC.

1.1 Stability of Nanoprecipitates in Fe-Base Model Alloys — L. Tan, Y. Katoh, L. L. Snead (Oak Ridge National Laboratory)

OBJECTIVE

Study the stability of MX-type nanoprecipitates in reduced-activation ferritic (RAF) steels using Fe-base model alloys under thermal, stress, and radiation conditions to help understanding the failure mechanisms of RAF steels and identify prominent strengthening particles for advanced RAF steel development.

SUMMARY

The stability of VN, TaC, and TaN under thermal, stress, and radiation conditions is being investigated. Isothermal aging experiments at 600 and 700°C for 100, 1000, and 5000 h have been completed. VN and TaC showed similar resistance to thermal aging at 600 and 700°C. TaC may be slightly more resistant. Further study is in progress including TaN particles. The samples have been subjected to creep tests at 600°C and 170 MPa for TaC and TaN and 100 MPa for VN. Unlike VN and TaC, TaN was not resistant to the creep, which was broken into small pieces. Irradiation experiments, using Fe^{2+} ions at 500°C for 20 and 200 dpa and neutron at 300, 500, and 650°C for up to about 20 dpa, are in progress. Post-irradiation examination will be pursued.

PROGRESS AND STATUS

Introduction

MX-type precipitates have shown excellent coarsening resistance compared to Laves phase and chromium-rich $M_{23}C_6$ in 9-12% Cr ferritic-martensitic steels. They are critical for high temperature strength of this class of steels. Recently, however, limited data have shown the instability of MX, e.g., VN, TaC, and TaN, at elevated temperatures and irradiation conditions [1-3].

Experimental Procedure

Three model alloys, Fe-1WVN, Fe-1WTaC, and Fe-1WTaN, had been designed and procured. The alloys have been confirmed having VN, TaC, and TaN in nanometers respectively. Type SS-3 specimens were used in isothermal aging experiments and creep tests. The specimens were sealed in helium filled quartz tubes and isothermally aged at 600 and 700°C for 100, 1000, and 5000 h. Creep tests were conducted at 600°C using constant loads of ~70% of the yield stress of the alloys. Specimens were also prepared for Fe^{2+} ions and neutron irradiation experiments. The microstructural evolution of the nanoprecipitates was primarily characterized using transmission electron microscopy (TEM).

RESULTS

The isothermal aging experiments at 600 and 700°C h for up to 5000 h have been completed. Most of samples have been characterized except for a few aged samples of Fe-1WTaN. Using Fe-1WVN alloy as an example, Figure 1 shows bright-field and dark-field TEM images of the samples in the control, 600°C for 5,000 h and 700°C for 1,000 h aged conditions. Statistical measurements indicate that the density of VN was slightly increased (~11%) with some decrease in particle size after 5,000 h aging at 600°C. In contrast, the particles were significantly refined with a noticeable increase in density after aging at 700°C for 1,000 h, which suggest the occurrence of dissolution and/or precipitation at this temperature. The sample aged at 700°C for 5,000 h is being prepared for TEM characterization. The results are expected to provide more insights on the particle stability. No significant changes were observed for TaC aged at 600°C for 5,000 h. However, the 700°C aging for 1,000 h also exhibited some refinement of TaC particles.

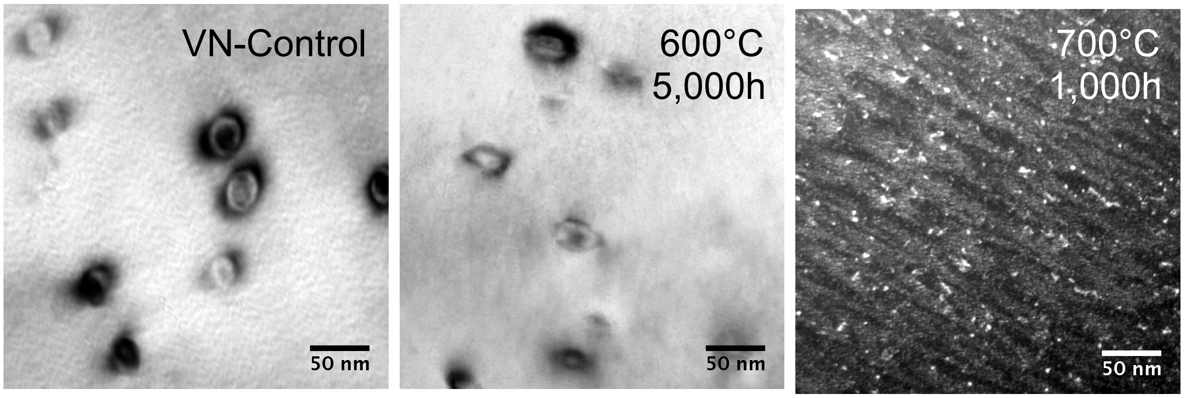

Figure 1. Bright-field (BF) and dark-field (DF) TEM images showing the evolution of VN nanoprecipitates under thermal aging at 600 and 700°C.

Creep tests have been completed at 600°C with a load of ~70% yield stress for the alloys. Figure 2(a) shows the creep life of the tested samples compared to the literature date of F82H [4]. Despite the low alloy of Fe-1W base metal, the Fe-1WTaC exhibited creep life (~371 h) closing to F82H. The Fe-1WVN showed the least creep resistance in the three alloys. The order of creep resistance of the alloys is consistent with the corresponding particle volume fraction in the alloys as shown in Figure 2(b). The larger volume fraction of TaC benefited the higher strength and greater creep life of Fe-1WTaC compared to the TaN and VN bearing alloys.

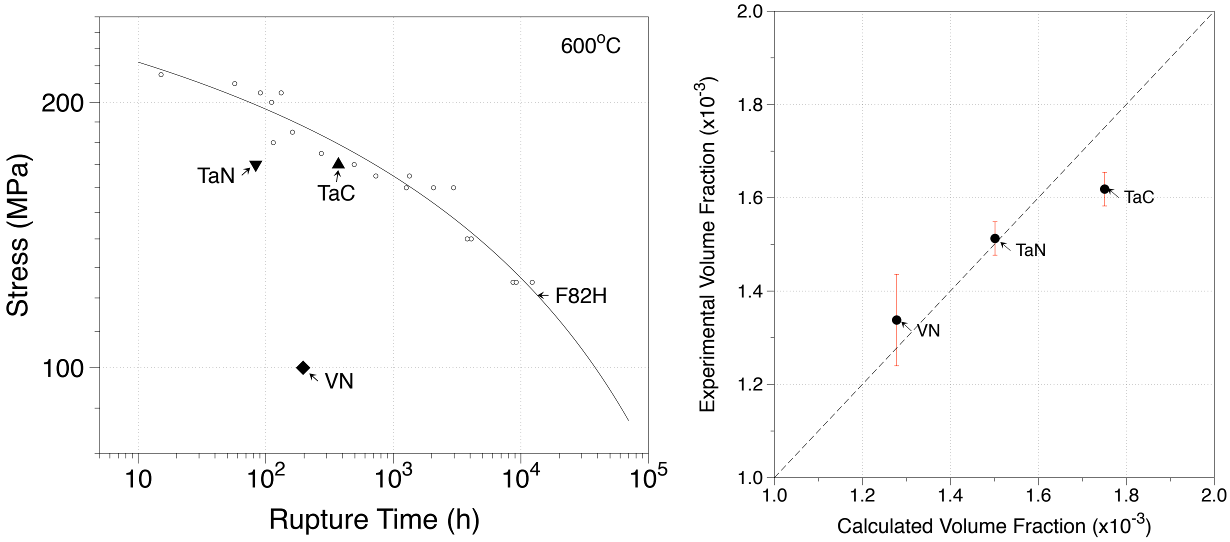

Figure 2. (a – left) Creep rupture time of alloys Fe-1WTaC, Fe-1WTaN, and Fe-1WVN compared to literature data of F82H; (b – right) Calculated and experimental volume fraction of TaC, TaN, and VN precipitates in alloys Fe-1WTaC, Fe-1WTaN, and Fe-1WVN, respectively.

Microstructural characterization indicated that the stress in the gauge section of the creep samples did not result in significant changes to the size/shape of VN and TaC particles. In contrast, the TaN particles were broken into small pieces under the stress of 170 MPa. Additionally, a few Fe_2W-type Laves phase particles with a size of ~100 nm were observed at grain boundaries in the gauge section of the creep ruptured Fe-1WTaC sample, which were not observed in the “unstressed” tab section of the creep sample. In comparison, Laves phase in a size of ~30 nm was found at grain boundaries in the Fe-1WTaC sample aged at 600°C for 1,000 h. The results suggest that the formation of the Laves phase was greatly accelerated by the stress during creep.

Fe^{2+} ion irradiation of the alloy samples has completed 20 dpa at 500°C at University of Michigan. The ion-irradiated samples have been received at ORNL and are ready for TEM specimen preparation using focused-ion-beam (FIB). The 200 dpa irradiation at 500°C is in progress. Additionally, a set of type SS-J2 specimens of the alloys has being neutron-irradiated, using HFIR at ORNL, at 300, 500, and 650°C to damage levels ranging from ~0.1 dpa to ~20 dpa. Post-irradiation examination including tensile tests at room temperature and selected TEM characterization will be pursued.

REFERENCES

[1] M. Tamura, H. Sakasegawa, A. Kohyama, H. Esaka, and K. Shinozuka, *J. Nucl. Mater.* **329** (2004) 328.

[2] A. Kabadwal, M. Tamura, K. Shinozuka, and H. Esaka, *Metall. Mater. Trans. A* **41** (2010) 364.

[3] H. Sakasegawa, et. al., “Microstructural changes of finely dispersed MX precipitates in ion-irradiated ferritic heat–resistant steels,” presented in the Conference of Japan Institute of Metals, Sept. 22-24, 2001.

[4] N. Yamanouchi, M. Tamura, H. Hayakawa, A. Hishinuma, and T. Kondo, *J. Nucl. Mater*. **191** (1992) 822.

1.2 Recent Observations of Helium Effects on Cavity Evolution in Tempered Martensitic Steels and Nanostructured Ferritic Alloys — G. R. Odette, T. Yamamoto, Y. Wu (University of California Santa Barbara), S. Kondo, A. Kimura (Kyoto University)

OBJECTIVE

The objective of this work is to characterize cavity evolution under Fe^{3+} and He^{+} dual ion beam irradiation in a normalized and tempered martensitic steel (TMS) F82H mod.3 and a nanostructured ferritic alloy (NFA), MA957.

SUMMARY

Additional dual ion (Fe^{3+} and He^{+}) beam irradiation (DII) was performed at 500°C on previously irradiated alloys up to a nominal dpa and He levels of 80 dpa and ≈ 3400 appm, respectively. The irradiations were performed at dual ion beam facility, DuET, located at Kyoto University in Japan. The actual dpa, He and He/dpa vary with depth in the sample. The alloys studied include normalized and tempered martensitic steel, (TMS) F82H mod.3 and a nanostructured ferritic alloy (NFA), MA957. TEM observations have been performed at a location where total dpa and He levels are estimated to be ≈ 220 dpa and ≈ 3400 appm He. These same locations had been previously irradiated to ≈ 70 dpa and ≈ 900 appm He. Cavity evolutions during the incremental irradiation were distinctly different in the two alloys. In F82H the number density of the cavities (N) remained at ≈ 5 x $10^{22}/m^3$ while average diameter (d) of all cavities grew from 3.5 to 4.9 nm, with corresponding increases in the void fraction of cavities from 67 to 87% (defined as d > 2 nm) and in growth of the average d of voids (d_v) from 3.9 to 5.3 nm. The cavity volume fraction (f) in F82H increased from 0.23% to 0.43%. In the case of MA957, the number density of the cavities increased by about a factor of 4 reaching N ≈ 4.4 x $10^{23}/m^3$; this is very similar to the typical number density of nm-scale oxide features in the alloy. The average d of cavities in MA957 also increased from 1.38 to 1.80 nm, including 22% that are larger than 2 nm. However, it is not known if these cavities are bubbles or voids. The cavity f in MA957 increased from 0.016% to 0.16%. Note the highest dpa and He irradiation conditions exceed the end of life conditions of even an aggressive fusion demonstration reactor.

BACKGROUND

Predicting and mitigating the effects of a combination of large levels of transmutant He and displacement damage (dpa), produced by high energy neutrons, on the dimensional stability and mechanical properties of structural materials is one of the key challenges in the development of fusion energy [1]. The fundamental overriding questions about He-dpa synergisms include: a) what are the basic interacting mechanisms controlling He and defect transport, fate and consequences, and how are they influenced by the starting microstructure and irradiation variables (dpa rate, He/dpa ratio, temperature and applied stress) and, b) how can the detrimental effects of He-dpa synergisms be mitigated and managed by proper microstructural design? In the absence of a fusion neutron source, we have been utilizing various alternative experimental techniques to study the He-dpa synergisms, that includes: a) in situ He implantation (ISHI) in mixed spectrum fission reactors, HFIR at ORNL and ATR at INL; b) spallation proton irradiation (SPI) in STIP (spallation target irradiation projects) at Paul Sherr Institute in Switzerland; and, c) multiple ion beams to simultaneously implant He and create displacement damage with heavy ions, specifically using dual ion beam irradiation (DII) facility, DuET at Kyoto University, Japan. The DII produces a broad range of dpa and He up to very high levels in short periods of time. However, great caution is required in applying DII data to neutron irradiation conditions due to a host of differences including dpa rates, the proximity of a free surface and injected interstitials and impurities in some cases. Nevertheless, DII are useful for mechanism studies and it is important to compare and contrast DII microstructural evolutions with the corresponding effects of neutron irradiations. Here we report the results of DII up to high dpa at different He/dpa ratios, based on re-irradiation of previously irradiated F82H and MA957 specimens.

PROGRESS AND STATUS

Experimental Procedure

The alloys studied here are a TMS F82H mod.3 and a NFA MA957. These alloys were previously irradiated in DuET to the nominal displacement damage and He levels of 25 dpa and 1000 appm at 500°C [2]. The original specimens were in the form of electro-polished 3 mm diameter disks that had been mechanically ground to a nominal thickness of 200 μm. The discs were slightly trimmed so that the larger target areas of the two alloys can be placed closer together to allow efficient use of ion beams. The DII was performed in DuET facility in the Institute of Advanced Energy, Kyoto University (Kyoto, Japan), where Fe^{3+} ions are accelerated to 6.4MeV by a tandem accelerator and He^{+} ions are accelerated to 1MeV by a single end accelerator. The specimens were positioned in a temperature-monitored/controlled stage. The He^{+} ion beam was passed through a rotating beam energy degrader creating four ion implantation energy bands that result in a broader and more uniform He deposition profile up to a maximum depth of ≈ 1500 nm. Re-irradiation was carried out to nominal additions of 57 dpa and 2900 appm He to the original 25 dpa and 1000 appm He, resulting in a nominal 82 dpa and 3900 appm He at 600 nm from the sample surface. An FEI HELIOS Focused Ion Beam (FIB) tool was used to micro-machine < 100 nm thick electron transparent ≈ 5 μm wide and 5 μm deep lift-outs that included both damaged-implanted and undamaged regions. TEM was performed on the FEI 200 keV Technai T20 and 300 KeV Titan instruments in the UCSB Microstructure and Microanalysis Facility. In this report we focus the microstructure evolution at the depth ranging from 1300 to 1400 nm from the irradiation surface, focus on regions with He (appm)/dpa ratios ≥ 50, 10 to 30 and < 10. The lower He/dpa regions where estimated damage and He conditions are ≈ 70 dpa and ≈ 900 appm, respectively, after the original irradiation, reach up to ≈ 220 dpa and ≈ 3400 appm after the re-irradiation.

RESULTS

Cavity Microstructures Before and After DI Re-irradiation at 500°C

Figures 1a-b show the TEM images for F82H mod.3 irradiated to (a) before and (b) after the re-irradiation, respectively. The images are at the depth from 1300, at the top end of the images, to 1400 nm, at the bottom, from the irradiation surface. Both images show clear bimodal distribution of cavities consisting of small bubbles and large voids. Figures 2a-b show the corresponding set of images for MA957 before and after the re-irradiation.

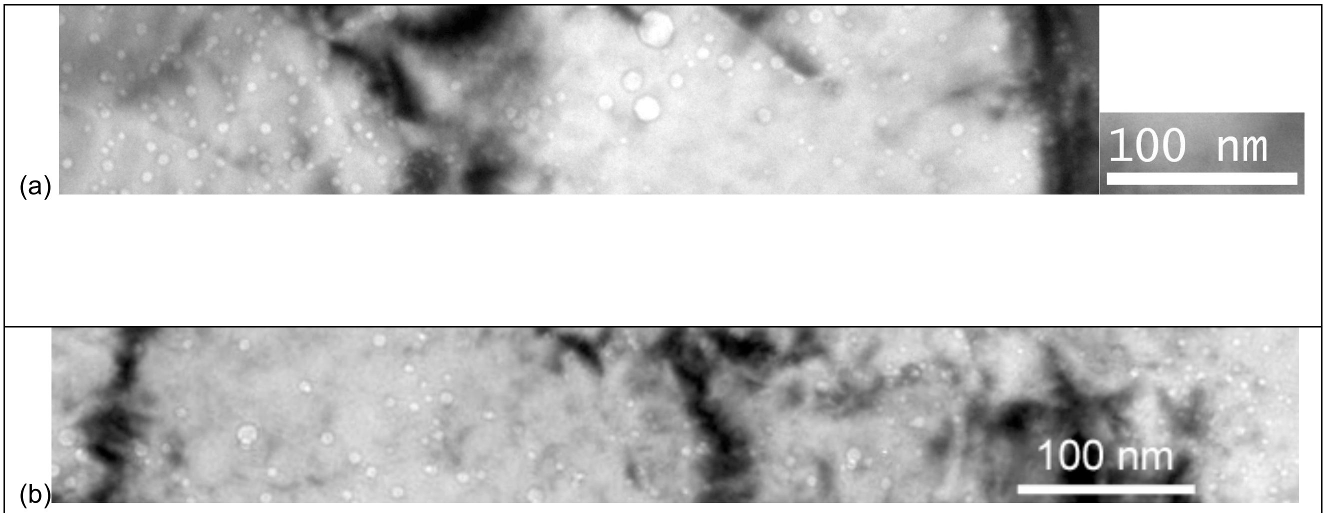

Figure 1. Under-focused bright field TEM images for the cavity microstructures in F82H mod.3 after DII to (a) ≈ 70 dpa and ≈ 900 appm He, and (b) ≈ 220 dpa and ≈ 3400 appm He.

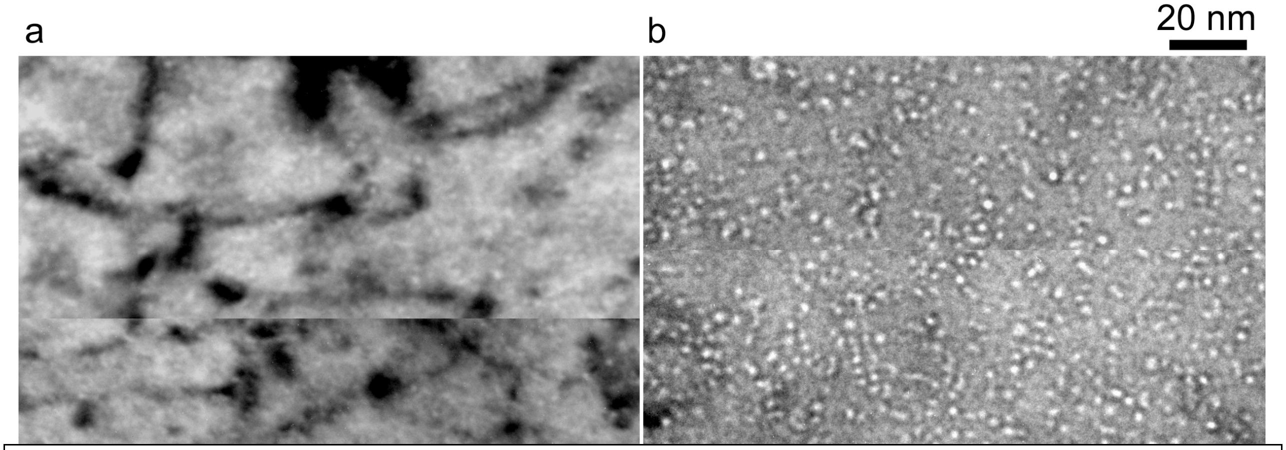

Figure 2. Under-focused bright field TEM images for the cavity microstructures in MA957 after DII to (a) ≈ 70 dpa and ≈ 900 appm He, and (b) ≈ 220 dpa and ≈ 3400 appm He.

Table 1. Detailed quantitative analyses of the cavity structures have shown that

F82H Condition			MA957 Condition	
68 dpa 970 appm	216 dpa 3400 appm		68 dpa 970 appm	216 dpa 3400 appm
3.46	4.87	Average size of all cavities <d> (nm)	1.38	1.80
4.6	5.1	Number density N (m^{-3})	11	44
3.9	5.3	Average size of voids $\langle d_v \rangle$ (nm)	______	2.5
67	87	Fraction of void cavities (%)	0	?
0.23	0.43	Volume fraction of cavities f (%)	0.016	0.16

Figure 3 shows the evolutions of: a) average cavity d; b) N; and, c) f as a function of dpa for F82H. Figure 4 shows the corresponding plots for MA957.

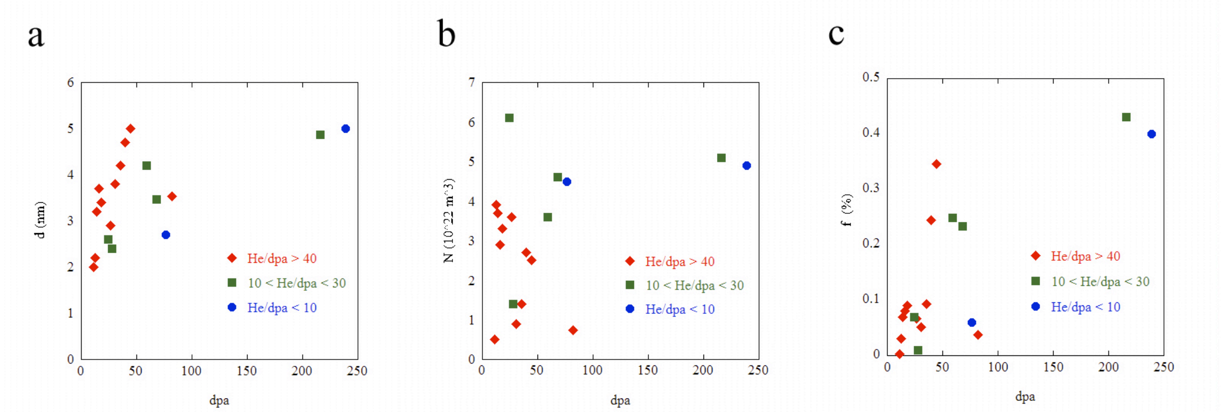

Figure 3. a) Average cavity d; b) N; and, c) f as a function of dpa for F82H.

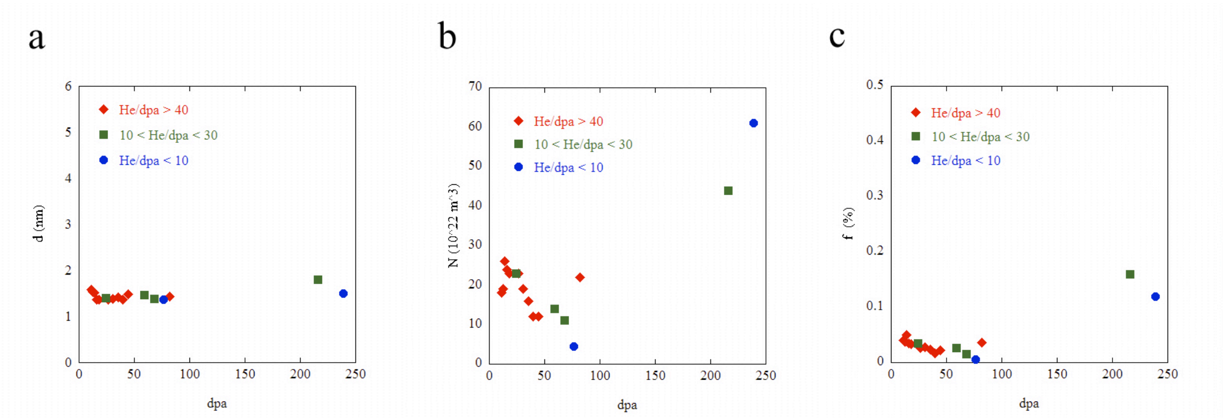

Figure 4. a) Average cavity d; b) N; and, c) f as a function of dpa for MA957.

DISCUSSION

The major, and perhaps surprising, result is that the cavity volume fraction (f) is so low in both alloys even at very high He and dpa levels. Except for on anomalous data point it appears that higher He/dpa ratios shift the f-curves to lower dpa. Clearly the cavities are smaller and more numerous in the NFA and the net swelling is lower. Further analysis will be provided in the future.

FUTURE WORK

This is ongoing very high priority research.

ACKNOWLEDGEMENTS

The DII were conducted as a part of the TITAN program for US DOE- Japan MEXT collaboration for fusion energy research. The work performed at UCSB was supported by the U. S. Department of Energy, Office of Fusion Energy Sciences, under contract DE-FG03-94ER54275. We acknowledge the contributions of the NSF sponsored UCSB Microstructure and Microanalysis Facility.

REFERENCES

[1] Y. Dai, G. R. Odette, and T. Yamamoto, The Effects of helium on irradiated structural alloys, in Comprehensive Nuclear Materials, R. Konings, T. R. Allen, R. E. Stoller, and S. Yamanaka editors (2012) Elsevier.

[2] T. Yamamoto, Y. Wu, G. R. Odette, K. Yabuuchi, S. Kondo, and A. Kimura, Dual Ion Beam Irradiation Studies of Cavity Evolution in a Tempered Martensitic Steel and Nanostructure Ferritic Alloys, Fusion Materials Semiannual Report 6/30/2012, DOE/ER-0313/52 (2012) 8.

2.1 **Development of ODS FeCrAl for Fusion Reactor Applications** — B. A. Pint, D. T. Hoelzer, D. Shin, J. O. Kiggans and K. A. Unocic (Oak Ridge National Laboratory)

OBJECTIVE

The dual coolant lead-lithium (DCLL) blanket concept requires improved Pb-Li compatibility with ferritic steels in order to demonstrate viable blanket operation in a DEMO-type fusion reactor. The goal of this work is to develop an oxide dispersion strengthened (ODS) alloy with improved compatibility with Pb-Li and excellent mechanical properties. The current focus is determining the desired Cr and Al contents in the alloy and the minor additions to form a stable oxide dispersion for this application. The Cr and Al content effect is being investigated using model cast FeCrAl alloys and the oxide stability is being investigated using a combination of computation and diffusion couples.

SUMMARY

Capsule testing was completed on six cast FeCrAl alloys for 1,000h at 700°C. The alloys with 3%Al all showed mass losses similar to 9Cr steel under these conditions while those with 5%Al all showed little or no mass gain. In all cases, a $LiAlO_2$ reaction product formed but it was thinner for the 3%Al alloys and the surface was rougher. For the oxide stability, the thermodynamic model of HfO_2-Y_2O_3 was combined with the other two constituent pseudo-binaries of Al_2O_3-Y_2O_3 and Al_2O_3-HfO_2. Isothermal and isoplethal data from the experimentally assessed phase diagram of Al_2O_3-Y_2O_3-HfO_2 were used to adjust the ternary model parameters. Diffusion couple experiments at 1250° and 1650°C showed that Ti was very reactive with Al_2O_3 and Y_2O_3. Much less reaction occurred with HfO_2 and ZrO_2.

PROGRESS AND STATUS

Introduction

The DCLL blanket concept (Pb-Li and He coolants) is the leading U.S. design for a test blanket module (TBM) for ITER and for a DEMO-type fusion reactor.[1] With reduced activation ferritic-martensitic (FM) steel as the structural material, the DCLL is limited to ~475°C metal temperature because Fe and Cr readily dissolve in Pb-Li above 500°C and Eurofer 97 plugged a Pb-Li loop at 550°C.[2-3] For a higher temperature blanket for DEMO, structural materials with enhanced creep and compatibility are needed. ODS FeCrAl alloys are one possibility to meet this objective and considerable research on ODS FeCr alloys has shown an excellent combination of creep strength and radiation resistance.[4-7] Isothermal compatibility tests have shown low mass losses at up to 800°C.[8] Therefore, a materials development effort is underway, specific to this application. The first steps are to identify the Cr and Al contents needed for good Pb-Li compatibility and to identify stable oxide dispersions for a FeCrAl matrix.

Experimental Procedure

Static capsule tests were performed using Mo (inert to Pb-Li) inner capsules and type 304 stainless steel (SS) outer capsules to protect the inner capsule from oxidation. The uncoated cast FeCrAlY specimens were ~1.5 mm thick and 4-5 cm^2 in surface area with a 600 grit surface finish and were held with 1 mm diameter Mo wire. The capsules were loaded with 125g of Pb-Li in an Ar-filled glove box. The Pb-Li was melted and cast at ORNL and had Li contents of 15.6-16.5 at%. The Mo and SS capsules were welded shut to prevent the uptake of impurities during the isothermal exposure. After exposure, residual Pb-Li on the specimen surface was removed by soaking in a 1:1:1 mixture of acetic acid, hydrogen peroxide and ethanol for up to 72 h. Mass change was measured with a Mettler-Toledo balance with an accuracy of 0.01 mg/cm^2. Post-test specimen surfaces were examined using x-ray diffraction (XRD), a Veeco Wyko optical profilometer and secondary electron microscopy (SEM) equipped with energy dispersive x-ray (EDX) analysis. After surface characterization, the specimens were metallographically sectioned and polished and examined by light microscopy.

A plate of high purity Al_2O_3 (99.8% purity) was obtained for preparation of samples to investigate the high temperature oxide phase reactions and stabilities. Slurries of TiO_2, ZrO_2, HfO_2 and Y_2O_3 were prepared for the diffusion couples. Samples were prepared by placing a row of the TiO_2, ZrO_2 and HfO_2 slurries on the Al_2O_3 plate and then dried. An additional row of Y_2O_3 slurry was placed next to the dried oxide slurries on each Al_2O_3 sample to produce samples of the three oxide ternary systems, Al_2O_3-Y_2O_3-HfO_2, Al_2O_3- Y_2O_3-ZrO_2, and Al_2O_3-Y_2O_3-TiO_2. Individual sections of each sample were annealed for 1h at 1250°C and 1650°C. After annealing, the microstructure was assessed using SEM and EDX analysis.

Results and Discussion

Figure 1a shows the mass change for the six cast FeCrAlY alloys after exposure to Pb-Li for 1,000h at 700°C. There was a distinct difference between the 3%Al and 5%Al alloys with minimal effect of the alloy Cr content. The results are shown in Figure 1b as a function of the alloy Cr and Al contents and the next series of experiments are shown to fill in the gap. Lower Cr contents are desired to avoid issues with embrittlement,[9,10] especially under irradiation. This is driving the focus for the next series of experiments. Figure 2 shows cross-sections from the exposed specimens. In each case, XRD indicated that the surface oxide was $LiAlO_2$, consistent with earlier results.[8,11] The oxide appeared to be slightly thinner on the 3%Al alloys. Based on the undulations in the surfaces, the roughness was measured on the specimens and was somewhat rougher on the 3%Al alloys compared to the 5%Al alloys. Concentration profiles in the substrate beneath the surface oxide will be performed in the future.

Compared to the highly stable Y-Ti-O nano-oxide dispersion in Fe-(9-14)Cr,[6] the Al addition presents serious challenges to the choice of oxide dispersion since Al_2O_3 is thermodynamically more stable than TiO_2 and readily reacts with Y_2O_3 to form a number of stable compounds. Ideally, another addition would react with Y_2O_3 to form a nano-dispersion in FeCrAl. Thus, understanding the high-temperature stability of the oxide dispersion in the presence of Al is important for developing ODS FeCrAl. A self-consistent model for Al_2O_3-Y_2O_3-ZrO_2 was obtained from the literature, so the computational work focused on the

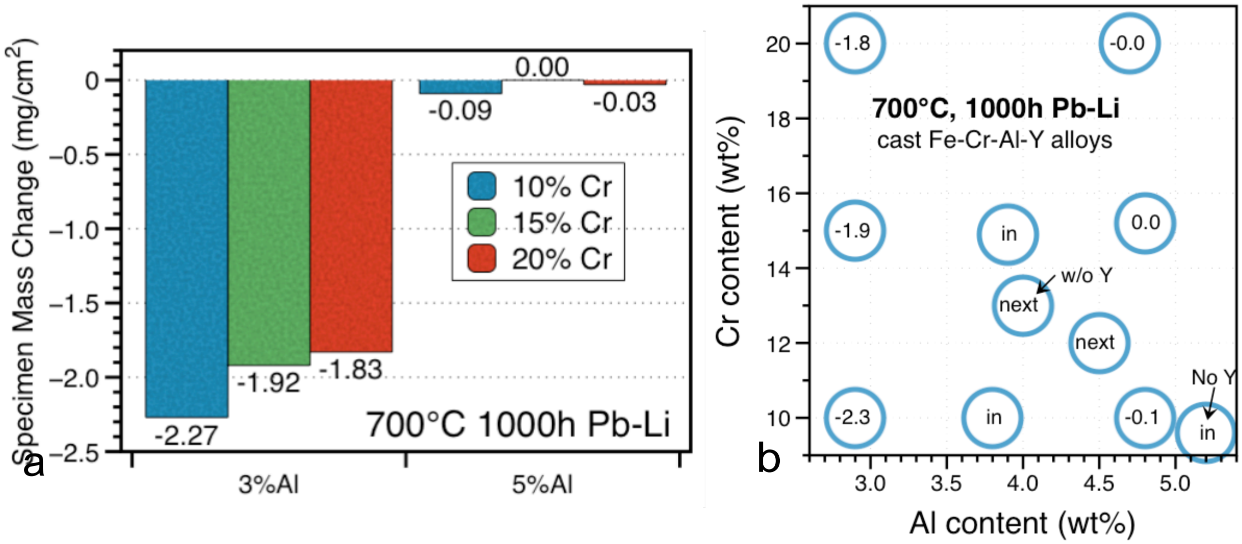

Figure 1. Specimen mass change is shown (a) for the cast FeCrAlY alloys after exposure to Pb-Li for 1,000h at 700°C and (b) as a function of the Cr and Al contents with the next experiments noted.

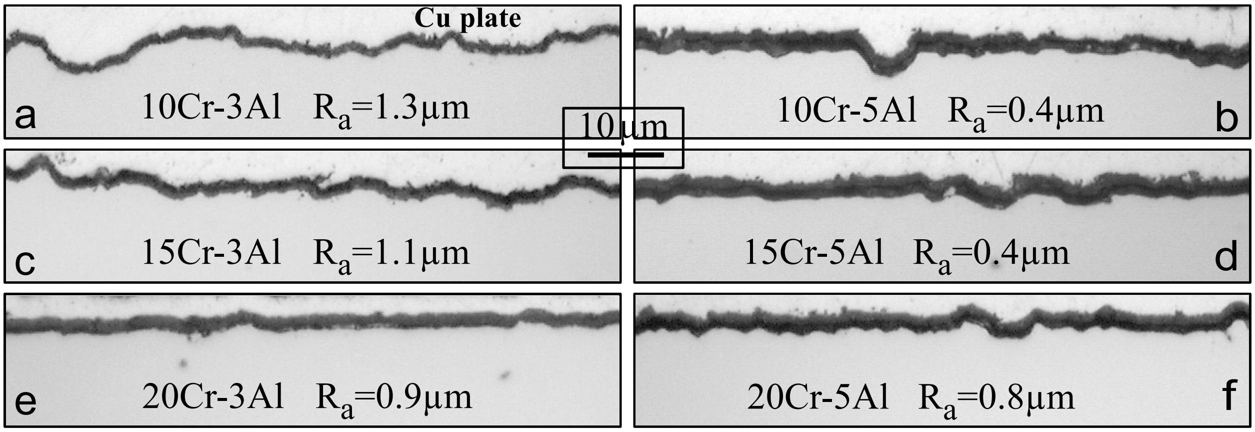

Figure 2. Polished cross-sections of cast FeCrAl alloys after 1000h at 700°C in Pb-Li.

Al_2O_3-Y_2O_3-HfO_2 system where there was disagreement between the experimental and predicted phase diagrams.[12,13] A model for a constituent pseudo-binary HfO_2-Y_2O_3 in Al_2O_3-Y_2O_3-HfO_2 was updated to compare with reported ternary isothermal phase equilibrium data and phase fractions at 1650°C from the Al_2O_3-Y_2O_3 equi-concentration to pure ZrO_2 and HfO_2 were obtained. Figure 3 shows ternary and psuedo-binary diagrams at 1650°C for the Al_2O_3-Y_2O_3-HfO_2 system. The binary diagram is from the dashed line in Figure 3a.

For validation, diffusion couples were annealed at 1250° and 1650°C. Figure 4 shows the couples annealed for 1h at 1650°C. At both temperatures, Al_2O_3 and Y_2O_3 reacted to form a 50-60μm layer. By far, TiO_2 was the most reactive with Al_2O_3, diffusing millimeters into the substrate, Figure 4. Both ZrO_2 and HfO_2 were more stable, with limited solubility in Al_2O_3 and <1μm thick reaction layer at 1650°C.

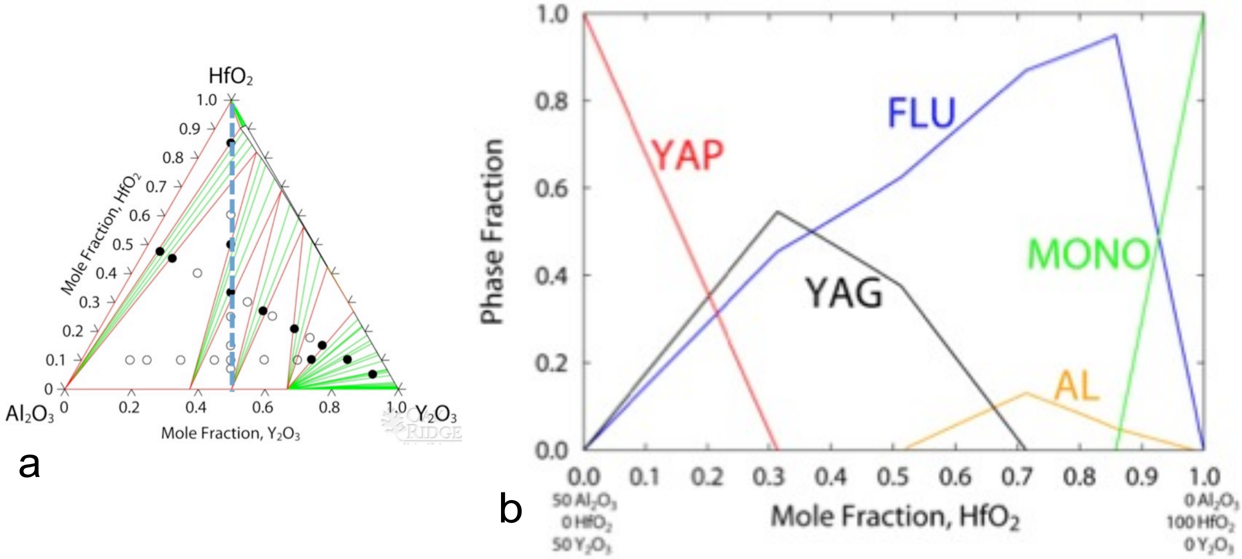

Figure 3. (a) Ternary and (b) pseudo-binary diagrams at 1650°C calculated for the Al_2O_3-Y_2O_3-HfO_2 showing YAP ($YAlO_3$), YAG ($Y_3Al_5O_{12}$), FLU (flourite), AL (Al_2O_3) and MONO (monoclinic) phases.

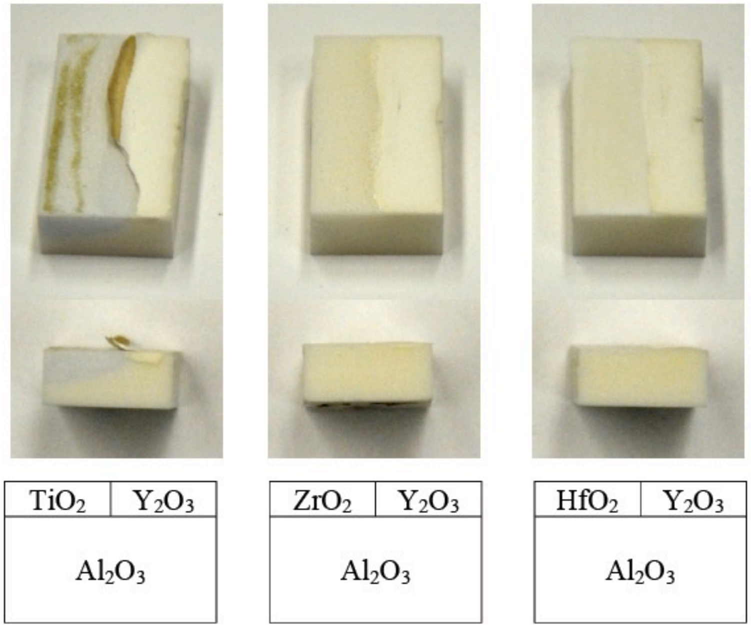

Figure 4. Three diffusion couple annealed for 1h at 1650°C.

Figure 5 shows EDS analysis of the Al_2O_3-Y_2O_3-HfO_2 and Al_2O_3-Y_2O_3-ZrO_2 couples annealed at 1650°C. In the reaction zone in each case, there appears to be less Hf present in the Y_2O_3 phase while Zr appeared to form a complex $(Al,Y,Zr)O_x$ phase, Figure 5b. However, both Hf and Zr are more soluble in FeCrAl than Y [14] and therefore may coarsen more readily during processing or high temperature exposure.

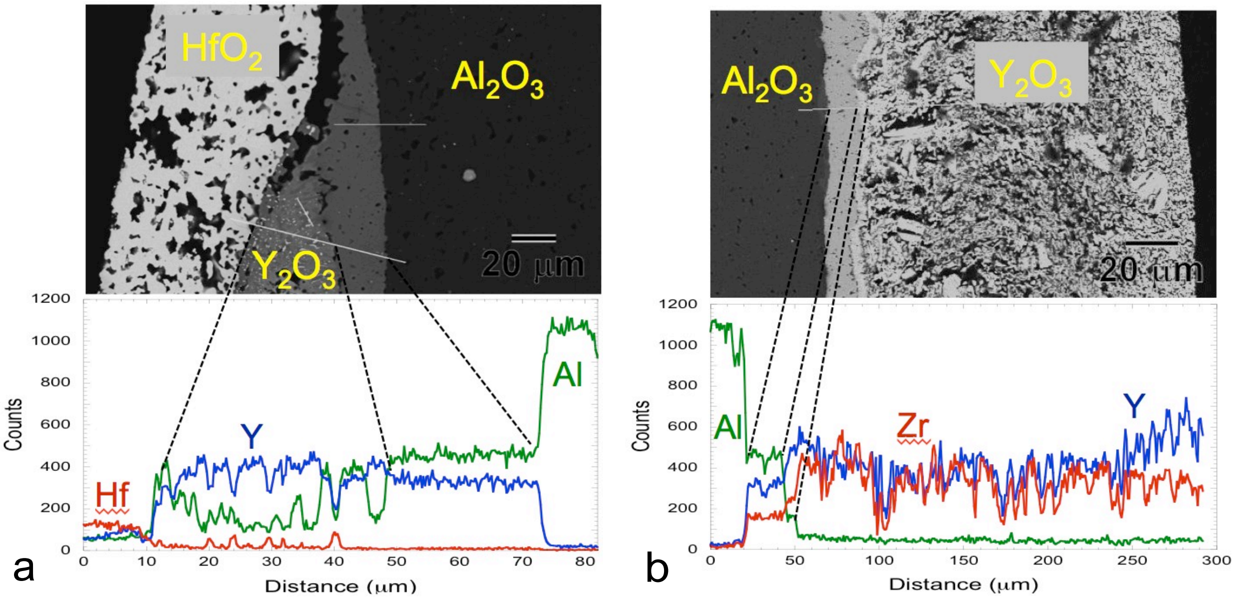

Figure 4. SEM images and EDS profiles for diffusion couples after 1h at 1650°C (a) Al_2O_3-Y_2O_3-HfO_2 and (b) Al_2O_3-Y_2O_3-ZrO_2.

REFERENCES

[1] M. Abdou, D. Sze, C. Wong, M. Sawan, A. Ying, N. B. Morley and S. Malang, *Fus. Sci. Tech*. **47** (2005) 475.

[2] O. K. Chopra, D. L. Smith, P. F. Tortorelli, J. H. DeVan and D. K. Sze, *Fusion Technol*. **8** (1985) 1956.

[3] J. Konys, W. Krauss, J. Novotny, H. Steiner, Z. Voss and O. Wedemeyer, *J. Nucl. Mater.* **386-88** (2009) 678.

[4] S. Ukai and M. Fujiwara, *J. Nucl. Mater.* **307** (2002) 749.

[5] G. R. Romanowski, L. L. Snead, R. L. Klueh, and D. T. Hoelzer, *J. Nucl. Mater*. **283-287** (2000) 642.

[6] R. L. Klueh, J. P. Shingledecker, R. W. Swindeman, and D. T. Hoelzer, *J. Nucl. Mater.* **341** (2005) 103.

[7] D. A. McClintock, M. A. Sokolov, D. T. Hoelzer and R. K. Nanstad, *J. Nucl. Mater*. **392** (2009) 353.

[8] B. A. Pint, L. R. Walker, and K. A. Unocic, *Mater. High Temp.* **29** (2012) 129.

[9] P. J. Grobner, *Metal. Trans.* **4** (1973) 251.

[10] S. Kobayashia and T. Takasugi, *Scripta Materialia* **63** (2010) 1104–1107.

[11] B. A. Pint and K. L. More, *J. Nucl. Mater.* **376** (2008) 108.

[12] S.M. Lakiza et al., *J. Euro. Cer. Soc.* **31** (2011) 1285.

[13] O. Fabrichnaya and C. Mercer, *CALPHAD* **29** (2005) 239

[14] B. A. Pint, *J. Am. Ceram. Soc.* **86** (2003) 686.

2.2 Characterization of 14W NFA Micro-alloyed with Y, Ti, Hf and Zr — Y. Wu, V. Ravula[1] and G. R. Odette (University of California, Santa Barbara)

OBJECTIVE

The objective of this work was to explore alternative composition variants for nanostructured ferritic alloys (NFA).

SUMMARY

Nanostructured ferritic alloys (NFAs) have applications in advanced fission and fusion reactors and are strengthened and made irradiation tolerant by a high number density of Y-Ti-O nanofeatures (NFs) that are very stable up to 1000ºC [1]. We briefly report preliminary results on the effects of various additions of Y, Ti, Hf and Zr to a baseline NFA composition of 14Cr, 3W and 0.3 Y_2O_3 (wt.%) on the microstructure and strength of NFAs. These alloys were characterized by microhardness (μH) and transmission electron microscopy (TEM) measurements. Alloys with additions of Ti (≈ 0.47 at.%) plus Hf (≈ 0.13 at.%) or Y(≈ 0.25 at%) had the highest μH and smallest grain sizes after hot consolidation at 1150°C. The corresponding hardness was lower in alloys alloyed with Zr (≈ 0.25 at. %) and Ti. The μH was lowest in alloys with Hf and Zr but without Ti; Hf again resulted in higher μH in this case than Zr. The alloy alloyed with Hf but without Ti had larger grains than those alloyed with either Hf or Y and Ti.

The alloys with Ti and Hf or Y added had extremely small grain sizes, especially for the consolidation temperature of 1150°C. The average NF size (<d>), number density (N) and volume fraction (f) ranged from 2.8 to 3.9 nm, 1.3 to $1.7 \times 10^{23}/m^3$ and 0.7 to 1.8 %, respectively. The NF oxides appear to be consistent with pyrochlore structures observed in reference NFA MA957, which are Y_2Ti_2O7 in this case. The NFs in alloys without Ti appear to contain large quantities of Cr.

BACKGROUND

To date most NFA have been based on micro-alloying Fe-(12-16)Cr-(2-3)W base alloys with small amounts of Y_2O_3 and Ti (< 1%). However, some researchers have explored the use of Hf and Zr which share Group V with Ti [see Ref. 2 as an example]. Thus as part of his work during a 6 month visit to UCSB, Dr. Vijay Ravula from the International Advanced Research Centre for Powder Metallurgy and New Materials (ARCI) in Hyderabad, India, prepared a number of small batch heats of NFA to explore the relative effects of Hf, Zr, Ti and additional Y to a standard base of a 14YWT NFA. Here we report some results of initial characterization studies of these alloys.

---

[1] Permanent Address: International Advanced Research Centre for Powder Metallurgy and New Materials (ARCI), Hyderabad, India

PROGRESS AND STATUS

Experimental Procedure

We fabricated 6 small alloy heats by mechanical alloying with SPEX ball milling for 20h the extra constituents shown in Table 1 (wt. %) with rapidly solidified Fe-14Cr-3W powders with and without Ti (0 and 0.4 wt.%) designated as 14YW and 14YWT, followed by hot pressing at 1150°C for 3 h at 1.3 MPa. Note, an initial study of an alloy with Ti and Hf additions based on milling for 10 h did not completely succeed in fully mixing the solutes, although this may be partly due to problems with the SPEX shaker mill motor at that time. The alloys are labeled as YWXX, where the last letter(s) designate the solute(s) that were added (T = Ti, H = Hf, Z = Zr, Y = Y_2O_3),

Vickers μH measurements were carried out at a load of 500 g on all the alloys. TEM specimen lift-outs were prepared using a FEI Helios FIB. A final lift out cleaning step used a low energy 2 KV, 5.5 pA beam to minimizing gallium ion damage. Small oxides were also extracted on a carbon foil for TEM EDX analysis. The TEM was performed using FEI Titan at 300 kV equipped with energy dispersive X-ray (EDX) spectrometer on YWTH, YWTY and YWH. Further details can be found in [3].

RESULTS

The μH results are shown in Table 1. Table 2 summarizes the TEM observations in terms of the NF oxide number density, N ($10^{23}/m^2$), average diameter. <d> (nm), and volume fraction, f (%), along with the μH and average grain diameter, d_g (nm) of the three alloys examined.

Table 1 Alloy Compositions (wt. %) and μH (kg/mm^2).

Alloy ID	14YWT	14YW	Zr	Hf	Y	Y_2O_3	μH
YWTH	99.93	-	-	0.4	-	0.3	522
YWH	-	99.93	-	0.4	-	0.3	455
YWTZ	99.93	-	0.4	-	-	0.3	425
YWZ	-	99.93	0.4	0.4	-	0.3	415
YWTZH	99.89	-	0.4	0.4	-	0.3	522
YWTY	99.93	-	-	-	0.2	0.3	533

Table 2. Hardness and TEM Data for Three Alloys.

Alloy	μH [kg/mm2]	N (×$10^{23}/m^2$)	<d> (nm)	f (%)	d_g (nm)
YWTH	522	1.3	3.4	0.7	150
YWH	455	1.5	3.9	1.4	525
YWTY	533	1.7	2.8	1.8	132

The grain structures of YWTH, YWTY, and YWH are shown in Figure 4. The alloys that contain both Ti and either Hf or Y additions have remarkably small grain sizes of less than 150 nm, especially considering the consolidation temperature of 1150°C. There are also small grains in the YWH alloy without Ti, but in this case the average is size ≈ 3.5 to 4 times higher than for the

Ti alloyed heats. Small grains certainly contribute to the higher strength of the YWTH and YWTY alloys [4].

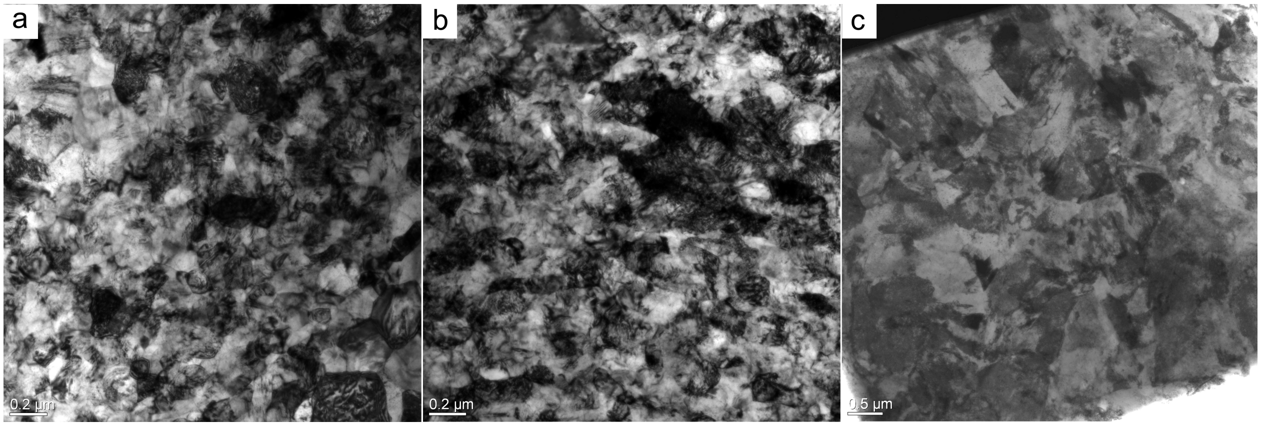

Figure 1. Lower magnification images show the grains in: a) YWTH; b) YWTY; and, c) YWH.

As shown in the extraction replica micrographs in Figure 2, small NF oxides were found in both YWH and YWTH. However, the <d> of the NFs in YWTH is slightly less than that in YWH, reflecting the well known refining effect of Ti [1]. However, the variations in N and <d> are relatively modest for all 3 alloys. The NF f varies from 0.7 to 1.8%. The nominal f is largest in the YWTY alloy with the highest Y + Hf + Ti solute content (≈ 1.1 at.%), but was smallest in the YWTH alloy with an intermediate solute content (≈ 0.98 at.%). The large f in the lowest solute content YWH alloy (0≈0.26 at. %) is not understood; and it is not clear that is consistent with a solute mass balance without the inclusion of a large fraction of Cr (see below).

Figure 3 shows a HRTEM images of small NF in YWTH (a) and the corresponding FFFT diffraction pattern (b) that is consistent with an fcc pyrochlore-type $Y_2Ti_2O_7$ complex oxide structure (b). Table 3 shows the corresponding lattice d-spacings taken from SAD ring patterns for the extracted NF oxides for YWH and YWZ are also consistent with $Y_2Ti_2O_7$, suggesting that he are $Y_2Hf_2O_7$ and $Y_2Zr_2O_7$ in YWH and YWZ, respectively.

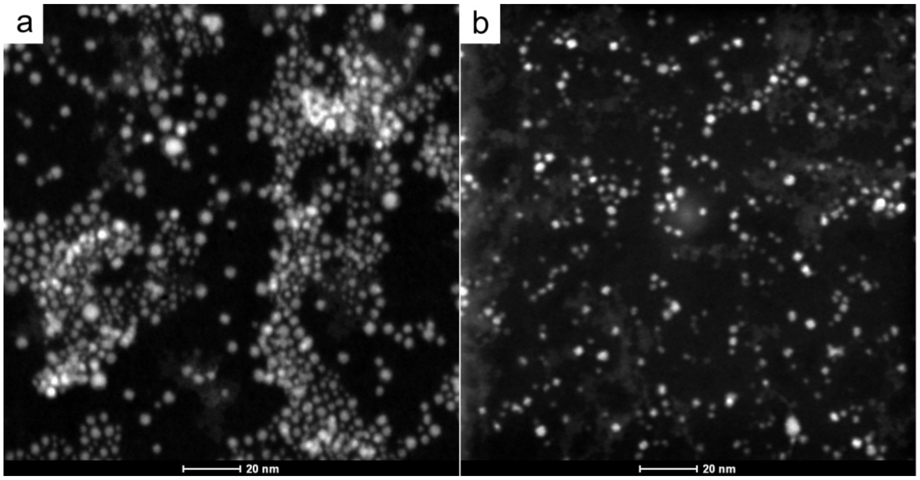

Figure 2. HAADF STEM images showing the NF oxides extracted from: a) YWH; and, b) YWTH.

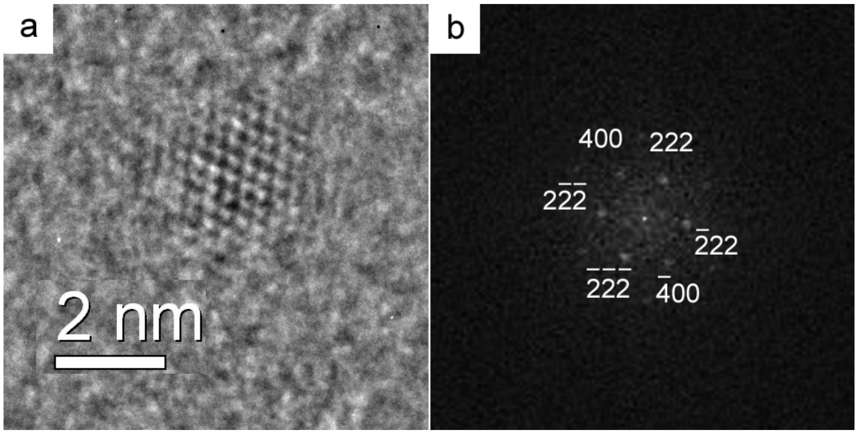

Figure 3. A HRTEM image of a small NF oxide (~2 nm in diameter) extracted on carbon film (a), and the corresponding FFT power spectra (b).

Table 3 gives a summary of d spacings measured from selected area diffraction (SAD) ring patterns (not shown here) in YWH and YWZ. Table 4 shows the results of EDX measurements on small the extracted NF oxides. The alloys without Ti appear to contain a large amount of Cr. Additional measurements will be needed to see is this observation is quantitatively correct; or perhaps partly an artifact of the extraction process. The nominal Zr/Y is ≈ 2.3 and the Hf/Y ≈ 1.2 in the YWZ and YWH alloys respectively. The Cr content of the alloy alloyed with Ti, Y and Hf is much lower; the corresponding Y/Ti = 1, but the Hf/Y and Ti is high at ≈ 4.7. A tentative conclusion is that the NFs are perhaps $(Y,Cr,Ti,Zr,Hf)_4O_7$ oxides, depending on the NFA composition.

Table 3. Measured d-spacings in Three NFA Compared to $Y_2Ti_2O_7$.

Lattice Spacing (Å)	YWZ	YWH	MA957	$Y_2Ti_2O_7$
d_{222}	3.05	3.05	3.0	2.93
d_{400} (Å)	2.60	2.65	2.6	2.56
d_{440} (Å)	1.80	1.8	1.8	1.80
d_{622} (Å)	1.60	1.6	1.6	1.54

Table 4. EDXS Measurements of the NF Compositions (at. %) for d<5 nm.

Alloys	Y	Ti	Hf	Zr	Cr
YWZ	17			39	44
YWH	16		19		65
YWTH	13	13	61		13

DISCUSSION AND FUTURE WORK

This exploratory study showed that alloying YW alloys with Hf and Zr, as well as Ti, would produce NFA and complex oxide NFs. However, the addition of Ti, along with the other Group IV elements resulted in higher alloy strength and smaller grains. Thus this preliminary research will continue. In the near term atom probe tomography (APT) and small angle neutron scattering (SANS) will be carried out on these and other new alloys prepared in the future.

REFERENCES

1. G. R. Odette, M. J. Alinger, and B. D. Wirth, *Annu. Rev. Mater. Res*. **38**, (2008) 472.
2. J. R. Rieken, I. E. Anderson, M. J. Kramer, G. R. Odette, E. Stergar and E. Haney, *J. Nucl. Mater.* **428** (2012) 65.
3. Y. Wu, E. M. Haney, N. J. Cunningham, and G. R. Odette, *Acta Mater.* **60** (2012) 3456.
4. Y. Wu, N. J. Cunningham, A. Etienne, E. Haney, G. R. Odette, et al., “The Effect of Bulk Oxygen Concentration on the Micro-nanostructure and Strength of a 14Cr Nanostructured Ferritic Alloy,” Fusion Reactor Materials Program DOE/ER-0313/50, Volume 50, pp. 47-57, June 30, 2011.

2.3 Characterization of the Final Precursor Alloy to a Larger Best Practice Heat of 14YWT[1]

— N. J. Cunningham, Y. Wu, G. R. Odette. D. Gragg, and K. Fields (University of California Santa Barbara) D. T. Hoelzer (Oak Ridge National Laboratory), S. A. Maloy (Los Alamos National Laboratory)

OBJECTIVES

The objective of this work was to characterize the alloy 14YWT-PM2, which is an extruded and cross-rolled precursor alloy to a large heat of 14YWT being produced using an alternative processing path that incorporates Y during gas atomization process.

SUMMARY

We describe our characterization of a new, extruded and cross-rolled nanostructured ferritic alloy (NFA) designated 14YWT-PM2 (PM2). Atomized Fe14Cr powders containing Y, Ti, and W were milled for 40 h with FeO, extruded at 850°C, and cross-rolled at 1000°C. The consolidated alloy was characterized by transmission electron microscopy (TEM) and atom probe tomography (APT), as well as by various mechanical property tests. A summary of the TEM, APT, mechanical testing results are shown in Table 1. PM2 contains a high number density of $N = 8.4 \pm 2.6 \times 10^{23}$ m^{-3}, small <d> = 1.75±0.35 nm Y-Ti-O nanofeatures (NFs). The balance of the microstructure consists of: a) a fine, nearly unimodal size distribution of grains with approximately equiaxed cross sections, that are moderately extended in the extrusion direction, with an average effective diameter $d_g \approx 424$ nm; and, b) a high dislocation density of $r \approx 1.2 \times 10^{15} m^{-2}$. Larger Ti oxi-nitride precipitate phases are also observed. The corresponding μH = 401±15 kg/mm^2, is consistent with yield and ultimate strengths of 1125 and 1298 MPa, respectively. The cleavage fracture toughness of PM2 increases in the temperature regime from ≈ -200 to -100°C up to a ductile tearing upper shelf transition at ≈ 80 MPa√m. A limited number of strain rate jump creep tests also showed high strength, comparable to that of the strongest NFA, in spite of the formation of edge cracks and possible necking during loading.

In addition, milled powders annealed at 850ºC, 1000ºC and 1150ºC were characterized by small angle neutron scattering (SANS) and TEM. They also contained a high number density of NFs with increasing <d> and decreasing (N) and volume fraction (f) with increasing temperature.

BACKGROUND

Nanostructured ferritic alloys (NFAs) have applications in advanced fission and fusion reactors and are strengthened and made irradiation tolerant by a high number density of thermally stable Y-Ti-O nanofeatures (NFs). The conventional NFA processing path uses ball milling to mechanically alloy Y_2O_3 in the Fe-Cr matrix, which is expensive and often leads to heterogeneous distributions of NFs. To overcome these challenges an alternative processing path in which Y is included in the melt prior to gas atomization and rapid solidification was developed in collaboration with partner institutions including Oak Ridge National Lab, Los Alamos National Lab, ATI Powder Metals, UC Berkeley and South Dakota School of Mines. Many small lab heats of NFA were prepared using this alternative processing method and

---

[1] This research was primarily sponsored by the DOE Office of Nuclear Energy under NEUP grants and a LLNL subcontract to UCSB. However, the FusMat program is using PM2 for various irradiation studies so it is appropriate to report these results in the a Fusion Semiannual Report.

analyzed in a program primarily funded by the DOE Office of Nuclear Energy [1]. The results of this extensive effort were used to identify the best processing practices. This preliminary work culminated in the final production of an extruded and hot, cross-rolled heat at ORNL known as 14YWT-PM2 (PM2). The following report describes the characterization of this new material.

STATUS AND PROGRESS

ATI Powder Metals (Pittsburgh, PA) produced the 14YWT atomized powders in its Laboratory Gas Atomizer (LGA) with a 27 kg (nominal) capacity vacuum induction melting (VIM) furnace lined with an alumina crucible. The crucible tilts to pour the melted alloy into a refractory tundish with a ceramic nozzle at the bottom. The combined effects of gravity and aspiration pressure deliver the melt through the nozzle to the gas atomization die in a close-coupled mode consisting of coaxial, co-directional supersonic gas flow to disrupt the stream of molten metal. Atomization breaks the melt stream into spheroidal droplets that solidify rapidly in an Ar or He atmospheres while moving through a stainless steel cooling tower. The objective is to solute trap Y in solution. Unfortunately this did not occur and the powder cellular solidification microstructure contained phase separated Y, mostly in ≈100 nm $Fe_{17}Y_2$ boundary precipitates or Y-rich precipitates within the grains. In addition, the large batch of powders prepared for subsequent industrial milling in greater quantities by Zoz Corporation in Germany, had a low O content, which was previously found to be inadequate to form fine dispersions of Y-Ti-O NFs [2]. Therefore, attritor ball milling was required both to adequately mix the Y and to add O. The PM2 powder was Zoz CM08 attritor milled at ORNL for 40 h with FeO (-10 mesh, Alpha Aesar, Part #30513) to increase the O content to ≈ 0.135 wt.%. The milling used 5 mm hardened steel balls at a ball to powder mass ratio of 10:1. The milling speed alternated between 900 (2 minutes) and 450 rpm (9 minutes). Care was used to limit O and N contamination from the atmosphere by better chamber sealing and evacuating and backfilling with Ar several times. The powders were then canned and degassed at 400ºC, hot extruded at 850º, annealed for 1 h at 1000ºC and hot cross-rolled to a ≈ 50% thickness of 5 mm. Optical microscopy, SANS, APT and TEM was performed on the extruded and cross-rolled alloy. The volume of available consolidated PM2 was approximately 14 cm^3, allowing for limited mechanical property measurements, including µH, tensile, strain rate jump creep and fracture testing.

Table 1. Summary of the PM2 characterization results.

NFs	
TEM <d> (nm) APT <d> (nm)	1.4 2.1
Average <d> (nm)	1.75±0.35
TEM N (10^{23} m^{-3}) APT N (10^{23} m^{-3})	5.8 11.0
Average N (10^{23} m^{-3})	8.4±2.6
TEM f (%) APT f (%)	0.07 0.47
Average f (%)	0.27±0.2
EDX Y/Ti	0.5 -1
APT Y/Ti/O	12/43/45
Other Microstructures	
Dislocation density (m^{-2})	$1.2 \times 10^{15} m^{-2}$
Average grain size	424 nm
Mechanical Properties	
μH (kg/mm^2)	401±15
Yield Stress, LX(MPa)	1125
Ultimate tensile stress, LX (MPa)	1298
Elongation to a load drop (%)	6
Total Elongation	11
Temperature ≈ half way between lower and upper shelf toughness (°C)	-170
LMP estimation of the stress at 750°C, for a 10^{-8}/s creep rate - axial/transverse (MPa)	310/260

Limited SANS and TEM studies were performed on milled powders annealed at 850, 1000 and 1150ºC for 3 h. The baseline anneals involved a 15ºC/min ramp to temperature and cooling, but one condition was an isotherm anneal at 1150ºC.

Microstructural Characterization

The TEM micrographs in Figures 1a and b show a moderately elongated grain structure in the extrusion direction, with an effective grain diameter of 424 nm. The SEM back-scattered images in Figures 1c and d show a more isotropic grain structure in the plane normal to the extrusion direction. At these high magnifications PM2 appears to have a uni-modal grain size distribution in the areas probed. In contrast, previous work on alloys consolidated at 1150ºC showed a bimodal grain size distributions with the smallest grains a few hundred nm in diameter and a significant fraction of larger grains up to 10 μm in diameter.

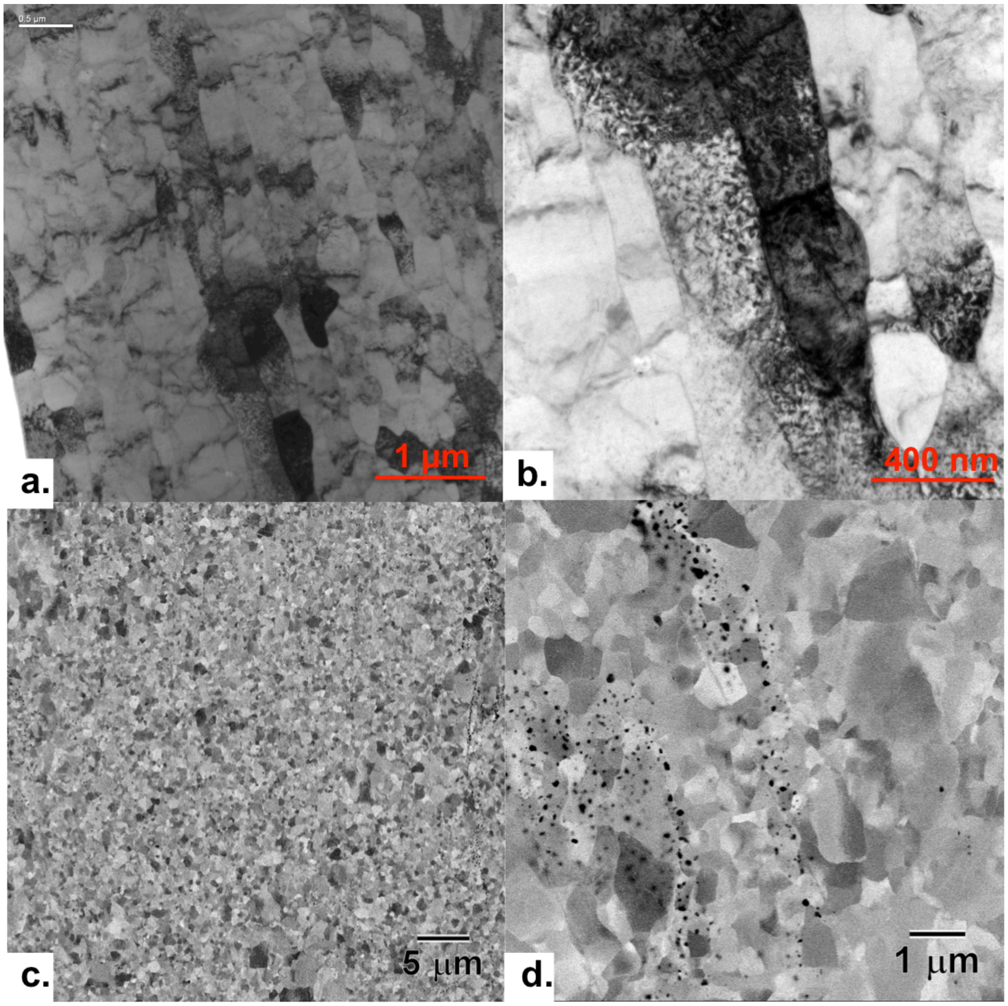

Figure 1. a-b) TEM micrographs perpendicular to extrusion direction showing elongated grain structure; c-d) SEM back-scattered imaging showing fine grain size; the black regions in these micrograph are Ti oxi-nitride phases.

Optical micrographs for chemically etched samples in Figure 2 show the grain structure at lower magnification in three directions. Note that the samples are difficult to etch due to the high Cr content and small grain size. Nevertheless, there appears to be a bimodal grain size distribution perpendicular to the extrusion and rolling direction as shown in Figure 2a. However, the large grain area fraction is small.

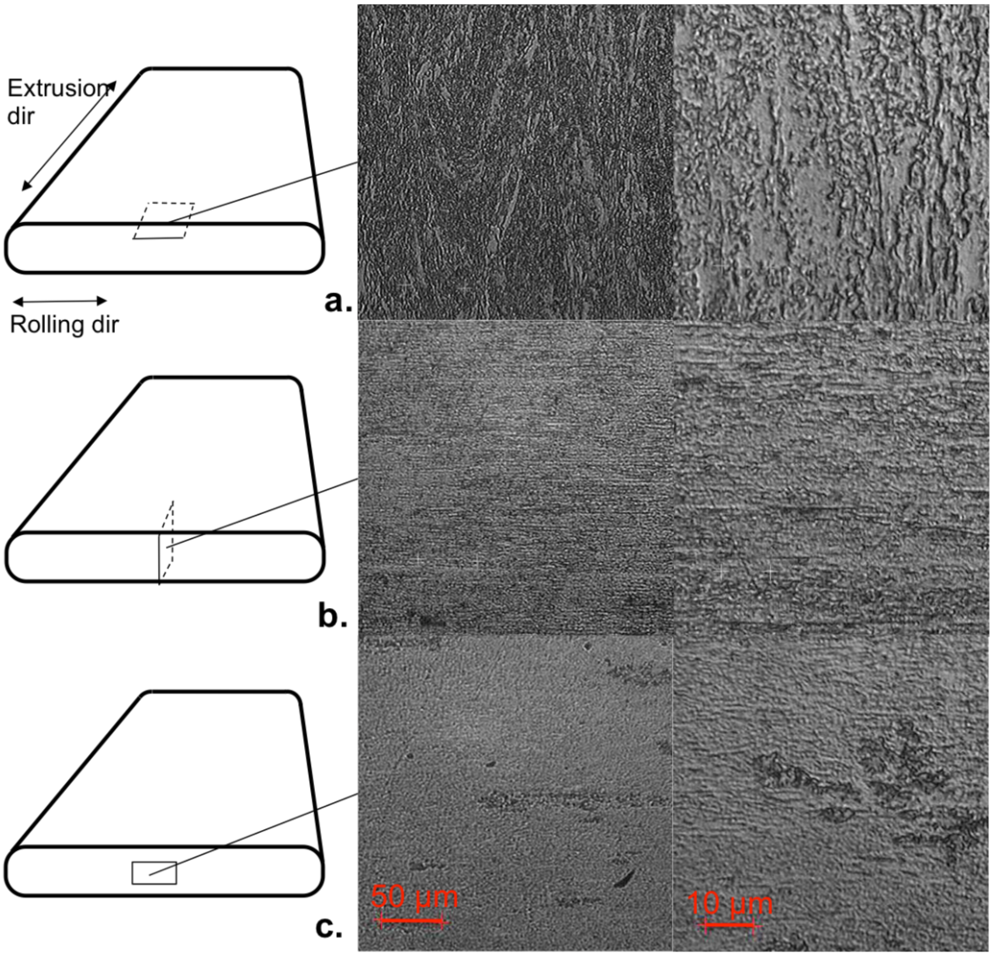

Figure 2. Etched PM2 alloy of surface a) perpendicular to the rolling direction; b) perpendicular to the extrusion direction; c) parallel to the extrusion direction.

TEM also revealed a high density of dislocations. Figure 3 shows two-beam bright field image showing a dislocation density of 1.2×10^{15} m^2.

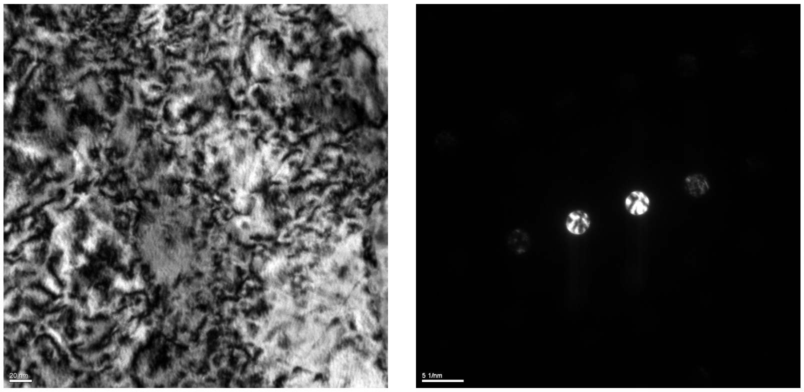

Figure 3. Two-beam bright field TEM image showing high density of dislocations.

The main focus of this research was on characterizing the Y-Ti-O NFs. TEM was first performed on the powder annealed at 1150ºC. Figure 4 shows a high N ≈ $2.1\text{x}10^{23}/\text{m}^3$ of <d> ≈ 2.8 nm NFs, with a volume fraction f ≈ 0.24. EDX showed a Y/Ti ratio of 0.74 for the NF.

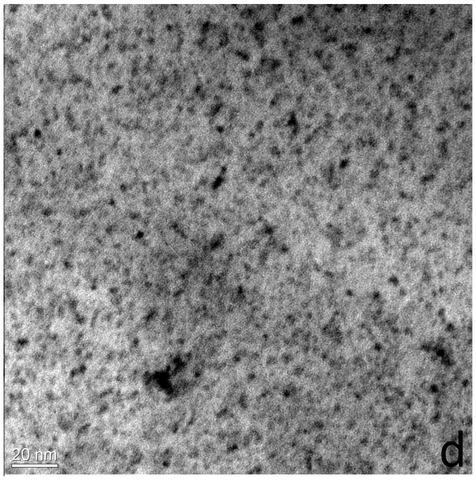

Figure 4. TEM on powder milled with FeO and annealed for 3 h at 1150ºC.

SANS was also performed on four powders milled with FeO for 40 h and annealed for 3 h at 850ºC, 1000ºC, and 1150ºC. Three powders were ramped up to the hold temperature at 15ºC/min and cooled at the same rate to mimic the HIPing time-temperature history. A fourth powder was isothermally annealed at 1150ºC, which is closer to that experienced during extrusion; note the temperature was lower for PM2. Table 2 summarizes the SANS results. The <d> increased and the N and f decreased with increasing annealing temperature. The M/N ratio remained relatively constant. No significant difference was observed between the ramp anneal and isothermal anneal at 1150ºC. SANS has not yet been performed on the consolidated alloy.

Table 2. Summary of the SANS results on milled and annealed powders.

T(°C)-cycle	<d> (nm)	M/N	N ($10^{23}/m^3$)	f (%)
1150 - ramp	2.80	1.2	7.1	0.8
1000 - ramp	2.46	1.1	12.5	1.0
850 - ramp	2.14	1.1	23.4	1.2
1150 - isothermal	2.82	1.2	7.2	0.9

The consolidated PM2 alloy was also analyzed using TEM and APT. TEM measured <d> ≈ 1.4 nm and N ≈ $5.2x10^{23}$, indicating smaller and more numerous NF than in the annealed powders. This gives a volume fraction of 0.07%, which is lower than expected and measured by APT. In foil EDX showed the NF to typically have an estimated Y/Ti ratio less than 1. Figure 5 shows a fairly uniform distribution and high number density of NF. Some larger precipitates were found to contain high levels of Ti and N.

An APT atom map with 2% Y-Ti-O iso-concentration surfaces, shown in Figure 6, has uniformly distributed NFs. Only one APT volume of PM2 was analyzed, with N ≈ $11.0x10^{23}/m^3$ and <d> ≈ 2.1 nm. The size distributions of a previous 1150ºC HIP consolidated alloy, OW2, and PM2 are compared in Figure 7.

The bulk, matrix and NF compositions are shown in Table 3. The high nominal Fe content is believed to be an APT artifact due to trajectory aberrations that artificially place matrix inside the NF. The Y/Ti/O ratio is 12/43/45 giving a Y/Ti ratio of 0.29. The Y/Ti ratio in PM2 is similar to alloy MA957. In addition to Y, Ti, and O, PM2 also appears to contain a high Cr content in the NFs. The 1-D profiles in Figure 8a show a reduction in Fe but a slight increase in Cr through the NFs. The 1-D profiles of Y, Ti, and O in both the z and x-y directions show a Ti and O tail below the Y core with more symmetric concentration profiles in the x-y direction. The extra matrix atoms in the NF are known to be artifacts since the atom density in the precipitates increases to non-physical levels as shown in Figure 8b. This increase in density is caused by dimpling of the atom probe tip surface during evaporation when the NF atoms evaporate at lower electric fields than the matrix or when higher electric fields are induced above the NF [3]. The dimpling alters the electric field lines so that matrix atoms at the NF interface are projected inward and thus observed as part of the NF after data reconstruction.

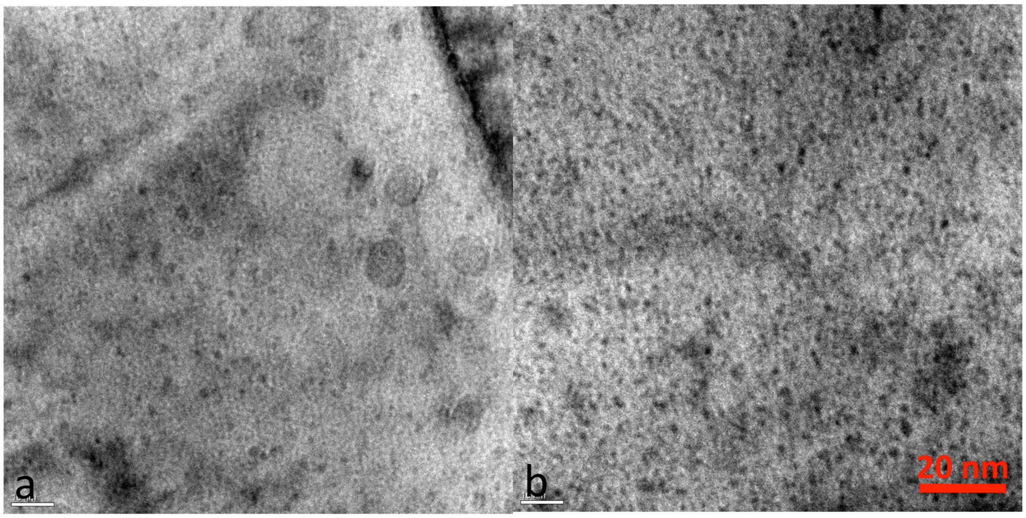

Figure 5. Bright field TEM images of extruded and cross-rolled PM2 alloy.

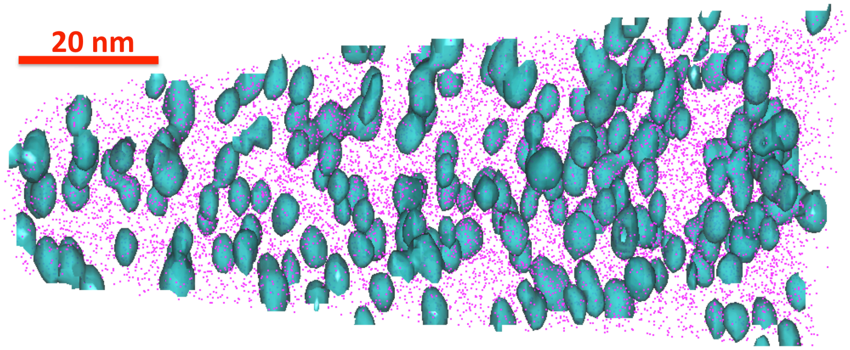

Figure 6. An APT reconstruction of a volume of PM2 analyzed by APT. The NFs are shown by Y-Ti-O iso-concentration surfaces (2.0 at.%).

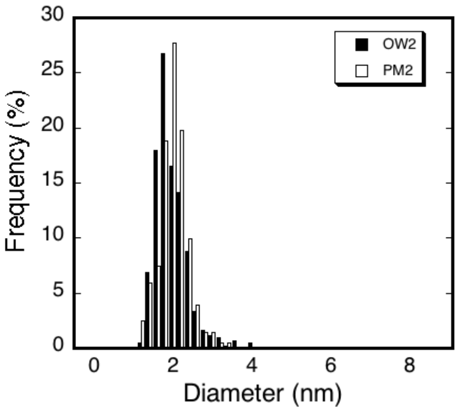

Figure 7. Comparison of the size distribution of NFs in OW2 and PM2.

Table 3. The average APT NF composition (at.%) in PM2.

	Fe	Cr	W	Ti	Y	O	C	Al	Si
Bulk	83.6	14.5	0.952	0.257	0.073	0.342	0.120	0.016	0.075
Matrix	84.2	14.4	0.961	0.059	0.016	0.134	0.108	0.009	0.073
Cluster	72.6	17.3	0.963	3.64	1.05	3.88	0.330	0.132	0.108
Y-Ti-O				42.5	12.3	45.3			

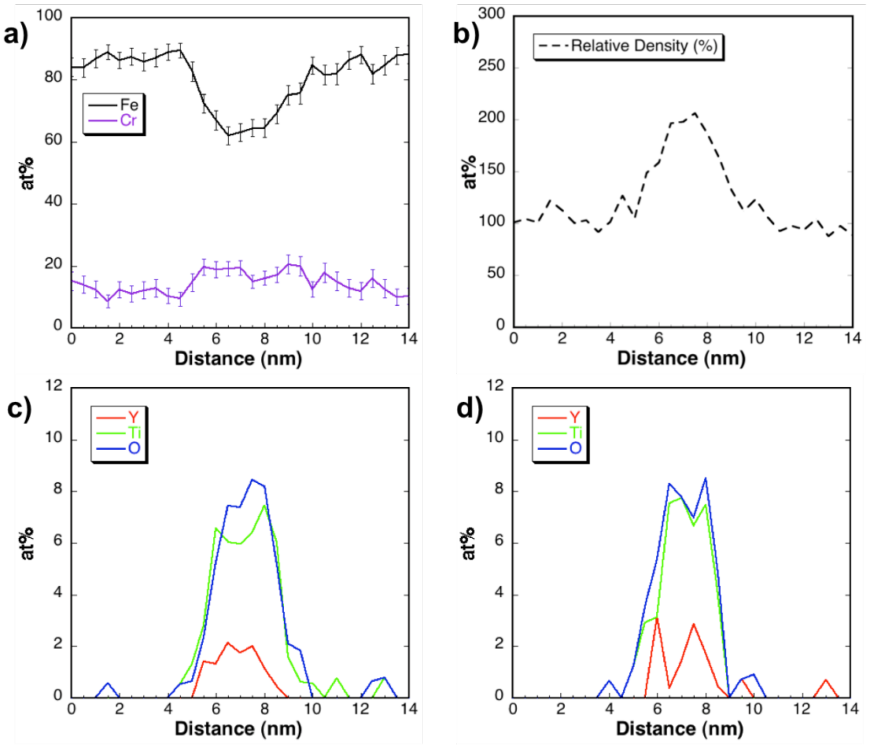

Figure 8. 1-D composition profiles of single NF in PM2 alloy showing a) Fe and Cr content and b) atom density relative to the matrix density in Z direction; c) Z and d) X-Y direction atomic Y, Ti, and O content.

Mechanical Testing

Due to time and material constraints only a limited number of scoping mechanical property tests could be performed. So the results reported here should be generally considered provisional. A hardness of ≈ 401±15 kg/mm^2 was measured on the PM2 surface perpendicular to the extrusion direction. Tensile and creep tests used SSJ2 tensile specimens (4×16×0.5mm) while fracture tests used small bend bars (3.33x3.33x18mm). The tensile and bend bar specimens were oriented as shown in Figure 9. Since there are two deformation orientations we use a modified nomenclature for the bend specimens where the crack propagation path and tensile axis are parallel to the extrusion (LE) or the cross-rolling (LX) directions, while the crack plane normal is transverse to these processing deformation directions.

A yield stress of 1125 MPa and ultimate tensile stress of 1298 MPa was observed in the LX orientation. Thus the ratio of the average of these two stresses with the microhardness value is almost exactly 3. The engineering flow stress has a near plateau between ≈ 1 and 6% strain, indicating limited strain hardening and significant pre-necking uniform elongation. The total elongation was ≈ 11%. An SEM micrograph of the tensile specimen's fracture surface is shown in Figure 10. The material has what appear to be delamination cracks on planes defined by the extrusion and rolling directions. Slightly lower strength was observed in the LE orientation with a yield stress of 1035 MPa and ultimate tensile stress of 1164 MPa, as summarized in Table 4.

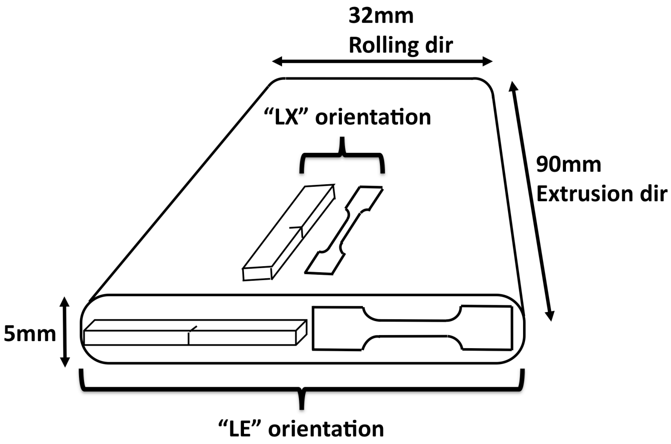

Figure 9. SSJ2 tensile and 1/3 bend bars produced from PM2 extruded and cross-rolled material (not to scale).

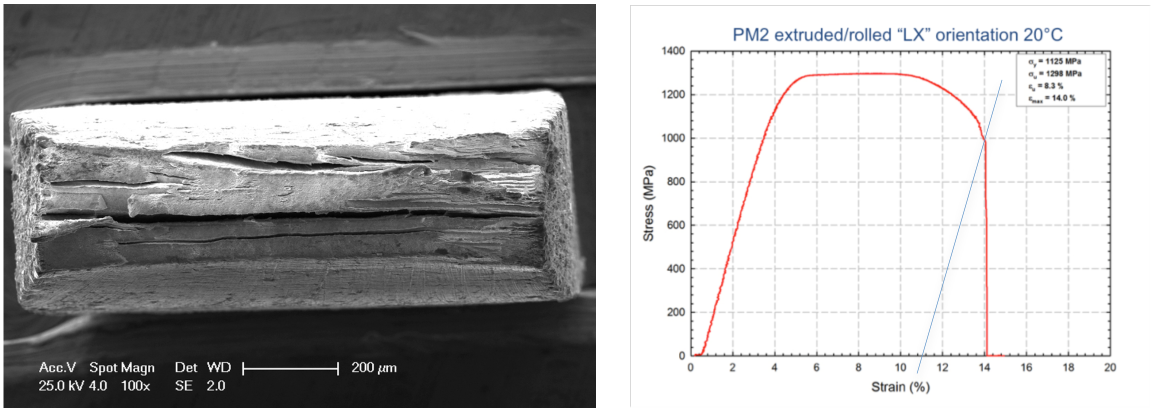

Figure 10. Tensile test fracture surface of PM2 (LX orientation) showing cracks along extrusion and rolling direction.

Table 4. Tensile test results.

T(°C)-cycle	LX	LE
σ_y (MPa)	1125	1035
σ_u (MPa)	1298	1165

Four strain rate jump tests were performed; one in the LE orientation and three in the LX orientation. Stress increases were observed upon application of higher strain rates as expected. However, the stresses did not plateau, but rather slowly decreased with increasing strain. This is believed to be due to development of edge cracks that reduce the load bearing cross section, and possible onset of necking. Thus nominal stresses after the jumps are likely to be less than the actual values, but the results still provide a reasonable basis to estimate the comparative strength of PM2. Future testing will use larger, polished cylindrical specimens, but due to the limited material availability this was not possible for PM2. The strain rates are shown in the Larson-Miller type plot in Figure 12 as filled circles for both orientations. In spite of the fact that these are probably less than the actual stresses, the PM2 strength is higher than either the US and French heats of MA957 and close to that for the Japanese 12YWT that is considered to be one of the strongest NFA variants produced to date.

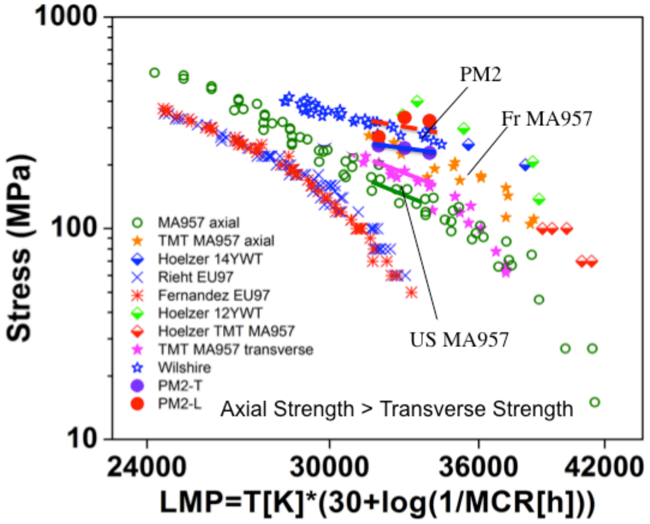

Figure 11. Larson-Miller plot comparing PM2 with other NFA alloys.

Three-point bend bar tests measure fracture toughness of PM2 from -200ºC up to 150ºC for PM2. The results are shown in Figure 12a along with this NFA HIP consolidated at 1150°C and designated OW4. In the latter case the cleavage transition to the upper shelf occurs between 0 and 150°C at ≈ 70 MPa√m (and even lower at 600°C). The high transition temperature is attributed to the large grains and bimodal grain size distribution in this NFA. In contrast the cleavage transition for both orientations of PM2 is much lower, between -200 and -100°C. However, the upper shelf ductile tearing toughness is still low in PM2 at ≈ 80 MPa√m. The temperature at the mid-point between lower and upper shelf, assumed to be at ≈ 20 and 80 MPa√m, respectively, is ≈ -160°C. The much lower transition temperature in PM2 is attributed to its more uniformly fine grain structure. The low ductile tearing toughness is thought to be due to a high density of coarser scale Ti-oxides or oxi-nitrides that act as microvoid nucleation sites as illustrated to the micrograph in Figure 12b. Figure 12c shows the same type of delamination cracks that are also observed in the tensile test.

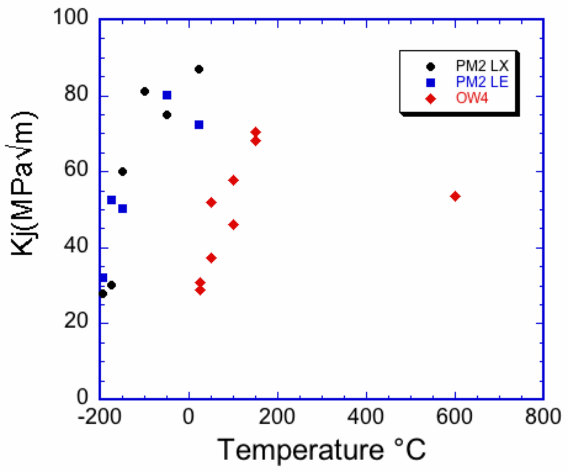

a.

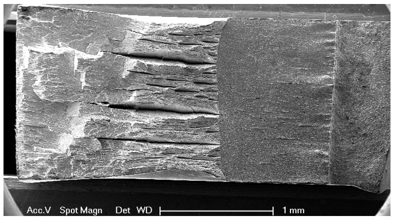

b.

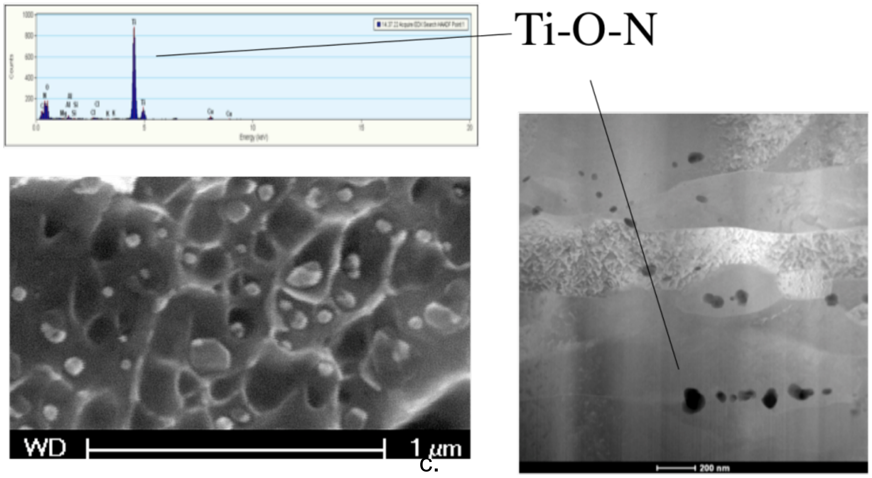

c.

Figure 12. DBTT of OW4 and PM2 in LE and LX orientations; and b) high magnification fracture surface and TEM image showing large Ti-oxi-nitrides; c) low magnification fracture surface of PM2 LX bend bar showing delamination.

FUTURE WORK

SANS will be carried out to complete the characterization of the NF in PM2.

REFERENCES

1. N. J. Cunningham, "Study of the Structure, Composition, and Stability of Y-Ti-O nm-Scale Features in Nano-Structured Ferritic Alloys," Ph.D. Thesis, University of California - Santa Barbara, Santa Barbara, CA (2012).
2. Y. Wu, N. J. Cunningham, A. Etienne, E. Haney, G. R. Odette, "The Effect of Bulk Oxygen Concentration on the Micro-Nanostructure and Strength of a 14Cr Nanostructured Ferritic Alloy," DOE Fusion Reactor Materials Program Semiannual Progress Report for the Period Ending June 30, 2011, DOE/ER-0313/50 2011.
3. C. Oberdorfer and G. Schmitz, "On the Field Evaporation Behavior of Dielectric Materials in Three-Dimensional Atom Probe: A Numeric Simulation," *Microsc. Microanal.* **17**, 2011, 15-25.

3.1 Determination of Interfacial Mechanical Properties of Ceramic Composites by the Compression of Micro-Pillar Test Specimens — C. Shih, Y. Katoh, K. J. Leonard, H. Bei, E. Lara-Curzio

OBJECTIVE

The objective of this work is to determine the interfacial mechanical properties of fiber matrix composites through a novel method, which involves micro compression test of micro, sized pillars containing an inclined fiber/matrix interface. These interfacial mechanical properties are important factors that affect the fracture behavior of composites. Determination of these properties is critical for modeling of composite behaviors and for designing composite with high strength and toughness.

SUMMARY

The interfacial debond shear strength and the coefficient of internal friction between the fiber and pyrocarbon interface of a SiC fiber reinforced CVI SiC matrix composite are determined using a novel method, which involves micro compression of micro sized pillars containing an inclined fiber/matrix interface. The interfacial debonds shear strength and the coefficient of internal friction was determined to be 100 MPa and 0.73, respectively. This new test method with simple geometry showed high data reproducibility; moreover, the results fit the proposed Coulomb fracture criterion well. The determined interfacial properties are compared with those determined from fiber push out tests.

PROGRESS AND STATUS

Introduction

Ceramic materials are strong, chemically inert and high temperature compatible. These unique properties make them promising for applications with extreme environments. However, the brittle nature of ceramic materials greatly limits its application. Ceramic matrix composites (CMCs) can increase the toughness and reliability of ceramic materials and have gained interest for various applications where high temperature environments are encountered, including aerospace, gas turbine, and nuclear energy [1]. The high toughness of CMCs is achieved through proper fiber/matrix (F/M) interface properties that result in arresting/deflecting of cracks formed in the matrix and sliding of the fiber during loading [2]. Therefore, designing of the F/M interface in CMCs is a critical issue for achieving good mechanical properties such as high service strength, high damage tolerance and long service life [3].

The interfacial debonds shear strength and the sliding stress of fiber pull out is the two most important parameters used for modeling of CMC properties [2, 4]. These interfacial properties can be determined by several methods including the single fiber push-out [5] or push-in tests and the tensile unloading/reloading hysteresis analysis [6]. However the uncertainty in in-situ clamping stress and complex stress state associated with Poisson effect make determination of these properties difficult.

The nano indentation technique has been widely adopted in the characterization of mechanical behavior of materials at small scales [7, 8]. Recently, this technique has extensively been used for micro- or nano-pillar compression test to study mechanical properties and deformation mechanisms of materials including metals [9-11] and monolithic ceramics [12]. In this study, a novel test method is proposed and evaluated; where micron-sized, pillar shaped samples containing an inclined fiber/matrix interface were prepared from a SiC fiber reinforced SiC matrix composites using a focused ion beam micro-machining. The micro-pillars were then tested in a nano-indentation system equipped with a flat punch tip. This new test method employs a simple geometry and mitigates the errors associated with complex stress state.

Samples with different interface orientations were prepared and tested. The interfacial debonds shear strength and the internal friction coefficient for the interface is determined and these values are compared with those obtained by other test methods.

Experimental

Materials and micro-pillar preparation

The uni-directional single fiber-tow composite (mini-composite) used in this investigation consisted of Hi-Nicalon™ Type S SiC fibers (Nippon Carbon, Co., Ltd., Tokyo, Japan) and a b-SiC matrix. The SiC fiber has a diameter of ~11 ± 2 mm. The actual fiber diameter varies along its length. The fibers were coated with fiver layers of (50 nm pyro-carbon/1mm SiC). Both the matrix and fiber coating were synthesized by chemical vapor infiltration (CVI) by Hyper-Therm HTC, Inc (Huntington Beach, CA). The mini-composites were cut with a diamond saw and embedded in epoxy at three different angles (45, 55 and 60°) and subsequently polished using standard metallographic techniques with a series of diamond pastes to a surface finish of 100 nm. Micro-pillar test specimens were machined from the polished samples using focused iron beam (FIB) milling with a FEI (Hillsboro, OR) Qunta™ 3D 200i DualBeam™ instrument, similar to ref [13]. Initially, a large diameter annulus (~40 mm in diameter and 2 mm deep) was milled to make it easy to locate the small micro-pillars during following compression test in a nano-indentation system and to ensure that the pillars were being compressed without interference from the edge of the annulus. A beam current of 15 nA was used in the rough milling. The outer surfaces of the 3.7 mm diameter pillars containing pyrocarbon/SiC interface left standing in the middle of the annuli were then milled using a lower bean current (1 nA or less) to produce ~3.5 mm diameter cylindrical pillars. The pillar geometry is schematically shown in Fig. 1. The finished micro pillars are about 3.5 mm in diameter and at least 15mm in length. The diameter of the pillars was measured using electron beam images from the FIB system with a viewing angle along the pillar longitudinal direction. The pillars sit inside a pit that is about 40mm in diameter to accommodate the nano-indenter tip. Fig. 2 shows an electronic beam micrograph of a finished 55° interface micro-pillar before testing. The pyro-carbon interphases are readily visible and are indicated by white arrows. It can be seen that the pillar is slightly tapered because the divergence of ion beam, which was minimized as much as possible. For simplicity, this effect is not accounted for in the stress analysis.

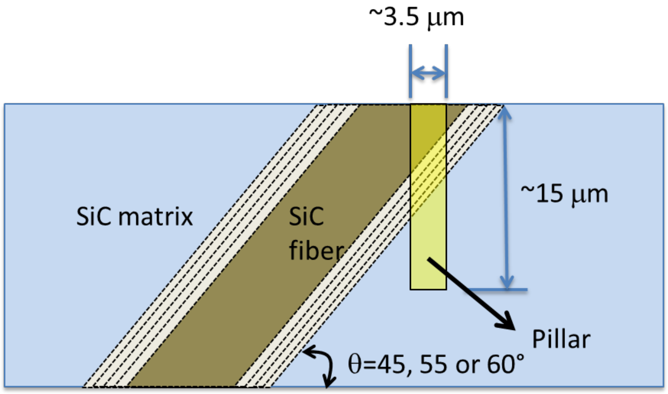

Fig. 1. A schematic plot showing the pillar geometry.

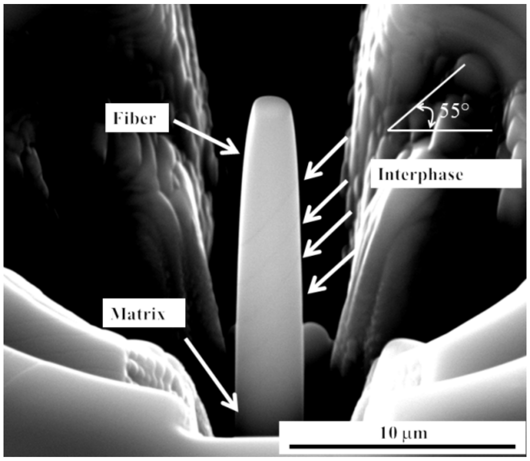

Fig. 2. Electron beam micrograph of a 55° interface micro pillar from a side angel view in the FIB.

Micro compression testing

Micro compression tests were performed with a MTS Nano XP indenter system (MTS Nano Instrument, Oak Ridge, TN) with a flat indenter tip. The flat indenter with diameter about 15 mm was custom fabricated form a conical diamond tip by using the FIB milling. The compression of the micro pillar was done under a constant load rate of 0.1 mN/sec with a data acquisition rate of 10 Hz. Details of micro-pillar testing is described in [13]. A sudden increase in displacement (strain burst) indicates that debonding and sliding along one of the interfaces has occurred. The pillars after micro compression test were examined with a field emission gun scanning electron microscope (S4800, Hitachi, Japan).

Pillar interface force balance at break

It is assumed that the pillar has a constant cross-section area, A, (ignoring the tapering effect resulting from the FIB micromachining process) and that the interface is a flat plane with an area equal to A/cosq, with q being the interface angel as shown in Fig. 1. It should be noted that the interface has a curvature as a result of the cylindrical geometry of the fiber coatings. The load, P, from the indenter is resolved into a normal stress and a shear stress with respect to the interface as shown in Fig. 3. The Coulomb fracture criterion, which is generally used for rock failure in geology, is used as the failure criterion for this study [14]. At the pillar break load, P_{break}, the shear stress component from P should be equal to the interface debond shear stress (t_{debond}), which is related to the chemical bond strength of the interface, plus the internal friction contribution, which is estimated to be equal to the resolved normal stress times the internal friction coefficient, m. This relationship is shown in Equation 1.

$$P_{break} \cdot \frac{\sin\theta \cdot \cos\theta}{A} = \tau_{debond} + P_{break} \cdot \frac{\cos\theta \cdot \cos\theta}{A} \cdot \mu \qquad \text{(Equation 1)}$$

The Coulomb fracture criterion model predicts that in a plot of the resolved shear stress (P_{break}×sinq×cosq/A) versus resolved normal stress (P_{break}×cosq×cosq/A) at different interface angel, q, the data points should lie in a straight line with slope equal to the internal friction coefficient (m) and intersect equal to t_{debond}.

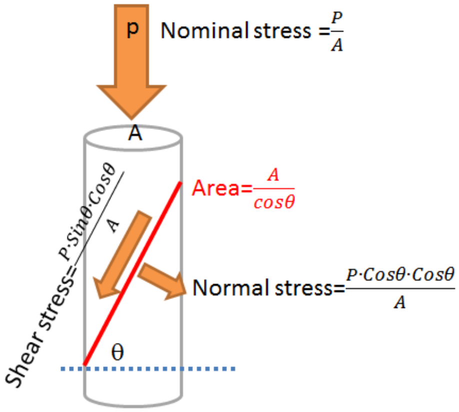

Fig. 3. Schematic showing the resovled stresses.

RESULTS AND DISCUSSIONS

Load displacement curves test

Representative load displacement curves of the micro compression tests are shown in Fig. 4. All the curves showed elastic behavior up to a breaking load, which was followed by a sudden burst of indenter displacement. The elastic behavior has been reported for CVD β-SiC micro-pillar compression tests [12]. Since all the pillars are of the same shape and materials, and since the pyrocarbon interphase layers are very thin (50 nm × five layers), the pyro carbon interphase layers with different angels are not expected to affect significantly the modulus of the pillars. Indeed, the initial slope of the load-displacement curves is the same for all the undamaged pillars (~0.077 mN/nm). The real modulus of the pillars cannot be obtained directly from the load displacement curves because the penetration of the pillar into the substrate and the load frame compliance of the machine need to be accounted for. Load displacement of a damaged pillar (sample 45°-2) is also shown in Figure 3. This pillar showed a smaller initial slope and breaking load, indicating a damaged interface. The damage is believed to be from either the CVI process or from the high-energy ion beam during the FIB process. It is worth noting that the significant slope reduction is helpful to identify damaged pillar samples.

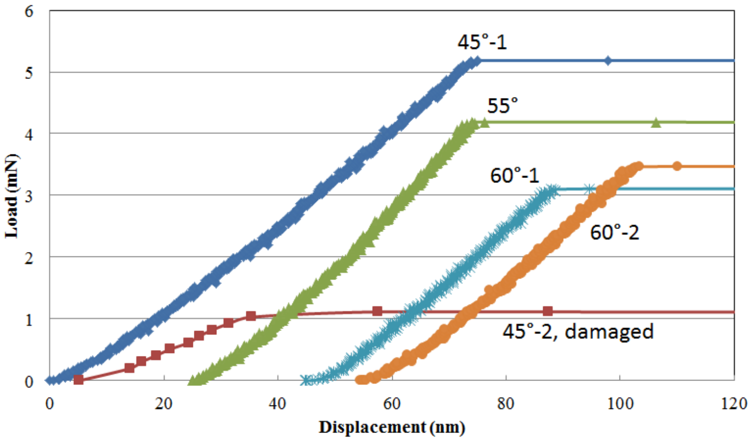

Fig. 4. Representive load displacement curves of the micro compression tests.

SEM observation following compression tests

Fig. 5 shows SEM images of two 55° micro-pillars after the compression test. The appearance of the interface angles seem different because of different specimen tilt angles in the SEM. Failure of the pillars always occurred along the innermost fiber/pyrocarbon coating interface, leaving a smooth fracture plane. It is possible that the slight taper of the micro-pillars is contributing to this trend. Energy-dispersive X-ray spectroscopy (EDS) analysis revealed the presence of a carbon rich layer on the remaining pillar fracture surface, indicating that fracture occurred between the SiC fiber and the pyrocarbon layer. This type of adhesive failure was also reported for Hi-Nicalon Type S SiC fibers reinforced CVI SiC/SiC composites under both interlaminar shear test and trans-thickness tensile test [15].

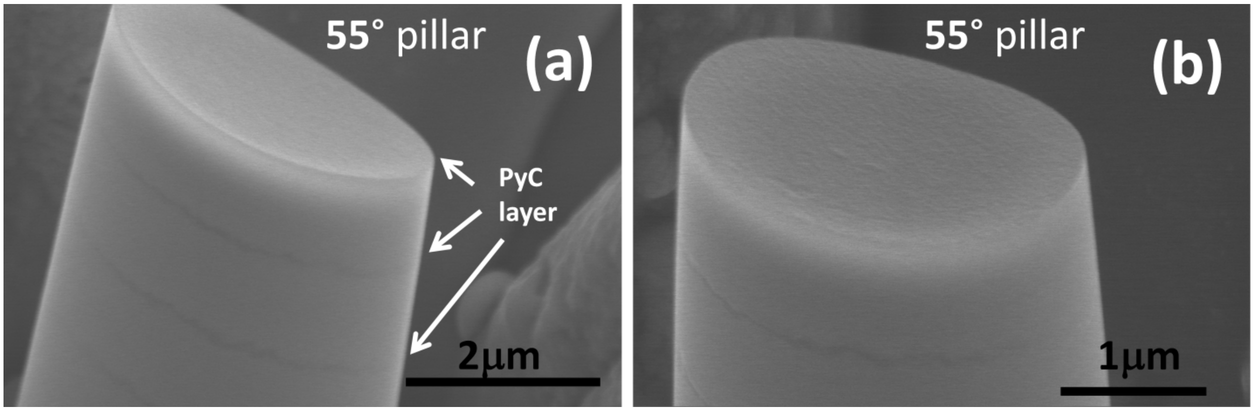

Fig. 5. SEM images of the micropillar after micro compression test.

Since a crack initiated and grew only along one interface, this test method is useful to determine the properties of that interface. It should be noted that for some fiber composites with multilayer interphase, crack propagation occurs within the PyC interphase adjacent to the fiber during fiber push in test [16], presenting a cohesive type of failure. Therefore, interfacial properties obtained from the fiber push in test and the micro pillar test correspond to different crack propagation mechanisms and should not be compared directly.

Normal and shear stress at the interface

The resolved shear stress versus the resolved normal stress plot is presented in Fig. 6 for pillars with three different interface angels. Both individual data point (triangle) and averaged values for the same inclination angle (diamond) are shown, illustrating the good degree of reproducibility. A liner fit was found to describe the data well, with a high coefficient of correlation, 0.994, which validates the applicability of the Coulomb fracture criterion described previously. The obtained interface debonds shear stress (t_{debond}) and coefficient of internal friction (m) between the pyrocarbon and SiC interface were found to be 100 MPa and 0.73, respectively, as shown in Fig. 5.

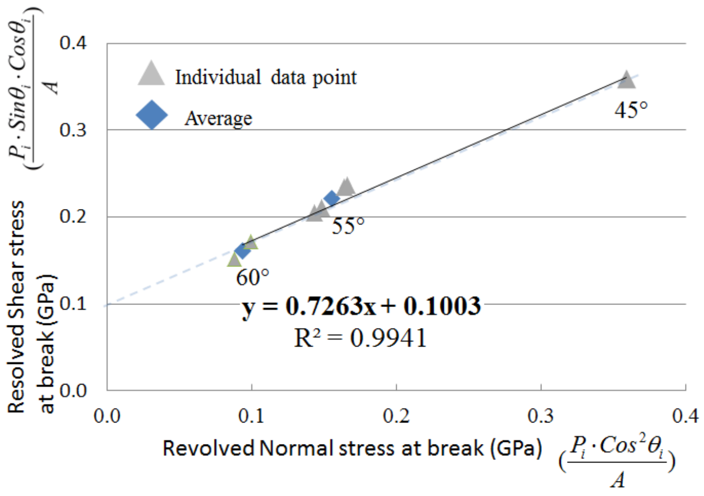

Fig. 6. Resolved shear stress versus resolved normal stress plot.

The interface debond shear stress (t_{debond}) of similar CVI SiC/SiC composite has been investigated using the fiber push in test [5] with different models [4, 17], and the reported t_{debond} is in the range of 160 to 190 MPa with large variability of 39% for the interface between Nicalon™ SiC fiber and CVI pyrocarbon. More recently, Nozawa et al. [16] reported that the interface debond shear stress of Hi-Nicalon™ Type-S SiC fiber/ CVI SiC matrix composites with a 720 nm single layer pyrocarbon interphase was found to be 280 MPa. The higher value reported for t_{debond} by the fiber push in test is partially because the push in test model doesn't account for the effect of clamping stress when debonding is initiated [4, 17, 18]. The Poisson effect during fiber push in test could also cause complex stress state and errors. The authors believe that the t_{debond} determined with the micro pillar compression method provides a value that is more representative of the chemical bonding/cohesion strength of the interface.

Pyrocarbon is generally considered to be a material of low friction coefficient. The friction coefficient between different types of SiC fibers and different thickness of pyrocarbon interphase in SiC/SiC composites has been estimated by fitting the loading curves from fiber push out test using the Hsueh model [18]. The reported friction coefficient is in the order of 0.01 to 0.05 [5, 19], which is more than an order of magnitude smaller than the internal friction coefficient of 0.73 reported here. The authors believe that the internal friction coefficient in this study, which has been discussed extensively in geophysical research community [14], has a different physical meaning from the sliding coefficient of friction, which is well known to the materials research community. The two coefficients should not be compared directly because of their different meanings.

CONCLUSIONS

A novel test method is proposed and evaluated; where micron-sized, pillar shaped samples, containing an inclined fiber/matrix interface, were prepared and tested using the micro compression technique. The results prove that the new test method is useful for determination of interfacial debond shear strength and internal interfacial friction coefficient. The load displacement curves showed elastic behavior with similar slopes regardless if angle of inclination, and a well-defined breaking load. Out of the eight pillars prepared, only one showed pre-test damage, which was characterized by a low slope and low breaking load. Overall, this new test method shows high successful test rate and low data variability.

SEM observations showed that debonding occurred at the top fiber/pyrocarbon interface. The data points from three different interface angles fit suggest that the Coulomb fracture criterion can describe well the experimental results. The determined t_{debond} and internal friction coefficient for the SiC fiber/pyrocarbon interface are 100.3 MPa and 0.73 respectively. The determined t_{debond} appears smaller than t_{debond} from fiber push in test because the latter test uses a model that doesn’t account for the effect of residual clamping stress during initial debonding. The determined internal friction coefficient of the micro pillar test was found to be an order of magnitude greater than the static friction coefficient determined by fiber push in testing and it has become clear that these two parameters have different physical meanings [14]. The new test method is simple, reproducible and complementary to other test methods. It determines interfacial properties that are important for understanding and predicting the mechanical behavior of fiber composites.

REFERENCE

[1] R. Naslain, *Compos. Sci. Technol.* **64** (2004) 155-170.
[2] A. G. Evans and D. B. Marshall, *Acta Metall.* **37** (1989) 2567-2583.
[3] R. R. Naslain, R. J. F. Pailler and J. L. Lamon, *Int. J. Appl. Ceram. Technol.* **7** (2010) 263-275.
[4] C. H. Hsueh, *Mat. Sci. Eng. A-Struct.* **123** (1990) 1-11.
[5] F. Rebillat, J. Lamon, R. Naslain, E. Lara-Curzio, M. K. Ferber and T. M. Besmann, J*. Am. Ceram. Soc.* **81** (1998) 965-978.
[6] J. M. Domergue, E. Vagaggini and A. G. Evans, *J. Am. Ceram. Soc.* **78** (1995) 2721-2731.
[7] W. C. Oliver and G. M. Pharr, *J. Mater. Res.* **19** (2004) 3-20.
[8] W. C. Oliver and G. M. Pharr, *J. Mater. Res.* **7** (1992) 1564-1583.
[9] M. D. Uchic and D. A. Dimiduk, *Mat. Sci. Eng. A-Struct.* **400** (2005) 268-278.
[10] M. D. Uchic, D. M. Dimiduk, J. N. Florando and W. D. Nix, *Sci.* **305** (2004) 986-989.
[11] C. J. Lee, J. C. Huang and T. G. Nieh, *Appl. Phys. Lett.* **91** (2007).
[12] C. Shin, H. H. Jin, W. J. Kim and J. Y. Park, *J. Am. Ceram. Soc.* **95** (2012) 2944-2950.
[13] S. Shim, H. Bei, M. K. Miller, G. M. Pharr and E. P. George, *Acta Mater.* **57** (2009) 503-510.
[14] J. Handin, *J. Geophys. Res.* **74** (1969) 5343.
[15] C. Shih, Y. Katoh, K. Ozawa, E. Lara-Curzio and L. L. Snead, *J. Am. Ceram. Soc.* **Submitted** (2012).
[16] T. Nozawa, Y. Katoh and L. L. Snead, *J. Nucl. Mater.* **367** (2007) 685-691.
[17] C. H. Hsueh, *Mat. Sci. Eng. A-Struct.* **145** (1991) 135-142.
[18] C. H. Hsueh, *J. Am. Ceram. Soc.* **76** (1993) 3041-3050.
[19] E. Lara-Curzio, M. K. Ferber and R. A. Lowden, *Ceram. Eng. Sci. Proc.* **15** (1994) 989-1000.

3.2 Process Development and Optimization for Silicon Carbide Joining and Irradiation Studies — T. Cheng, J. O. Kiggans, Jr., Y. Katoh, and L. L. Snead (Oak Ridge National Laboratory)

OBJECTIVE

The objective of this task is to develop and optimize joining processes for silicon carbide (SiC) for future neutron irradiation effects study in the High Flux Isotope Reactor (HFIR).

SUMMARY

The candidate joint materials for the ongoing work to evaluate the neutron irradiation effects on chemically vapor-deposited (CVD) SiC includes bonds produced by the NITE (nano-infiltration and transient eutectic-phase) – like transient eutectic phase processes, diffusion bonding utilizing active titanium or molybdenum inserts, calcia-alumina (CA) glass/ceramics, and Ti-Si-C MAX phase through displacement reaction. During the present reporting period, joint specimens were successfully produced through the active metal insert methods and the NITE-like process, and then evaluated for as-fabricated properties.

PROGRESS AND STATUS

Development of Joining Process

In the preparation of joining specimens, flat plates of chemical vapor deposition (CVD)-SiC (“CVD SILICON CARBIDE,” Dow Chemical, Marlborough, MA) were joined by hot pressing with inserts of titanium (Ti) foil (0.025 mm thick, 99.94%, 75 × 75 mm, Alfa Aesar), molybdenum (Mo) foil (0.025 mm thick, 99.95%, 150 × 150 mm, Alfa Aesar), Mo powder slurry (powder size of ~44 µm), or nano-infiltrated transient eutectic SiC slurry (NITE [1], 6wt% Y_2O_3-Al_2O_3-SiO_2 sintering additives). The CVD-SiC samples were ultrasonically cleaned in acetone, and then dried in an oven. For the specimens joined by NITE, a thin layer of NITE slurry was applied on the face of two SiC specimens, which were then placed face to face to form a sandwich. Joining was performed in a hot-press furnace in a flowing Ar atmosphere with a uniaxial pressure of 15-20 MPa. High vacuum (10^{-5} torr) was applied and held for 12 h in the furnace before heating in order to remove gas impurities. Joining conditions for each of the joining materials were carefully designed; the processing conditions and the results of the testing are summarized in Table 1.

Table 1. Processing conditions, shear strength, joint microstructures, and fracture behavior of CVD-SiC joined by different filler materials

Insert materials	Specimen ID	Processing Conditions			Joint Strength		Observed Phases	Joint Microstructure	Failure location
		Temperature (°C)	Pressure (MPa)	Time (h)	Mean Shear Strength (MPa)	Standard Deviation (MPa)			
Mo foil	Mof-1500-1-15	1500	15	1	55.2	15.4	Mo_2C, Mo_5Si_3	No debonding	Through joint
Mo foil	Mof-1700-1-20	1700	20	1	85.2	58	Mo_2C, Mo_5Si_3	No debonding	SiC base
Mo foil	Mof-1300-5-20	1300	20	5	15.2	7.2	Mo_2C, Mo_5Si_3	No debonding	Interface and base
Mo foil	Mof-1500-5-20	1500	20	5	18.8	11.2	Mo_2C, Mo_5Si_3	Partially debonding	Primarily at base
Mo powder	Mop-1500-5-20	1500	20	5	9.3	3.6	Mo_2C, Mo_5Si_3	Porous/dense joint No debonding	Through porous joint
Mo powder	Mop-1300-5-20	1300	20	5	6.5	5.7	Mo_2C, Mo_5Si_3	Porous/dense joint, debonding at porous joint	Interface and base
Ti foil	Tif-1500-1-15	1500	15	1	97.6	8.8	85% TiC, Ti_3SiC_2	No debonding	Through joint
Ti foil	Tif-1300-1-20	1300	20	1	1.7		Ti_5Si_3, TiC	Ti_5Si_3/SiC debonding	Interface
Ti foil	Tif-1500-5-20	1500	20	5	28.4	13.7	Ti_3SiC_2	No debonding	Joint and interface
NITE slurry	NITEs-1860-1-20	1860	20	1	43.9	38.8	SiC	Porous/dense joint, debonding at porous joint	Interface

Note: Four replicates were used in tests in order to achieve statistical accuracy.

Mechanical testing and characterization

Planned irradiation testing will examine the strength of the SiC joints using torsional shea employing solid hourglass type specimens. The torsional shear test is nearly ideal f purpose because of its simplicity and ability to apply true shear loading to the joint speci However, machining the torsional hourglass specimens is relatively expensive and consuming. Other test methods are more appropriate for the purpose of estimati approximate strength in a timely manner to support joining process optimization studies.

In this work, the joint strength was estimated by loading a double-notched test speci uniform width in compression, which is the standard test method ASTM C1292 for inter-l shear strength of continuous fiber-reinforced advanced ceramics at ambient temperatures test method, often referred to as double-notch shear (DNS) test, is in principle a variation offset single lap shear test as defined in ASTM D905 with an improved alignment capabili to the presence of the extended end sections. The hot-pressed plates were machined int specimens according to the dimension scheme shown in Fig. 1. The actual dimensions a were L = 20.0 mm, W = 6.0 mm, t = 7.6 mm, h = 1.3 mm, and d = 3.0 mm. Figures 2 (a) a show a schematic and a photograph of the test setup and a specimen. Failure of th specimen occurs by shear between two centrally located notches machined halfway throu thickness and spaced a fixed distance apart on opposing faces (ASTM 1292).

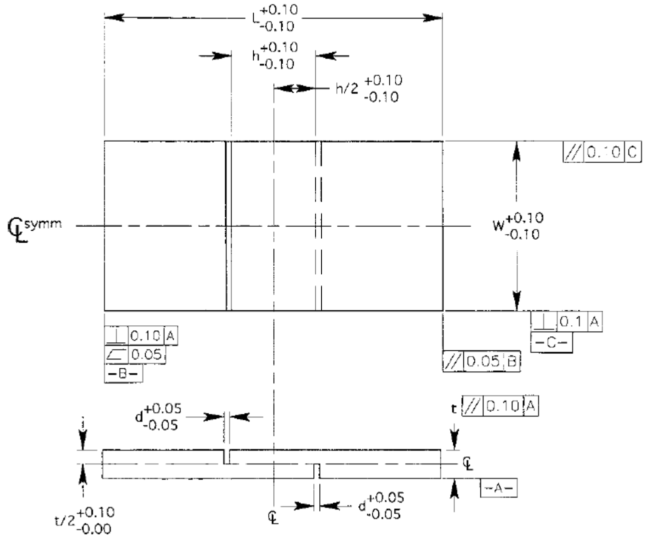

Fig. 1. Schematic of the double-notched compression test specimen. Note: All dimensio in millimeters.

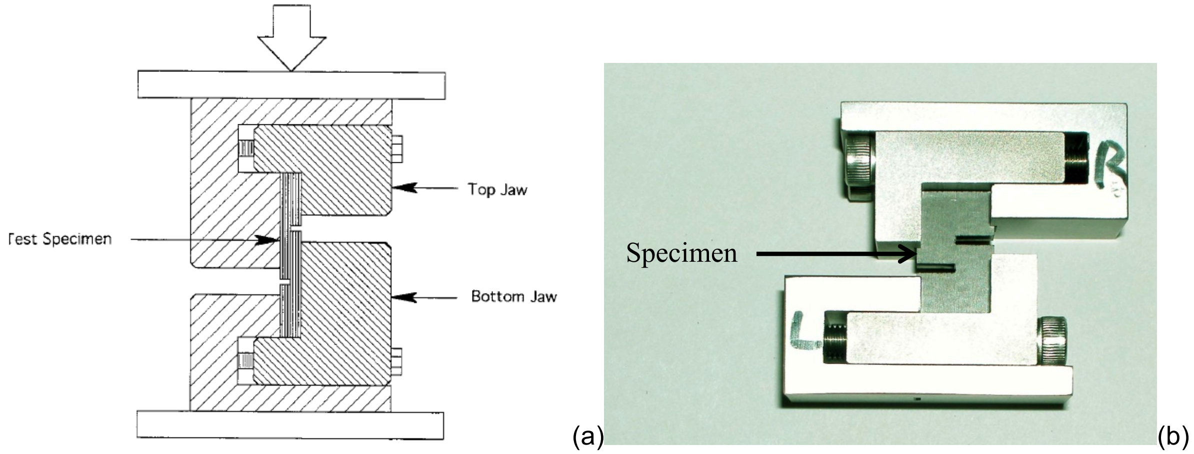

Fig. 2. Schematic (a) and an image (b) of test fixture for the double-notched compression test specimen.

Polished cross-sections of the tested specimens were characterized using field-emission-gun scanning electron microscopy (FEG-SEM) in a Hitachi Model S4800, equipped with energy dispersive spectroscopy (EDS). The surface phases formed and their relative amounts were determined by X-ray diffraction (XRD) analysis (Model Scinatag Pad V, Thermo ARL). (NOTE: all SEM images shown below were taken on specimens after shear testing.)

Results of As-fabricated Characterization

The processing parameters including hot pressing temperature, pressure, time, and joining material thickness were selected based on thorough literature review, summarized in Table 2. Multiple joining conditions were attempted for each joining material in order to determine their optimal processing conditions, which will be used for fabricating the joint specimens for irradiation behavior study. Table 1 lists processing conditions, shear strengths, joint microstructures, and fracture behaviors of CVD-SiC joined by Ti foil, Mo foil, Mo powder slurry, or NITE slurry.

Ti foil joint

For Ti diffusion bonding, a scheme representing the Ti joint microstructure evolution at different hot-pressing temperatures was developed by Gottselig [5], shown in Fig. 3. Low temperature (<1250°C) may result into complex interlayer structures, which may not be favorable in robust process design and mechanical property control. Therefore, temperatures in a range of 1300-1500°C were selected for Ti joining in this work.

Pressure higher than 10 MPa has no effect on bonding quality [2, 5], therefore, slight variations in pressure, e.g., 15 MPa and 20 MPa should not result in obvious joint microstructure evolution. Temperature and time effects are examined in this work. Figure 4 shows the microstructure of the Ti joint formed after hot pressing at 1500°C for 1 h. The Ti foil was completely reacted with SiC by forming TiC (primary product) and Ti_3SiC_2 (Table 1), evidenced by the measured XRD spectrum (not shown here) in which no Ti metal phase was detected. In Fig. 4, the Ti joint seems homogenous and no phase contrast was observed, suggesting that the fine Ti_3SiC_2

grains may disperse in the TiC matrix. Cracks were found in the joint indicating its brittle character. The formed TiC phase has good wetting behavior on SiC, evidenced from good contact at the joint/substrate interface. The effect of pressing time was analyzed by extending the hot pressing time to 5 h, keeping the temperature and pressure constant, and the microstructure of the resulting Ti joint is illustrated in Fig. 5. A uniform Ti_3SiC_2 interlayer was formed under the above conditions, indicating that Si diffusion dominated in the 5 h test by reacting with TiC, forming Ti_3SiC_2. No interfacial debonding was observed. Hot pressing at a lower temperature of 1300°C was also performed to examine the temperature effect. The microstructure of Ti joint formed at 1300°C for 1 h is shown in Fig. 6. The TiC phases (dark) with small and large grains are dispersed in Ti_5Si_3 (bright) matrix, which is adjacent to SiC base. Interfacial debonding is clearly observed in Fig. 6, possibly due to the large coefficient of thermal expansion (CTE) mismatch between SiC and Ti_5Si_3. These results suggest that the Ti foil joining requires high temperature, e.g. 1500°C, in order to achieve good interfacial bonding with the SiC base.

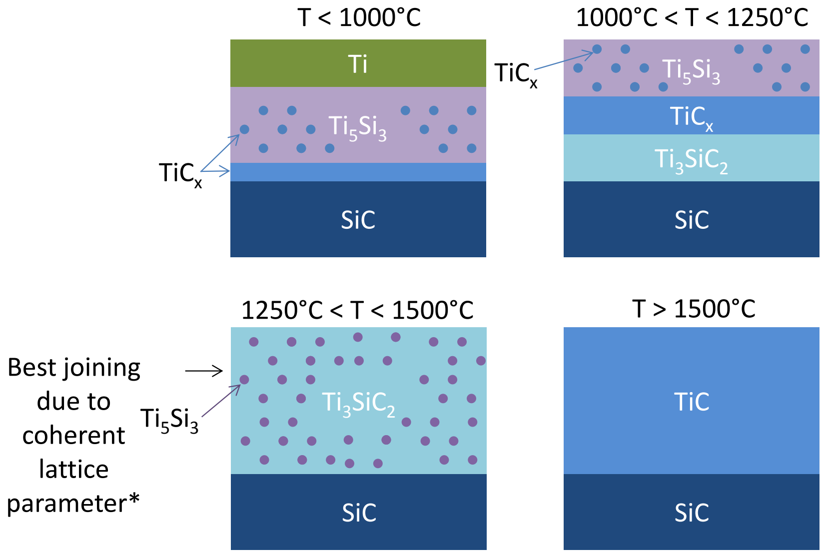

Fig. 3. A schematic illustration of Ti joint microstructure evolution at various temperatures.

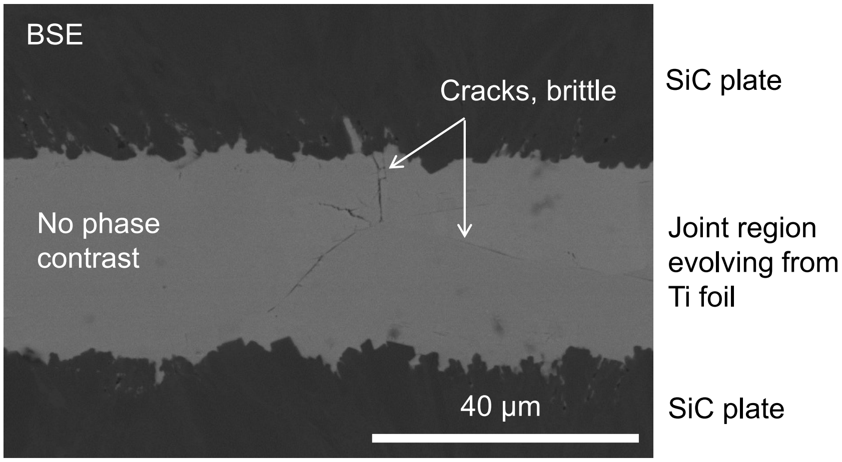

Fig. 4. Back Scattering Electron (BSE) cross section image of joint formed between two SiC plates and Ti foil hot pressed at 1500°C for 1 h.

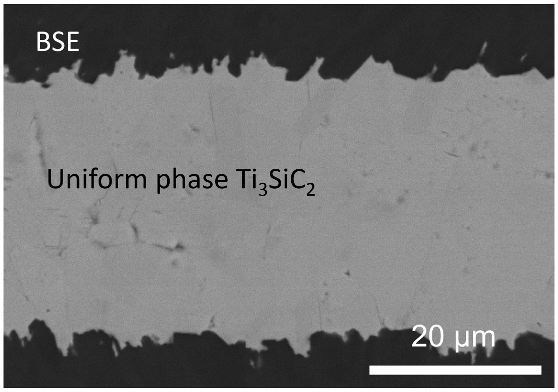

Fig. 5. As Fig.4, but hot pressed at 1500°C for 5 h.

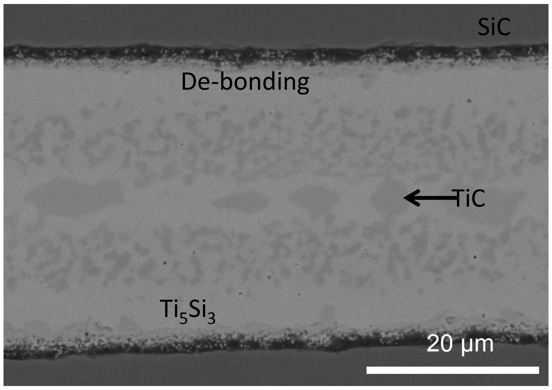

Fig. 6. As Fig. 4, but hot pressed at 1300°C for 1 h.

The Ti joint strengths of the specimens hot pressed under different conditions are listed in Table 1. The joints formed after hot pressing at 1500°C for 1 h show the highest shear strength of 98 MPa and acceptable standard deviation of 9 MPa. In contrast, the joints formed at 1300°C for 1 h show the lowest strength, some of which were actually broken during machining. These strength results are consistent with the microstructures presented in Figs. 4 and 6, showing good interfacial contact at 1500°C and interfacial de-bonding at 1300°C, respectively. The low strength provided by the Ti joints hot pressed at 1500°C for 5 h was surprising, because the uniform Ti_3SiC_2 phase formed was expected to show good strength due to the good CTE match with SiC. A small amount of oxygen (~8-9at%) was detected in the 5 h joint using SEM-EDS, but was absent in the Ti joint formed in 1 h hot pressing. Oxygen uptake during long duration processing may have led to the unexpected low joint strength. Ti sponge (as an oxygen getter) and hydrogen gas will be used during future hot pressing in order to eliminate oxygen in the furnace and eliminate oxide forming in the joint. The Ti joint hot pressed at 1500°C for 1 h exhibits the desired strength, therefore, its processing conditions have been chosen for fabricating the Ti joined CVD-SiC specimens to be produced for future irradiation tests.

Table 2. A review of processing conditions and joint microstructures reported in literature for CVD-SiC joined by Mo and Ti

Joining material	Reference	Foil thickness	Temperature (°C)	Pressure (MPa)	Time (h)	Phases	Findings
Mo foil	Cockeram [2], 1999	12.7	1200	8.8	10	no bonding	no reaction
		12.7	1500	3.4-17.2	10	Mo_5Si_3, Mo_2C	pressure no effect on microstructure
		25.4	1500	17.2	10	Mo_5Si_3, Mo_2C	more defects
	Cockeram [3], 2005	25.4	1500	17.2	10	Mo_5Si_3, Mo_2C	strength comparable to the monolithic SiC
Mo plate (Diffusion couple)	Martinelli [4], 1995	2.5 mm	1200	5	2	___	no flaw, but no image showed
		2.5 mm	1250	5	2	Mo_5Si_3, Mo_2C	Phases agglomerate and separated into two layers at high temperature
		2.5 mm	1300	5	1	Mo_5Si_3, Mo_2C	
		2.5 mm	1400	5	1	Mo_5Si_3, Mo_2C	
		2.5 mm	1500	5	0.2, 1	Mo_5Si_3, Mo_2C, Mo_5Si_3C	debonding at 1h, well contact at 0.2 h
		2.5 mm	1650	5	0.5	Mo_5Si_3, Mo_2C, Mo_5Si_3C, MoC	Mo_5Si_3/Mo_2C+ Mo_5Si_3 /Mo_5Si_3C/SiC complex microstructure
		2.5 mm	1700	5	1	Mo_5Si_3, Mo_2C, Mo_5Si_3C, MoC	
Ti foil	Cockeram [2], 1999	25.4	1500	3.4	10	Ti_3SiC_2, Ti_5Si_3	bad quality, more defects
		5.1	1500	8.8	10	Ti_3SiC_2, Ti_5Si_4	good quality, less defects
		25.4	1400	13.8	10	___	bad quality
	Gottselig [5], 1990	3	700		2	$TiC_{0.45}$	pressure >10 MPa, high strength
		3	1100		2	Ti_3SiC_2, $TiC_{0.45}$, Ti_5Si_3, $TiSi_2$	
		3, 1	1450	5, 15, 30	0.5, 1, 2	Ti_3SiC_2, Ti_5Si_3	
		3	1600		2	$TiC_{0.8}$	

Mo foil and powder joints

The results of a literature review on Mo foil joining of SiC and SiC/Mo diffusion are summ in Table 3. Similar to the Ti joining process, while pressure shows no effect on Mo joint q temperature and reaction time are the key factors controlling the Mo joint microstructure. joining was performed at temperatures of 1300, 1500, and 1700°C and pressures of 15 a MPa for 1 and 5 h (Table 1). Mo joints hot pressed at 1500°C and 1700°C for 1 h (Figs. 8) show similar microstructures: (1) vertical cracks though the joint indicate the brittle be of the formed joint; (2) Mo metal was completely reacted by forming the middle Mo_2C (region and the Mo_5Si_3 (dark) phase adjacent to the SiC base; (3) No debonding was fo the joint/base interface, indicating the good quality of joints formed under both condition (4) several pores (bubbles) were aligned at the middle of the joint, possibly related formation during reaction. Lower temperature, e.g. 1300°C, testing is included in the test but has not yet been performed. Hot pressing at 1500°C was extended to 5 h in or determine the time effect on the microstructural evolution of the Mo joint, shown in Complete Mo transformation to Mo_2C (bright) and Mo_5Si_3 (dark) phases were also obs However, interfacial de-bonding occurs at the bottom left and top right locations, deno arrows (Fig. 9), along with the Mo_2C band deviating from the middle of the joint and approa the SiC base in the debonding regions. De-bonding is likely owing to the large CTE mis between Mo_2C and SiC. While the formation mechanism of such tilted Mo_2C band morp is still under study, these results suggest good joint/base bonding can be achieved in 1 h excessive pressing is unnecessary. Lower temperature hot pressing was conducted at 1 for 5 h to study the temperature dependence of the Mo_2C band location. As shown in F the joint is well adhered to the SiC base. While the Mo_2C phase is very close to the SiC b thin layer of Mo_5Si_3 phase is observed between the SiC and Mo_2C, which possibly pre debonding. All those results indicate that short-time hot pressing is sufficient to obtain quality joints.

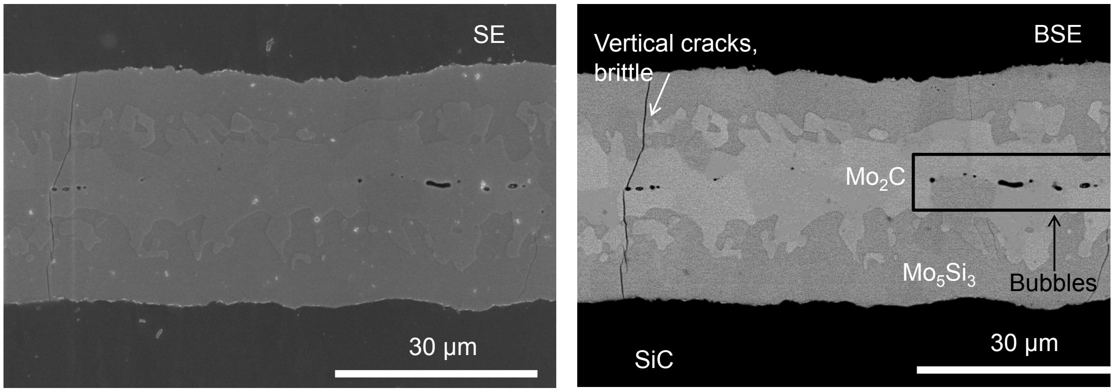

Fig, 7. Secondary electron (SE) and BSE images of joint formed between SiC plate and filler hot pressed at 1500°C for 1 h.

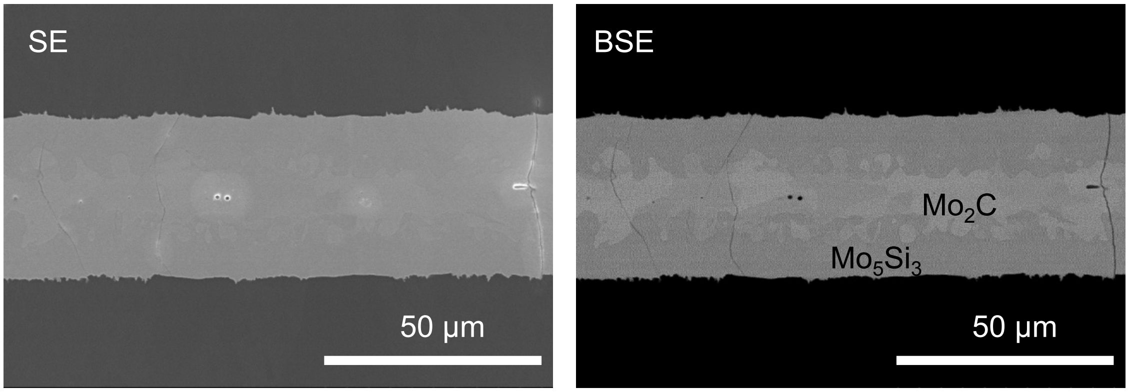

Fig. 8. SE and BSE images of Mo foil joint hot pressed at 1700°C for 1 h.

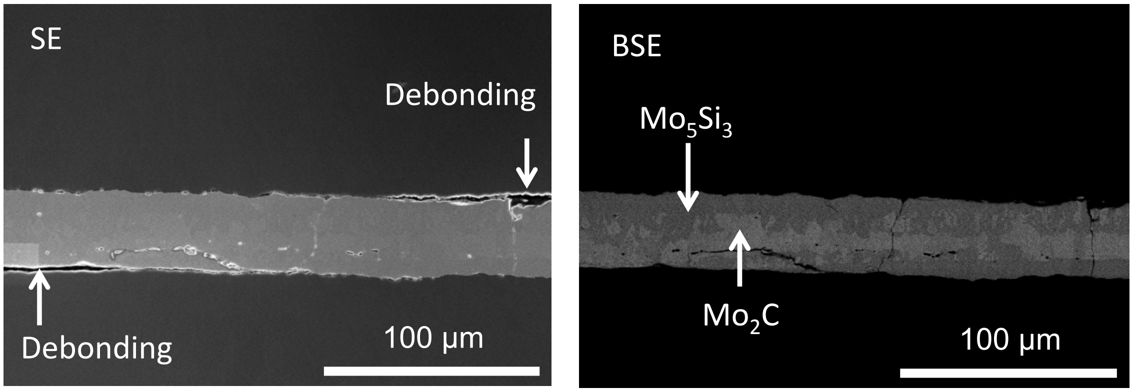

Fig. 9. SE and BSE images of Mo foil joint hot pressed at 1500°C for 5 h.

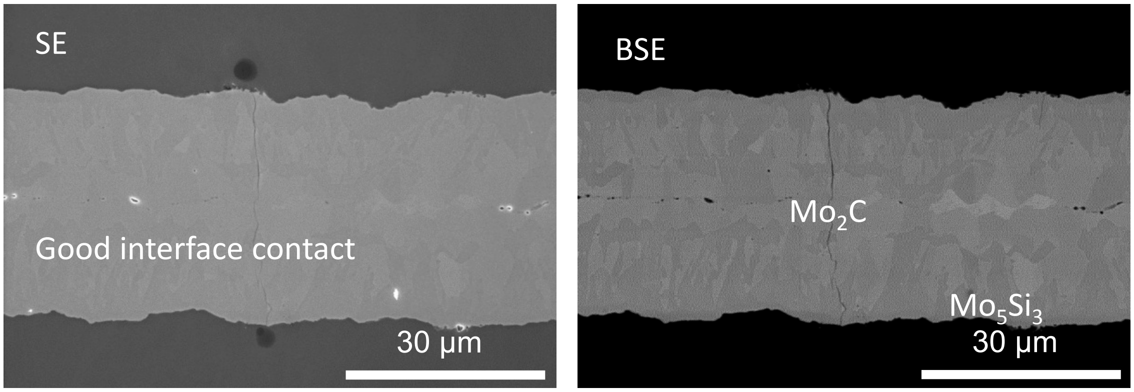

Fig. 10. SE and BSE images of Mo foil joint hot pressed at 1300°C for 5 h.

Another Mo joining approach was attempted by replacing the thin Mo foil with Mo powder slurry to study whether fine Mo powder can lead to a better joint by increasing the reactive surface area. The microstructures of Mo joints formed at 1500 and 1700°C in 5 h are shown in Figs. 11 and 12, respectively. The Mo slurry experienced significant volume shrinkage by gasification of binders and sintering during hot pressing, resulting in a joint exhibiting regions characterized as partial porous and partial dense. The dense joint has good contact with SiC (Fig. 12 b), whereas the porous joint usually leads to debonding at one side of the interfaces (Fig. 11 and Fig. 12 a). Therefore, Mo foil is favored over Mo powder slurry as the joining material because it experiences much less volume shrinkage during hot pressing.

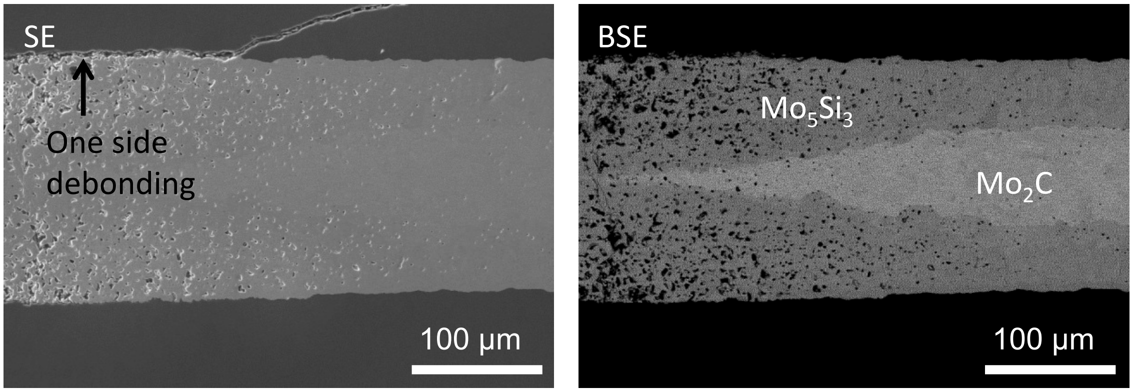

Fig. 11. SE and BSE images of joint formed between SiC plate using Mo slurry hot pressed at 1500°C for 5 h.

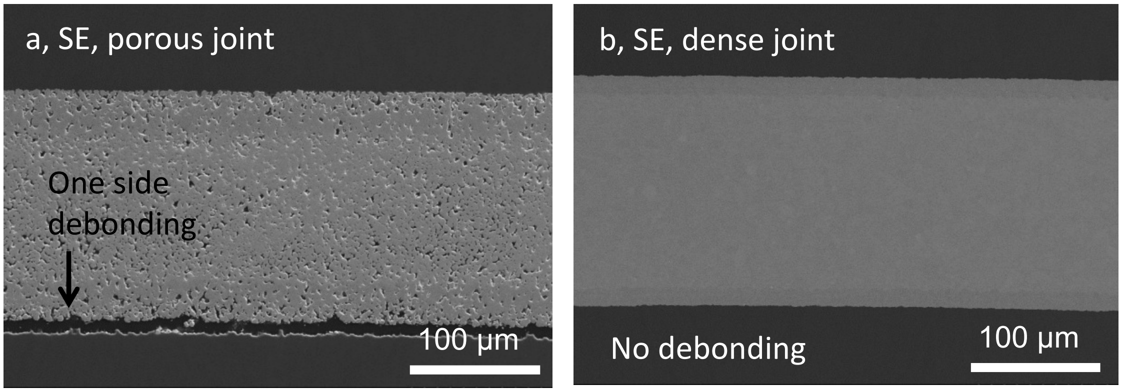

Fig. 12. SE images of partial porous (a) and partial dense (b) joint formed by hot pressing Mo powder slurry at 1700°C for 5 h.

The Mo joint strengths of specimens hot pressed under above conditions are listed in Table 1. The Mo joints formed by hot pressing Mo foil at 1500 and 1700°C for 1 h show good and comparable (within scattering range) shear strengths, which is consistent with the similar microstructure results shown in Figs. 7 and 8. The joint (foil) formed at 1500°C for 5 h shows lower shear strength around 20 MPa, which is predictable due to the interfacial debonding observed in Fig. 9. Surprisingly, the joint (foil) formed at 1300°C in 5 h also shows low shear strength around 15 MPa, even though debonding was not found in Fig. 10. Similar to the low strength results of the Ti foil joints hot pressed for 5 h, oxygen is suspected to have caused such low strength because a detectable amount of oxygen was observed in the Energy Dispersive X-ray spectrum of the joint (not shown here). An oxygen getter will be used in future Mo foil joining processes. All specimens joined by Mo powder slurry show low shear strength values, possibly due to interface debonding at the porous joint (Figs. 11 and 12). All microstructure and strength data shown above suggest using metal foils and short hot pressing time to achieve good joints.

NITE slurry joint

The microstructure of a NITE slurry joint hot pressed at 1860°C for 1 h at 20 MPa is shown in Fig. 13. Similar to the Mo slurry joint, partially dense and partially porous joints were also observed in NITE joints. The dense joint has good contact with the SiC base, but the porous joint has apparent debonding at both interfaces. This fair/bad unit is repeated along the joint, which is schematically illustrated in Fig. 14. Considerable volume shrinkage due to release of organic binders and sintering aids during hot pressing may lead to this observed microstructure. The shear strength of the NITE joint, shown in Table 1, is weak compared to the Ti and Mo joints. The fracture occurred at the joint/base interface and is possibly due to debonding at the porous joint (Fig. 13). Achieving a uniform and dense NITE joint with good contact with the SiC base is the key to guide future joining design.

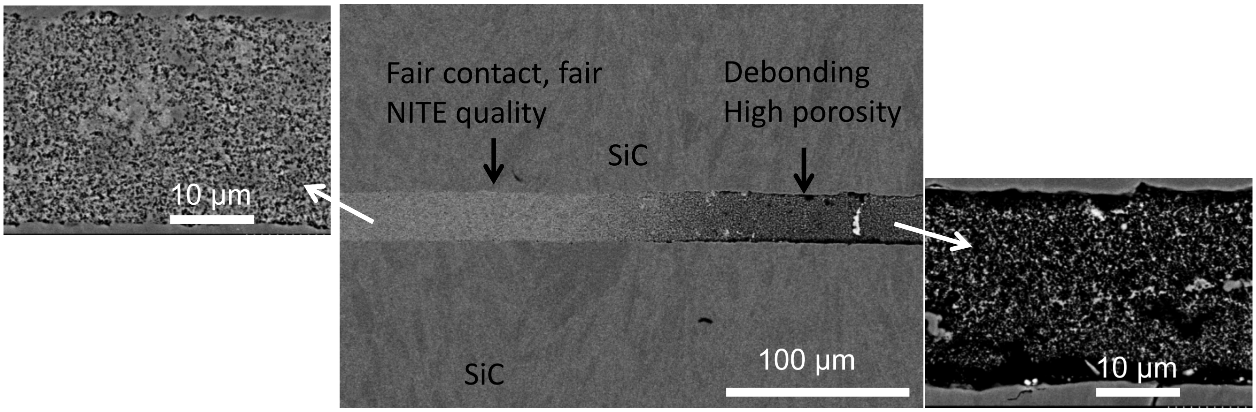

Fig. 13. BSE images of NITE slurry joint hot pressed at 1860°C for 1 h.

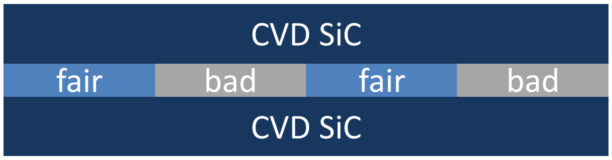

Fig. 14. Schematic of NITE slurry joint hot pressed at 1860°C for 1 h.

CONCLUSIONS

The candidate joint materials for the ongoing work to evaluate the neutron irradiation effect include chemically vapor-deposited (CVD) SiC bonded together with the NITE (nano-infiltration and transient eutectic-phase) – like transient eutectic phase processes, diffusion bonding utilizing active titanium or molybdenum inserts, calcia-alumina (CA) glass/ceramics, and Ti-Si-C

MAX phase through displacement reaction. Joint specimens were produced through the active metal insert methods and the NITE-like process then evaluated for as-fabricated properties during the present reporting period.

A high level summary of the status of joining development at Oak Ridge National Laboratory is provided in Table 3. The Ti foil insert joint of CVD SiC hot pressed at 1500°C for 1 h exhibited adequate strength. Hot-pressing at the lower temperature of 1300°C appeared sufficient to obtain a Mo joint of reasonable quality. Metal thin foils are favored over the powder slurries as the form of insert materials because of lower volume reduction during the pressurized process, used to form dense and uniform joints.

Table 3. Status summary of SiC joint processing at ORNL

Method	Insert Material	Status
Metallic diffusion bonding	Ti foil	Optimum joining condition established
	Mo foil	Optimum joining condition being studied
	Mo powder slurry	Optimum joining condition being studied
MAX-phase bonding	TiC/Si powder slurry	Commercial joining kit purchased
Transient eutectic-phase joining	NITE* slurry	Optimum joining condition being studied

*NITE: Nano-Infiltration and Transient Eutectic-phase process for sintering SiC

REFERENCES

[1] Y. Katoh, S. M. Dong, and A. Kohyama, *Fusion Eng. Des.* **61-2** (2002) 723-731.
[2] B. V. Cockeram, Bettis Atomic Power Laboratory, B-T-3255, (1999).
[3] B. V. Cockeram, *J. Am. Ceram. Soc.* **88** (2005) 1892-1899.
[4] A. E. Martinelli and R. A. L. Drew, *Mater. Sci. Eng. A* **191** (1995) 239-247.
[5] B. Gottselig, E. Gyarmati, A. Naoumidis, H. Nickel, *J. Eur. Ceram. Soc.* **6** (1990) 153-160.

4.1 High-Heat Flux Testing of Low-Level Irradiated Materials Using Plasma Arc Lamps —

A. S. Sabau, E. Ohriner, Y. Katoh, and L. L. Snead (Oak Ridge National Laboratory)

OBJECTIVE

The objective of this work is testing of irradiated materials that are candidate of divertor component materials and mock-up divertor components under high-heat flux using Plasma Arc Lamps (PAL).

SUMMARY

The high-heat flux testing facility using Plasma Arc Lamps was demonstrated at ORNL for W samples during a visit of the Japanese delegation of a PHENIX planning workshop. The second generation test section, which was designed by taking into account safety and materials compatibility requirements in order to handle the testing of low levels irradiated tungsten articles, was fabricated. The test sections were assembled and all the steps during the high heat flux runs were tested, including the air evacuation, backfill with Ar, and Ar pressure monitoring during the high heat flux testing, demonstrating the readiness of the new facility for irradiated samples.

PROGRESS AND STATUS

Introduction

Developing plasma-facing materials is a key challenge to the realization of the steady state high power levels that will be required in DEMO and future fusion power plants. Based primarily on high temperature performance and plasma poisoning issues the two candidate materials for PFC armor have been tungsten and carbon. However, for the case of ITER, and likely the next generation of deuterium-tritium fueled machines, tungsten appears the material of choice. In order to demonstrate the performance of these new materials and structures, the Plasma-arc-lamp facility at ORNL will be used with minor modification to provide fusion-prototypical steady state heat flux conditions.

This work specifically addresses (1) coupling of the material design effort with material testing, and (2) cost-effective testing, as specifically identified in the Fusion ReNeW roadmap as follows:

- thrust area 11 “Careful *coupling of the material design effort with material testing* will be required to advance a science-based development approach.” and “Such testing will need to proceed in a timely and *cost-effective* manner to ensure that the results are incorporated into improved material designs that will enhance the performance of the developed materials.”
- *thrust area 14* High heat flux testing will be aimed at “basic materials property information and models of materials behavior in the harsh fusion environment.”

There are several high heat flux (HHF) test facilities that provide thermal loads with power densities ranging from the MW/m^2 to several GW/m^2, and pulse durations ranging from a few hundred microseconds to almost continuous (Hirai et al., 2005; Coenen et al., 2011). For the static high heat flux testing, tests in electron beam facilities, particle beam facilities, IR heater and in-pile tests have been performed (Hirai et al., 2005). In this effort, only high heat flux (HHF) testing will be considered and the primary facility utilized will be the plasma arc lamp facility, a high-intensity infrared lamp. This technology has been successfully demonstrated for this purpose in the past for the High Average Power Laser inertial fusion program. Static heat loads corresponding to cycling loads during normal operation, are estimated to be up to 20 MW/m^2 in the divertor targets in ITER.

Tungsten coatings bonded to F82H steel have been successfully tested to greater than 10 MW/m^2 for one thousand cycles using the plasma arc lamp facility at ORNL (Romanoski, et al., 2005; Figure 5).

Experimental Procedure

In this project, as part of the material characterization of divertor armor, the testing is undertaken of actively cooled components under fusion specific (a) thermal loading conditions and (b) operational temperatures. The high heat flux testing at ORNL using the plasma arc lamp will aim at obtaining (1) basic materials property information and (2) formulating constitutive equations for models of materials behavior in the harsh fusion environment.

The second generation of Al enclosure was used in a high-heat flux testing demonstration. This 2G test section was assembled with all the safety and upgraded features (Figure 1 and 2), including:

(1) an optical pyrometer that was attached to the test section during in-situ measurements of the temperature of the Mo sample holder,
(2) a pressure valve that was installed for regulating the Ar pressure within the Al enclosure in order to prevent the liftoff of the main quartz window during the high heat flux testing.

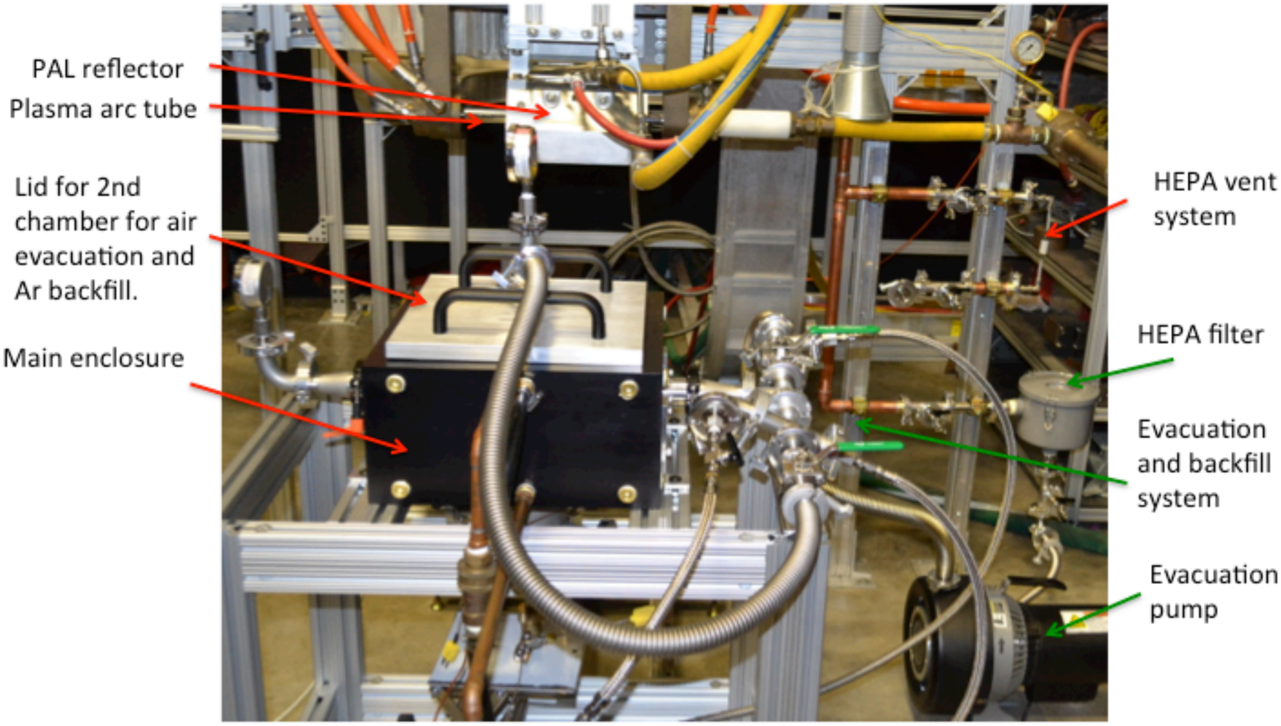

Figure 1. Aluminum enclosure (black anodized) as prepared for the evacuation procedure, showing major components of the system: arc lamp tube, PAL reflector, main Al enclosure, lid of top chamber, vacuum pump for the air-evacuation step, evacuation and backfill system including a HEPA filter and HEPA vent.

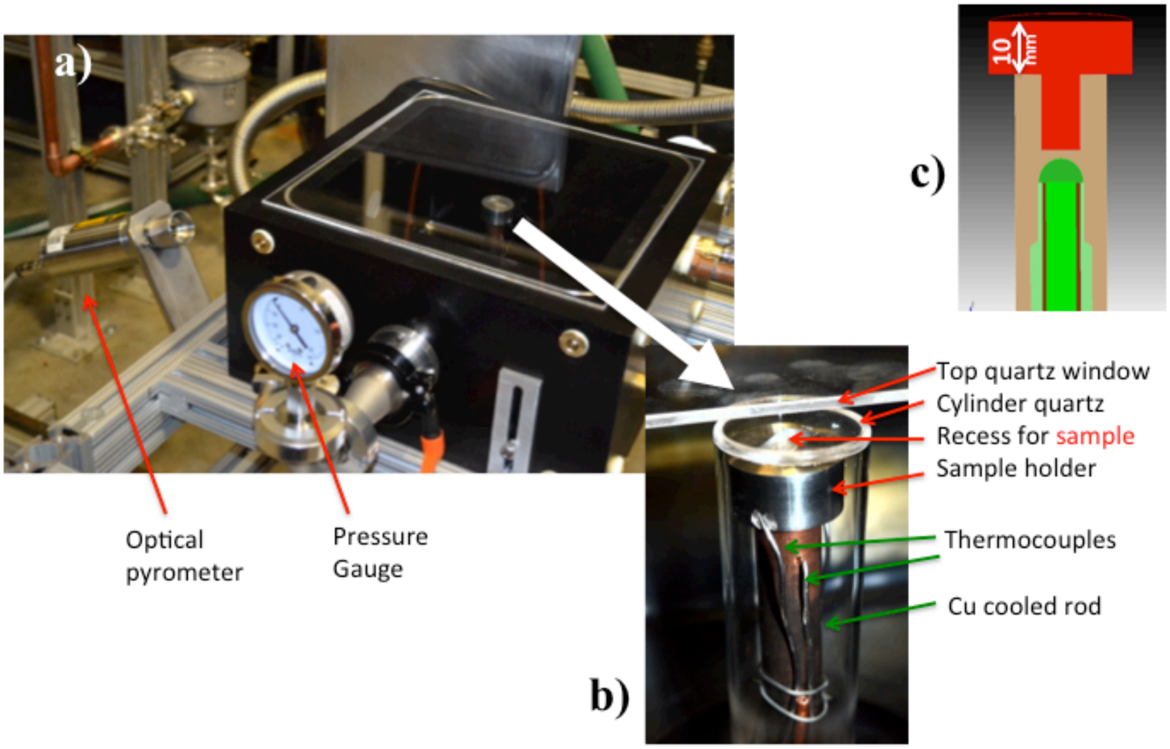

Figure 2. Experimental setup showing (a) panoramic top view showing the pressure gauge and pyrometer for in-situ surface temperature measurement of the Mo sample holder, (b) test stand composed of quartz cylinder for containment of volatile RAD gases, water cooled rod, Mo sample holder, and thermocouples, and (c) schematic of the cooling rod and Mo sample holder.

RESULTS

The test sections were assembled and proof-of-principle high-heat flux testing were conducted, demonstrating the readiness of the new facility. The locations of the thermocouples are shown in Figure 3. The temperature data during demonstration tests were obtained using the uniform reflector of the 750kW PAL at an estimated heat flux of 2 to 3 MW/m^2 at an offset distance of 3.2 to 2.5 cm. The heat flux measured at 2cm offset was 2.35 MW/m^2. It is estimated that the incident heat flux into the sample was approximately 1 MW/m^2. A typical temperature evolution during a demonstration test is shown in Figure 4. The duration of the first test was 30 s while the second test lasted approximately 10 min, during which four high heat flux pulses were generated. The temperature data were acquired during high-heat flux testing using a pyrometer and several thermocouples. The data shown in Figure 4, indicate that the pyrometer data is reliable and that it can be used in conjunction with those measured by thermocouples to estimate the sample temperature.

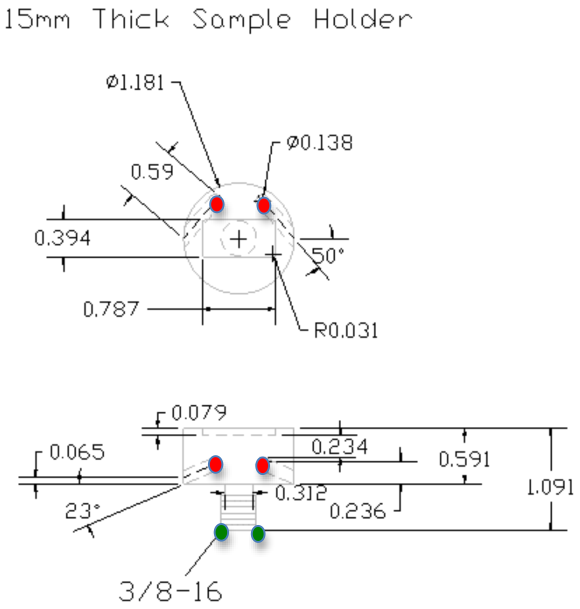

Figure 3. Location of thermocouples in the sample holder (red dots) and cooled rod (green dots). Dimensions are shown in inches.

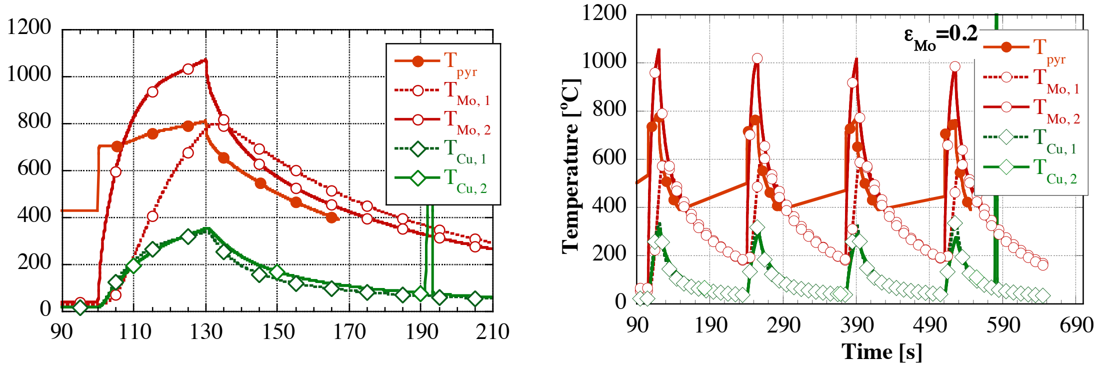

Figure 4. Typical temperature evolution during a demonstration test showing temperatures in the Mo sample holder (circle symbols) and in the Cu water-cooled rod (diamond symbols). The pyrometer temperature is indicated by the solid circle symbols: (a) one pulse of 30 s at 700 A, (b) four pulses of 15 s duration with 2 min idle at 800, 750, 725, and 700 A.

ACKNOWLEDGMENTS

The authors would like to thank Charles Ross (Chuck) Schaich for assisting with CAD design, fabrication specifications, and assembly; Jim Kiggans for design and fabrication of the Al enclosure, Alta Marie Williams for radiation safety considerations, and David Harper for operating the PAL.

REFERENCES

[1] T. Hirai, K. Ezato, and P. Majerus: "TER Relevant High Heat Flux Testing on Plasmas Facing Surfaces," *Mater. Trans.* **46**, 3 (2005) 412.

[2] J. W. Coenen, V. Philipps, S. Brezinsek, B. Bazylev, A. Kreter, T. Hirai, M. Laengner, T. Tanabe, Y. Ueda, U. Samm, and the TEXTOR Team, "Analysis of Tungsten Melt-Layer Motion and Splashing Under Tokamak Conditions at TEXTOR, *Nucl. Fusion* **51**, 083008 (11pp.), 2011.

[3] G. Romanoski, L. L. Snead, A. Sabau, J. Kelly, and S. J. Zinkle, "Bonding Tungsten to Low Activation Ferritic Steel," *HAPL Workshop*, LLNL, June 20-21, 2005.

4.2 Effect of Ti and TiC Additives on Sintering Behavior of Nano W — X. Wang and Z. Zak Fang (University of Utah)

OBJECTIVE

The objective of this research is to evaluate the effect of Ti and TiC additives on grain growth and densification behaviors of nano W powders produced by a high-energy planetary ball milling process.

SUMMARY

Ti and TiC were added as grain growth inhibitors during sintering of nano W alloys. The sintering of nano W, W-1Ti, W-1Ti-0.5TiC, W-1TiC powders were investigated to understand the effect of Ti and TiC addition on grain growth and densification. The results show that both Ti and TiC can effectively prevent W grain growth during sintering. However, the additives also adversely affect densification. The combinations of Ti and TiC appear to have promise to be used for achieving high density while retaining nanoscale grain size.

PROGRESS AND STATUS

Introduction

Nanoscale grain structure holds promise for improving ductility and fracture toughness of tungsten, which is a candidate for structural applications in future, fusion reactors [1-4]. Significant efforts have been put into consolidating nanocrystalline tungsten powders [5-7]. However there remains the challenge of achieving full densification while retaining nanoscale grain size. Our previous work [8] has shown a high energy milled nano tungsten powder can be sintered to 99% relative density at 1100 °C, a significantly lower than normal temperature, under hydrogen; but the final grain size after sintering is larger than 2 micrometers, far beyond the nanoscale.

For controlling grain growth of nano W, grain growth inhibitors based on second phase particles and solute segregation has been introduced in literature. The addition of second phase particles such as La_2O_3 and TiC to tungsten impedes the mobility of the grain boundaries. Kurishita et al., reported that with addition of 0.5 % TiC, the grain size of a compact HIPed at 1350 °C can be as small as 50 nm with 94% relative density. The inadequate densification was due to low temperature of HIPing used in their study, which was necessary to suppress grain growth [9]. Recently, the mechanisms of grain refinement based on solute segregation received a lot of interest in the research community. Butler et al reported alloying with Zr and Hf for producing ultrafine tungsten [10]. More recently, Chookajorn et al., demonstrated a W-20 at%Ti powder with stable grain size of about 20 nm after holding at 1100 °C in Argon for a week [11]. They explained that in a nanoscale structure an unexpected heterogeneous chemical distribution for a bulk equilibrium alloy contributed to the stable nanostructure.

It should be noted that grain growth and densification of nano powders are often accomplished by the same diffusion mechanisms [12]. In many cases, inhibiting grain growth of a powder can drastically reduce the ability to achieve full densification due to reduced diffusion, which is necessary for densification. In the present research, based on our previous work, we are engaged in a more in-depth study of doping nano W with grain growth inhibitors based on Ti and TiC and their combination, and study the correlations between the grain growth and densification versus the additions during sintering.

Experimental Procedure

Materials

Nano W, W-1Ti, W-1Ti-0.5TiC, W-1TiC powders were prepared by using a unique high-energy planetary ball milling (HEPM) process as illustrated in Figure 1. Our previous results have shown that the HEPM process significantly enhances the sinterability of the nanosized tungsten powders, achieving near-full density at much lower temperatures [8]. The powders were milled for 6 hours in heptane. Milled nano tungsten powders were compacted using a uniaxial press at 300 MPa. The green density was around 36% of theoretical density. Sintering experiments were carried out at temperatures between 950-1100 °C for 5 h in a hydrogen atmosphere using a tube furnace. Before sintering, the samples were reduced at 650 °C for 3 h in order to remove surface oxidation.

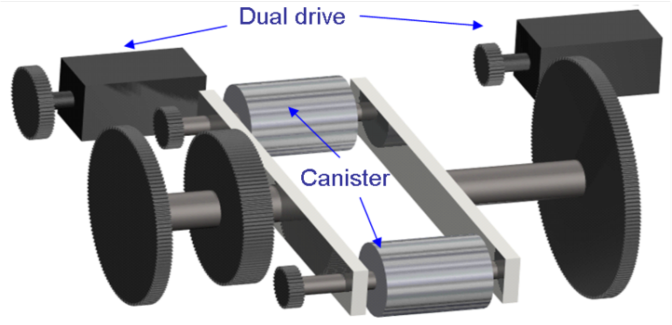

Figure 1. Schematic for the unique high energy planetary milling.

Characterizations

After sintering, the densities of the samples were measured by using Archimedes method. To take into account the influence of the initial as-pressed density, the sinterability of the powders can be expressed in terms of densification, which is calculated as follows:

$$Densification = \frac{Sintered\quad density - Green\quad density}{Theoretical\quad density - Green\quad density} \times 100\% \qquad (1)$$

The microstructural changes of the fractured surface of the sintered samples were observed using Scanning Electron Microscopy (SEM). Tungsten grain sizes were determined from the SEM micrographs by using the linear intercept method.

RESULTS

Milled Nano Powders

Figure 2 shows typical particle morphology of nano tungsten alloy powders produced by the high-energy planetary milling. The particle size of the most of the particles is in the range of 10–55nm. The average particle size is about 20 nm. It also shows that some particles agglomerate.

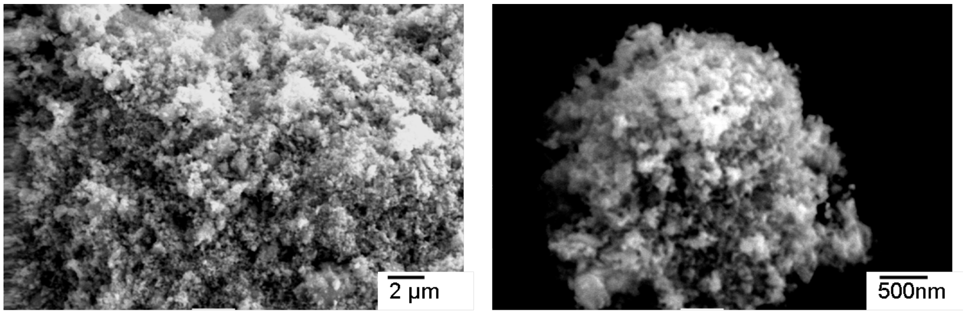

Figure 2. SEM images of high energy planetary ball milled nano W-1Ti powder

Microstructure Evolution versus Temperature

To study the effects of Ti and TiC additions on sintering behaviors of W, 4 nano powders of W, W-1Ti, W-1Ti-0.5TiC, and W-1TiC were sintered in the temperature range of 950-1100 °C. SEM microstructural examinations were conducted to observe the evolution of the tungsten grain structure vs. temperature for different powders, as shown in Figures 3-6. It can be seen in Figure 3 that W grains without any additives grow very rapidly with the increase of temperature, which is consistent with our prior results. In fact considerable WC grain growth occurred below 950 °C. At 950 °C, the W grains have grown to more than 100 nm. In contrast, Figures 4-6 demonstrates the addition of Ti and TiC to W grains effectively shifts the onset temperature of the W grain growth to higher temperature. Note that the temperatures for the surface morphologies of the W particles becoming smoothed and faceted were also delayed with the addition of the Ti and TiC.

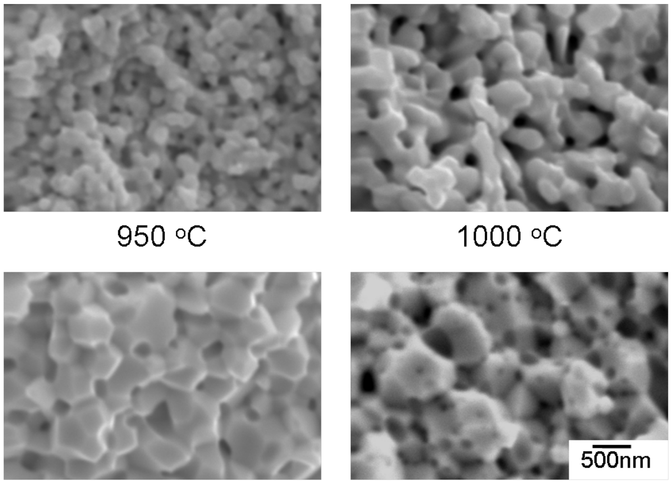

950 ^{o}C 1000 ^{o}C

1050 ^{o}C 1100 ^{o}C

Figure 3. SEM images of fracture surface of sintered nano W at different temperatures.

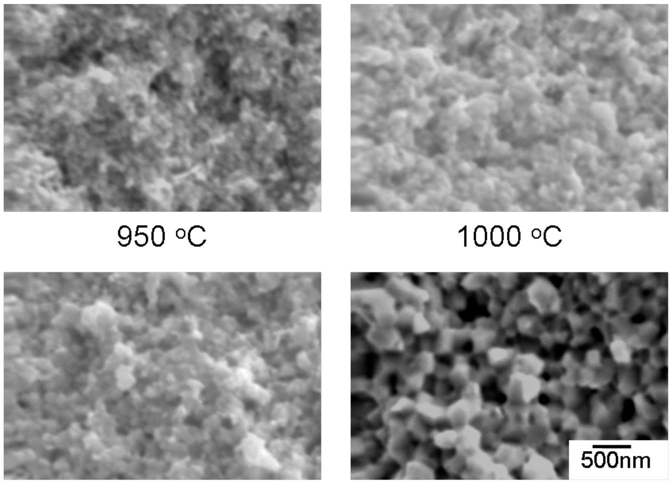

950 ^{o}C 1000 ^{o}C

1050 ^{o}C 1100 ^{o}C

Figure 4. SEM images of fracture surface of sintered nano W-1Ti at different temperatures.

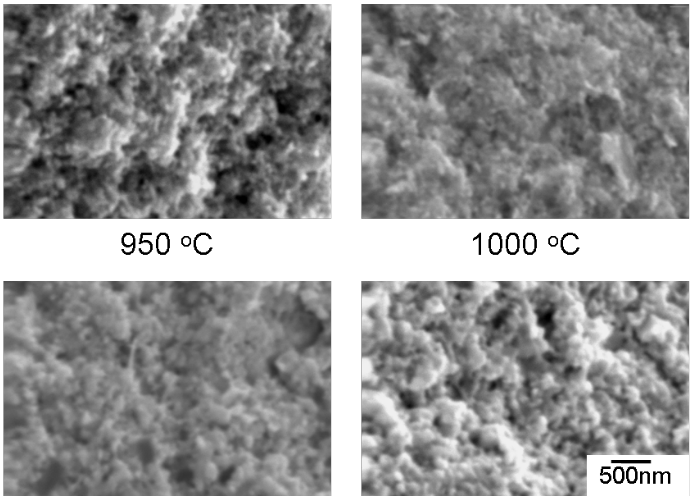

950 °C 1000 °C

1050 °C 1100 °C

Figure 5. SEM images of fracture surface of sintered nano W-1Ti-0.5TiC at different temperatures.

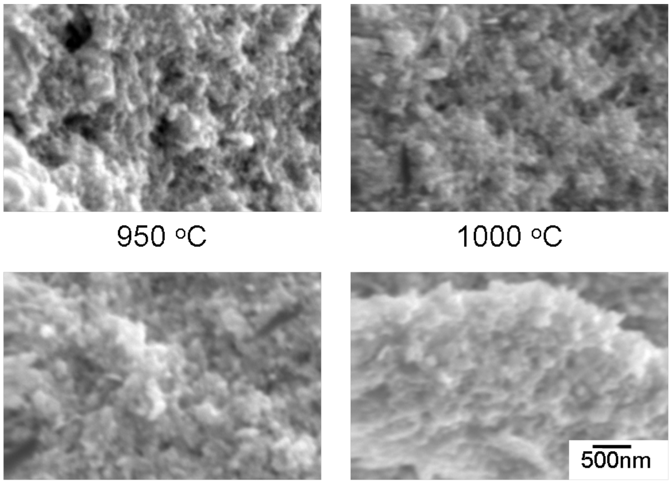

950 °C 1000 °C

1050 °C 1100 °C

Figure 6. SEM images of fracture surface of sintered nano W-1TiC at different temperatures.

Grain Growth and Densification Behaviors

Figure 7 plots the W grain size and densification as function of sintering temperature between 950-1100 °C. It is obvious that the addition of Ti or TiC has significant effects on W grain growth and densification of the powders. According to the curves, both Ti and TiC results in low densification rate. 1 wt% of TiC severely retard the densification. When combined with Ti, 0.5 wt% of TiC shows little effect on the densification. As grain growth inhibitor, TiC is more effective than Ti. Ti is not so effective to limit the W grain growth in the intermediate densification stage when the temperature is over 1000 °C, probably due to Ti starts to facilitate the diffusion of tungsten. The grain size vs densification trajectories for the 4 powders were examined in Figure 8. The slope of the sintering trajectory of the W powder was significantly lowered with the addtion of Ti and TiC.

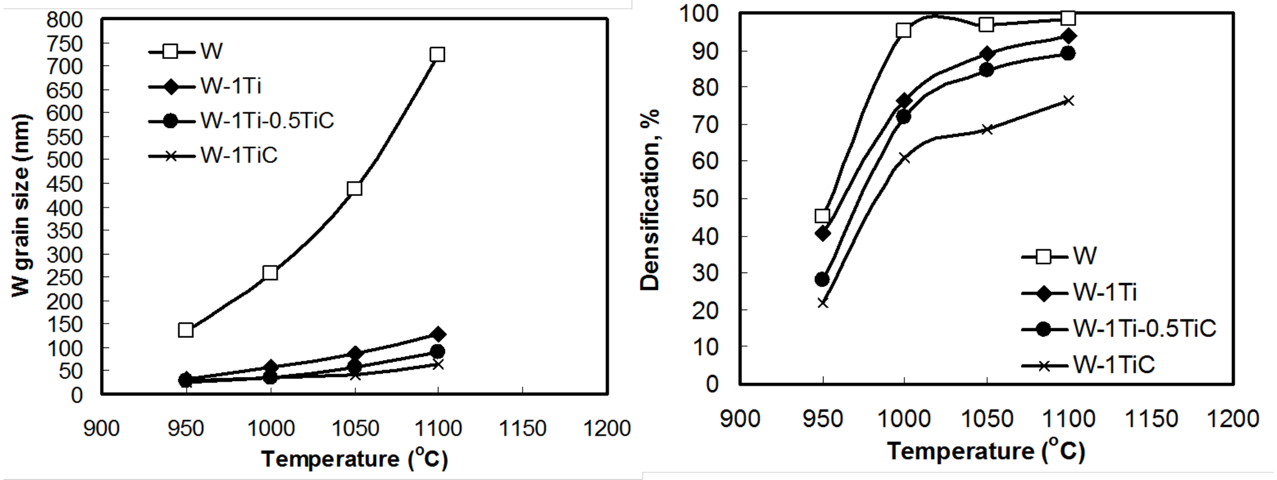

Figure 7. Grain size and densification as function of temperature during sintering of nano powders

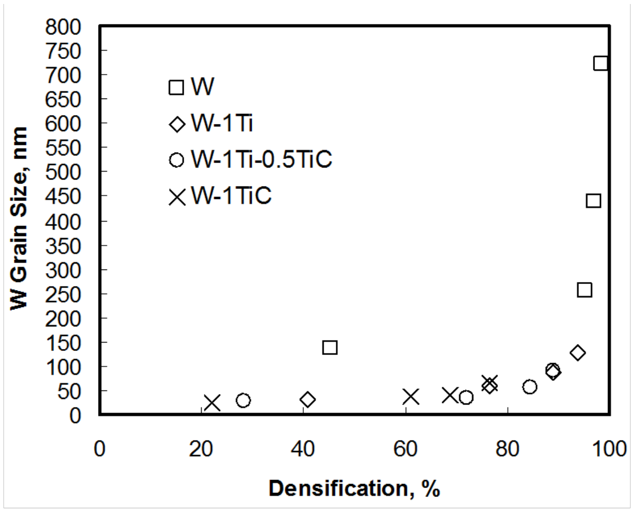

Figure 8. Grain size vs. Densification during sintering of nano W, W-1Ti, W-1Ti-0.5TiC, W-1TiC powders

Future work

The composition of W-Ti-TiC alloys will be optimized to achieve high density and minimized grain size.

REFERENCES

[1] M. Rieth, et al., *J. Nucl. Mater.* **432** (2011) 482-500.
[2] M. Jain, et al., *Int. J. Powder Metall.* **42** (2006) 53.
[3] Q. Wei, K. T. Ramesh, E. Ma, et al., *Acta Mater.* **54** (2006) 54.
[4] L. J. Kecskes, K. C. Cho, R. J. Dowding, et al., *Mater. Sci. Eng.* **467** (2007) 33.
[5] O. El-Atwani, D. V. Quach, M. Efe, et al., *Mater. Sci. Eng. A* **528** (2011) 5670.

[6] K. C. Cho, *Mater. Manuf. Process.* **19** (4) (2004) 619.
[7] A. Mondal, A. Upadhyaya, and D. Agrawal, *Int. J. Refract. Met. Hard Mater.* **28** (2010) 597.
[8] H. Wang and Z. Z. Fang, *Int. J. Refract. Met. Hard Mater.* **28** (2010) 312.
[9] Y. Kitsunai, et al., *J. Nucl. Mater.* **271-272** (1999) 423.
[10] B. G. Butler, et al., in Proceeding of 2011 Tungsten Conference (2011) 05-42.
[11] T. Chookajorn, H. A. Murdoch, and C. A. Schuh, *Sci.* **337** (2012) 951.
[12] X. Wang, Z. Z. Fang, and H. Y. Sohn, *Int. J. Refract. Met. Hard Mater.* **26** (2008) 232.

4.3 Effects of B, C, N, O, P AND S Impurities on Tungsten $\Sigma 27[110]\{552\}$ and $\Sigma 3[110]\{112\}$ Grain Boundaries — W. Setyawan and R. J. Kurtz (Pacific Northwest National Laboratory)

OBJECTIVE

The objective of this research is to support the design of tungsten-based materials with increased fracture resistance using first-principles computational methods.

SUMMARY

Density functional theory was employed to investigate the effects of B, C, N, O, P and S impurities on the properties of W $\Sigma 27[110]\{552\}$ and $\Sigma 3[110]\{112\}$ grain boundaries (GBs). Careful search of interstitial sites near the interfaces resulted in 19 and 9 unique interstices in $\Sigma 27$ and $\Sigma 3$ respectively. By using the segregation energy as a weighing factor, the average intergranular fracture energies were calculated. It was found that B, C, N and P increase the cohesion of $\Sigma 27$ by 10.1, 8.9, 4.1 and 2.5% respectively, while O (0.6%) and S (2.7%) embrittle the GB. In $\Sigma 3$, only C was found to strengthen the interface by 1.2%, while B, N, O, P and S decrease the intergranular cohesion by 1.7, 1.6, 11.2, 18.4 and 19.4% respectively. The impurity content in this study was 1.37 atoms/nm^2.

PROGRESS AND STATUS

Introduction

The development of novel W-based materials that are suitable for future fusion reactors is likely to involve synergistic advancements in intrinsic W alloys [1, 2], grain boundary (GB) engineering [3, 4] and W-based composites [5, 6]. In all of these areas, understanding and controlling the characteristics of materials at intergranular regions are important. Using first-principles methods, we have recently started to study more closely the effects of impurities on the GB cohesion in tungsten. In particular, $\Sigma 27a[110]\{552\}$ and $\Sigma 3a[110]\{112\}$ were used to model the high- and low-angle interfaces. We performed careful search of interstitial sites near the interface for each GB. In this article, we report the results for B, C, N, O, P and S impurities.

Formalism

The GB structures were initially relaxed using classical molecular dynamics (MD) utilizing the Finnis-Sinclair type of interatomic potential developed by Ackland and Thetford [7]. Systematic interfacial shifts and atoms relaxations were done to achieve the most stable configurations. The structures obtained from the MD were further optimized via an *ab initio* method. VASP software was used to perform the quantum mechanical calculations based on the plane-wave density functional theory (DFT). Accurate projector-augmented-wave pseudopotentials with Perdew-Burke-Ernzerhof exchange correlations were employed [8–10]. The number of valence electrons for W, B, C, N, O, P and S is 6, 3, 4, 5, 6, 5 and 6 with plane-wave energy cutoff of 223.1, 318.6, 400.0, 400.0, 400.0, 270.0 and 280.0 eV, respectively. The calculations were done using Monkhorst-Pack **k**-points grid of 5×5×1. These settings were needed to achieve convergence < 1 meV.

RESULTS

The necessary slab thickness for the DFT calculations was determined from the convergence tests of the {552} and {112} surface energies, namely 62 layers for the Σ27 and 23 layers for the Σ3 [11]. Figure 1 shows the relaxed structure of the GBs. For Σ27, the dimensions of the simulation cell converged to 8.2, 8.9 and 50.1 Å along x, y and z respectively. The thickness of the 62 {552}-layers was 26.7 Å, leaving enough vacuum to ensure no interaction between the free surfaces. For Σ3, the simulation cell converged to 8.2, 8.9 and 50.1 Å along x, y and z respectively. The thickness of the 23 {112}-layers was 29.6 Å. In Figure 1, the atoms are arranged in two alternating layers along [110] (-y). Tungsten atoms are plotted in dark or light gray depending on which layer they reside. The simulation cell of both GBs contains four such layers for a total of 124 W atoms (Σ27) and 138 W atoms (Σ3). Periodic boundaries were applied along x and y.

Initially, the set of interstitial voids (interstices) was determined within 3.5 Å from the GB plane. Nineteen unique interstices were found. For the Σ3, nine unique interstices were found. In Figure 1, the interstices are shown in small red spheres and labeled based on the nearest-neighbor distance r_{nn} with interstice 1 having the shortest r_{nn}. Two additional interstices labeled *oct* and *tet* are shown near atom *U*. They represent bulk-like interstices possessing octahedral and tetrahedral coordination. The *oct* interstice is located behind atom *U* and midway between atoms *V*.

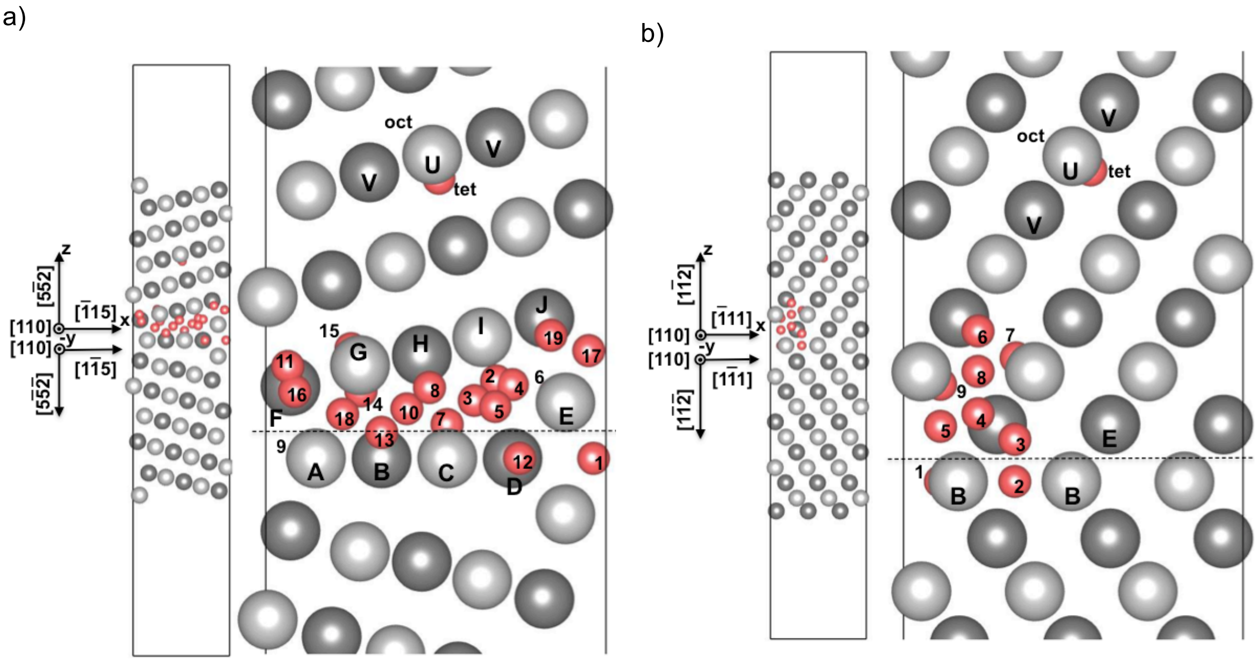

Figure 1. a) Structure of the W Σ27a[110]{552} tilt GB viewed along the [110] (-y). The initial positions of interstices are shown in red spheres from 1 to 19. Interstices 6 and 9 are located behind atoms *E* and *A* respectively. Interstice with octahedral coordination (*oct*) is behind atom *U* midway between atoms *V*. Interstice with tetrahedral coordination is labeled as *tet*. B) Structure of the W Σ3a[110]{112} tilt GB and the positions of interstices labeled from 1 to 9.

For the determination of the GB segregation energy E_{sg}, a reference site needs to be determined. For each impurity, the reference site is determined from the more stable site between *oct* and *tet* sites. The impurity binding energy E_b and GB segregation energy E_{sg} were defined as:

$$E_b = E - (E_W + E_I) \tag{1}$$

$$E_{sg} = E_{ref} - E \tag{2}$$

E denotes the total energy of the system with an impurity at an interstice, E_W is the total energy with only W atoms, E_I is the energy of an isolated impurity, E_{ref} is the total energy with an impurity at the reference site. The interstitial binding energies in body-centered cubic (bcc) W are presented in Table 1. Negative E_b represents an attractive interaction. Boron, C, N and O are attracted to W while P and S are repelled. Carbon is the most binding, followed by N, O and B. For all impurities in this study, *oct* is more stable than *tet* ($E_{ref} = E_{oct}$) except for O ($E_{ref} = E_{tet}$). With these references, the segregation energy at each GB interstice was calculated and summarized in Table 2. Positive values indicate tendency for segregation to the interface. Strong tendencies were observed for all the impurities considered here, particularly in Σ27. Despite the fact that B, C, N and O exhibit strong binding in bcc, their GB segregation energies are large ranging from approximately 1 to 3.5 eV. Meanwhile, as expected, P and S exhibit the largest segregation energy due to their repulsive nature with W atom with the segregation energies ranging from approximately 1 to 8.5 eV.

Table 1. Binding energy E_b (eV) of impurities at octahedral (*oct*) and tetrahedral (*tet*) interstitial site in bcc W. Negative value indicates attraction.

	B	C	N	O	P	S
oct	**-5.107**	**-8.399**	**-8.091**	-5.120	**0.393**	**1.588**
tet	-3.522	-6.897	-7.326	**-5.396**	0.529	1.738

Table 2. Segregration energy E_{sg} (eV) of impurities at various interstices in W Σ27 and Σ3 GBs. Positive E_{sg} indicates tendency to segregate to the GB.

Σ27	1	2	3	4	5	6	7	8	9	10
B	2.206	3.575	3.575	3.576	3.575	3.569	3.577	3.606	2.260	3.545
C	2.115	2.688	2.687	2.688	2.687	2.846	2.683	1.955	0.769	1.966
N	2.176	2.721	2.719	2.721	2.720	3.311	2.714	2.296	1.514	2.297
O	2.109	2.973	3.282	2.973	3.282	3.612	3.038	2.629	1.776	2.635
P	5.788	7.700	7.702	7.700	7.703	7.697	8.226	7.704	5.783	7.689
S	5.211	6.958	6.865	6.958	6.885	6.554	7.090	6.869	5.212	6.722
	11	12	13	14	15	16	17	18	19	
B	2.177	0.226	1.659	3.643	3.242	2.169	3.656	0.986	0.430	
C	2.148	0.456	1.054	3.118	3.113	2.148	1.646	1.117	0.509	
N	2.129	1.185	1.524	1.287	3.145	2.131	2.920	1.290	0.619	
O	3.446	1.645	2.636	1.947	2.962	3.448	3.449	1.958	3.448	
P	8.118	2.657	4.587	8.031	8.038	8.392	8.347	8.123	8.382	
S	7.113	3.128	6.861	7.196	7.203	8.040	8.002	7.091	8.009	
Σ3	1	2	3	4	5	6	7	8	9	
B	1.506	1.507	1.540	1.541	0.681	0.171	0.334	0.672	0.683	
C	1.562	1.562	1.569	1.566	0.642	0.188	0.039	0.648	0.636	
N	1.720	1.717	1.723	1.723	-0.334	0.247	0.432	0.684	0.671	
O	1.807	1.228	0.737	0.471	0.780	0.190	0.339	0.903	0.323	
P	2.908	2.915	3.030	3.026	2.906	0.127	0.838	1.618	0.806	
S	2.896	2.895	3.033	2.994	3.006	0.258	0.861	1.587	0.874	

The effect of impurities on the GB cohesion was studied by calculating the intergranular fracture energy E_{if} as follows:

$$E_{if} = E_{top} + E_{bot} - E \tag{3}$$

$$\Delta E_{if} = E_{if} - E_{if,clean} \tag{4}$$

$$\left\langle E_{if} \right\rangle = \left(\sum_{E_{sg,i}>0} E_{sg,i} E_{if,i} \right) / \sum_{E_{sg,i}>0} E_{sg,i} \tag{5}$$

$$\Delta \left\langle E_{if} \right\rangle = \left\langle E_{if} \right\rangle - E_{if,clean} \tag{6}$$

To obtain the fractured configurations, the system was separated into two subsystems containing atoms below (for the bottom half) or above (for the top half) the fracture plane (dash line in Figure 1). E_{top} and E_{bot} are the total energies of the top and bottom halves respectively. $E_{if,clean}$ denotes the fracture energy of the clean Σ27 (4.16 J/m^2) or Σ3 (6.18 J/m^2). As a first approximation, a measure of an average fracture energy <E_{if}> was introduced by using the segregation energy as a weighing factor. Only interstices with E_{seg} > 0 were included in the summation. In this formulation, if an impurity is more stable at the bulk than at a GB interstice, then its contribution at this interstice is zero as would be expected.

Figure 2 shows the distribution of E_{if}. The horizontal lines mark the intergranular fracture energies of the clean GBs. The influence of impurities significantly depends on the interstices as evident from Figure 2. The ranges of the $\Delta E_{\mathrm{if}}/E_{\mathrm{if,clean}}$ are summarized in Table 3 and given in percentage. In general, the impurities affect the GB cohesion more adversely in low-angle GBs than in high-angle ones. Note that in this study, both GBs have the same interface area; hence the comparison is based on the same impurity content of 1.37 atoms/nm^2. From the average values, it was indicated that B, C, N and P increases the cohesion of $\Sigma 27$ by 10.1, 8.9, 4.1 and 2.5% respectively, while O (0.6%) and S (2.7%) embrittle the GB. In $\Sigma 3$, only C was found to strengthen the interface by 1.2%, while B, N, O, P and S decreases the intergranular fracture energy by 1.7, 1.6, 11.2, 18.4 and 19.4% respectively.

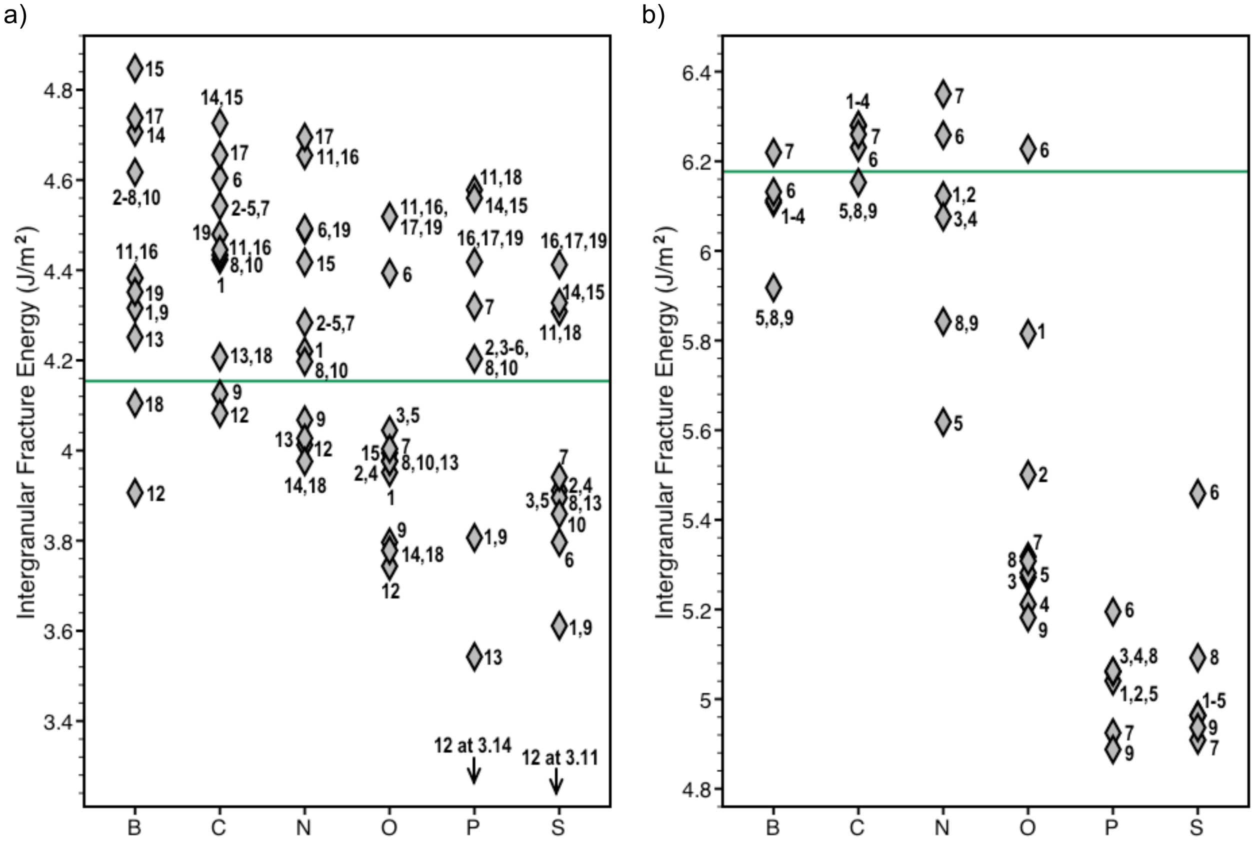

Figure 2. Intergranular fracture energy of a) W Σ27a{552} and b) W Σ3a{112} GBs with an impurity at various interstices. The lines at 4.16 and 6.18 J/m^2 mark the fracture energies of the pure GBs.

Table 3. Intergranular fracture energy change ΔE_{if} due to an impurity at various interstices in W $\Sigma27\{552\}$ and $\Sigma3\{112\}$ GBs. The minimum, maximum and average (bold face) values are given. The average effect was calculated using the segregation energy as a weighing factor. All values are normalized relative to the fracture energy of the clean interfaces and given in percentage. Positive numbers indicate an increased GB cohesion.

	B	C	N	O	P	S
Σ27	-5.9,16.7,**10.1**	-1.7,13.8,**8.9**	-4.3,13.0,**4.1**	-9.9,8.8,**-0.6**	-24.5,10.2,**2.5**	-25.2,6.2,**-2.7**
Σ3	-4.2,0.7,**-1.7**	-0.4,1.7,**1.2**	-9.0,2.8,**-1.6**	-16.1,0.8,**-11.2**	-20.9,-15.9,**-18.4**	-20.5,-11.6,**-19.4**

Computations were performed partly on Olympus supercomputer (FUSION account) at Pacific Northwest National.

REFERENCES

[1] Y. Mutoh, et al., *J. Mat. Sci.* **30** (1995) 770.
[2] S. Wurster, et al., *J. Nucl. Mater.* **413** (2011) 166.
[3] L. J. Kecskes, et al., *Mater. Sci. Eng. A* **467** (2007) 33.
[4] M. Faleschini, et al., *J. Nucl. Mater.* **367** (2007) 800.
[5] E. Lassner and W. -D. Schubert, “Tungsten”, Springer (1995).
[6] Y. Ishiyama, et al., *Mater. Sci. Eng. A* **473** (2008) 7.
[7] G. J. Ackland and R. Thetford, *Phil. Mag. A* **56** (1987) 15.
[8] P. E. Blöchl, *Phys. Rev. B* **50** (1994) 17953.
[9] G. Kresse and D. Joubert, *Phys. Rev. B* **59** (1999) 1758.
[10] J. P. Perdew, K. Burke, and M. Ernzerhof, *Phys. Rev. Lett.* **77** (1996) 3865.
[11] W. Setyawan and R. J. Kurtz, *Scrip. Mater.* **66** (2012) 558.

5.1 Irradiation Response of Next Generation High Temperature Superconducting Rare-earth and Nanoparticle-Doped $YBa_2Cu_3O_{7-x}$ Coated Conductors for Fusion Energy Applications

— K.J. Leonard, T. Aytug (Oak Ridge National Laboratory), A. Perez-Bergquist, W.J. Weber (University of Tennessee), and A. Gapud (University of South Alabama)

OBJECTIVE

The goal of this work is to evaluate the irradiation response of the newest generation of coated conductors based on rare earth and nanoparticle doping of the $YBa_2Cu_3O_{7-x}$ (YBCO) high temperature superconductor. The materials under investigation represent different methods for enhanced flux pinning for improved performance under externally applied magnetic fields. Ion beam irradiation will be used to simulate neutron damage cascades in the materials to examine the effect that radiation damage has on the different pre-existing defect structures used for flux pinning and to assess the superconductors capability for use in fusion reactor systems.

SUMMARY

The pre-irradiation electrical and microstructural characterization of three advanced high temperature superconductors has been completed and is discussed in this report. These conductors represent three distinct ways in which increased performance and improved flux pinning have been achieved through means of rare earth and nanoparticle doping. The $GdBa_2Cu_3O_{7-x}$ conductor primarily utilizes stacking fault and anti-domain defects in its structure to enhance magnetic flux pinning in the B//ab direction. Disperse $(Dy,Y)_2O_3$ nano-particles dominate the microstructure of the $(Y,Dy)Ba_2Cu_3O_{7-x}$ conductor which also shows enhanced B//ab pinning. The Zr-doping of $YBa_2Cu_3O_{7-x}$ produces c-axis aligned $BaZrO_3$ nanoparticles to produce enhanced B//c pinning and a reduced field dependence of the critical current density. Irradiation experiments using 25 MeV Au ions will begin at the start 2013, from which the response behavior of these advanced conductors will be evaluated.

PROGRESS AND STATUS

Introduction

In an effort to reduce reactor complexity and costs, the ORNL Fusion Materials Program is evaluating the irradiation response of the newest generation of $YBa_2Cu_3O_{7-x}$ (YBCO) high temperature superconducting (HTS) materials for possible qualification in future magnetic confinement reactor designs. In addition to the higher critical temperature over currently used Nb_3Sn ($T_c = 92$ K versus 18 K for Nb_3Sn), YBCO conductors offer higher critical current density (J_c) values, a smaller flux pinning coherency length that can produce J_c increases on exposure to neutron irradiation up to $1x10^{22}$ n/m^2 (E>0.1 MeV) [1-10] and a smaller effective neutron capture cross section. However, in the past, HTS materials have been limited to self-field applications such as power transmission cables due to their inability to maintain magnetic flux pinning under externally applied fields [10-11]. The newest generation of YBCO conductors incorporate the use of engineered textured substrates and nanoparticle additions to the conductor to produce correlated defect structures in the YBCO lattice that increase J_c values with reduced dependence on magnetic field [13-18].

The first stage of this work is to examine the room temperature ion-irradiated properties of the latest generation of rare earth and nanoparticle doped YBCO coated conductors for their potential use in nuclear environments. Providing a first investigation into both the radiation-induced generation of defects and the changes to pre-existing pinning centers for these materials. Establishing a fundamental understanding of the irradiation properties of these nano-doped materials may lead to further development of new ceramic materials used in diagnostic systems for ITER, DEMO and eventual fusion power plants.

Materials

The materials include $(Y,Dy)Ba_2Cu_3O_{7-x}$ supplied by American Superconductor (AMSC), $Gd_2Ba_2Cu_3O_{7-x}$ and Zr-doped $(Y,Gd)Ba_2Cu_3O_{7-x}$ purchased from SuperPower (SP). At this time, Nb-doped YBCO material has not been fabricated due to budgetary considerations, as this material will require in-house fabrication. The $GdBa_2Cu_3O_{7-x}$ (GBCO) tapes will represent a condition in which nanoparticles are not introduced into the standard $YBa_2Cu_3O_{7-x}$ conductor. The substitution of Gd for Y in the 123 structure offers a high performance conductor, which is in-line with the general goals of this research in examining high performance production quality tapes. Furthermore, cables made of GBCO based conductors demonstrate less critical current dependence, or degradation, to cable straining than YBCO based conductors for the same buffer/substrate architecture as used in this study [19,20]. A list of the materials of interest to this study and the general features of the HTS layer are provided in Table 1. The buffer architecture for the AMSC and SP produced tapes is illustrated in Figure 1. The high temperature superconducting (HTS) layers are produced through metalorganic chemical vapor deposition (MOCVD) onto the buffered Ni-alloy tapes. The biaxial texturing of the YBCO needed for superconducting current flow along the length of tape is generated from either the rolling assisted bi-axial texturing of the metallic substrate, AMSC architecture, or developed within the buffer layer as in the case of the SP materials.

Table 1. List of the high temperature superconductors, substrate architecture (listed by company name from which tapes were fabricated) and the type of flux pinning created for improved use in magnetic field applications.

Material	Substrate	Features
$(Y,Dy)Ba_2Cu_3O_{7-x}$	American Superconductor	50% substitution of Y in $YBa_2Cu_3O_{7-x}$ chemistry. Development of $(Dy,Y)_2O_3$ nanoparticles, enhanced H//ab pinning. Increased stacking faults ($YBa_2Cu_4O_8$ intergrowths) in the film.
$GdBa_2Cu_3O_{7-x}$	SuperPower	Substitution of Gd for Y in the $YBa_2Cu_3O_{7-x}$ chemistry. High density stacking fault generation from mismatch in growth domains from buffer and Gd_2O_3 particles, yielding improvements in H//ab pinning.
Zr-doped $(Y,Gd)Ba_2Cu_3O_{7-x}$	SuperPower	Creation of $BaZrO_3$ nanodots aligned along the c-axis direction, producing enhanced H//c pinning.
Nb-doped $YBa_2Cu_3O_{7-x}$	SuperPower	YBa_2NbO_6 nanoparticle alignment in c-axis direction, for enhanced H//c pinning, in addition to increased H//ab pinning from stacking faults generated.

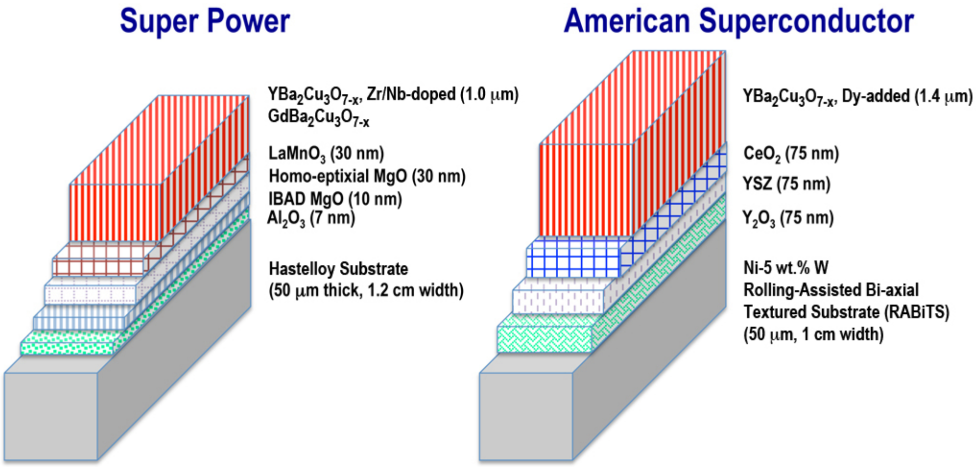

Figure 1. Schematic of the two buffer layer architectures used in this work.

Experimental Procedure

The as purchased long-length Zr-doped (Y,Gd)$Ba_2Cu_3O_{7-x}$ and (Y,Dy)$Ba_2Cu_3O_{7-x}$ conductors showed critical current, I_c, values in self-field of approximately 239 A/cm-width and 525 A/cm-width, respectively, across the 1 meter length tapes received. These tapes have been cut down into smaller test samples and for the case of the Zr-YBCO material, the Ag overlay coating was removed through etching. The purchased $Gd_2Ba_2Cu_3O_{7-x}$ samples were already pre-cut into smaller test specimens. Patterned current bridges were laser scribed into the HTS test samples for electrical characterization tests in order to accommodate on the available measurement equipment these high current-carrying tapes. Silver was deposited at specific sites for the pad positions of the four-probe voltage and current contacts. Following this, the samples were given a thermal anneal in oxygen at 500°C for 1 hour.

Field dependence characterizations of J_c as a function of applied magnetic field strength, and resistance versus temperature measurements were performed at the University of South Alabama. Angular dependence of I_c with field measurements was performed at ORNL. Pre-irradiation characterization of the specific test samples will allow for the precise assessment of each samples response to irradiation without the influence of possible variations occurring along the full-length tapes.

Transmission electron microscopy (TEM) characterization was performed using a Philips/FEI CM200 instrument at ORNL. Samples for TEM analysis were created through focus ion beam (FIB) milling the HTS samples using a FEI Quanta 3D 200i dual beam instrument. Care was taken in minimizing ion beam created damage during processing, with final thinning of the specimen performed down to a 2 kV,8.9 pA, beam conditions using the Ga ion source.

Ion irradiation will be performed at low energy levels typical of simulating cascade damage to avoid columnar defect formation that occurs when the electronic energy loss of the irradiating ions is above 20 keV/nm [21-23]. Computational analysis of energy loss profiles through the HTS tapes was performed using TRIM calculations to evaluate the electronic energy loss, penetration depths and collision events for 10 MeV O, 25 MeV Cu, and 25 MeV Au irradiations. To achieve a significant number of collisions occurring in the 1-1.4 mm thick HTS layer, 25 MeV

Au ion irradiations were selected for this testing. Based on TRIM calculations and estimates from published data [22,24], fluence ranges to be examined for the 25 MeV Au irradiations will be between 10^{10} and 10^{13} ions/cm^2. The first round of Ion irradiation of the HTS conductors will be completed in the first week in January of 2013, at a fluence of 10^{12} ions/cm^2. The fluence selected will be high enough to provide an initial feedback to our estimates, without exceeding conditions where J_c values fall due to excessive damage to the HTS structure.

RESULTS

Pre-irradiation characterization of the superconducting properties and microstructure has been completed for the material obtained to date. The microstructure of the $(Y,Dy)Ba_2Cu_3O_{7-x}$ conductor (Figure 2) is characterized by spherical shaped $(Y,Dy)_2O_3$ particles in the 123 matrix. Energy dispersive X-ray spectroscopy (EDS) analysis determined that Dy is substituting approximately 43% for Y in the 123 matrix and 39.2% for Y in the $(Y,Dy)_2O_3$ nanoparticles. The average $(Y,Dy)_2O_3$ particle size and density are measured at 26 nm and 4.7×10^{21} m^{-3}, respectively. These particles are cubic structured and do not display any specific orientation relationship to the 123 matrix. However, examples are found that show shapes with sides flattened parallel to the (001) planes of the matrix. Present in the 123 matrix are stacking fault defects identified as intergrowths of $(Y,Dy)Ba_2Cu_4O_8$, assuming that Dy is also substituting for Y in these layers. This 124 structure is similar to the 123 structure, but with the addition of a double Cu-O chain (Y-123, has a single Cu-O chain) that creates the longer c-axis lattice constant of 2.723 nm, versus 1.174 nm for Y-123.

The electrical properties of the pre-irradiated $(Y,Dy)Ba_2Cu_3O_{7-x}$ conductor samples were tested at field strengths up to 1.5 Tesla under varying applied angular field directions (f). The results for one of the test specimens is shown in Figure 3, and reveals that there is no enhanced J_c performance in the condition where the applied magnetic field is parallel to the c-axis (B//c, f=90°). This corroborates with microstructural studies that show only planar defects along the ab-planes are observed. The $(Dy,Y)_2O_3$ particles offer improved properties over that of undoped YBCO over a range of applied field directions, but the lack of particle alignment provides no additional benefit to the conductor properties in the B//c field orientation as compared to that of the B//ab.

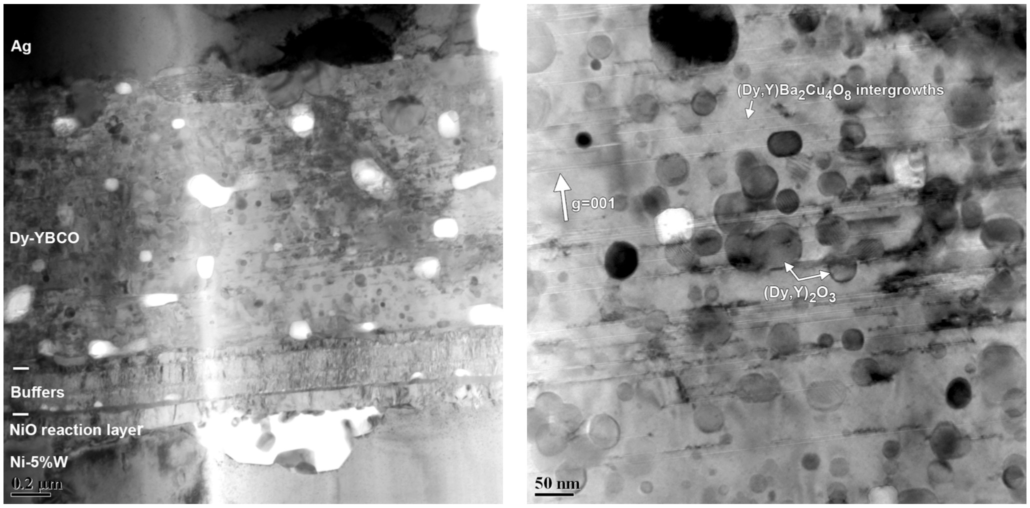

(a) (b)

Figure 2. Transmission electron micrographs of the $(Y,Dy)Ba_2Cu_3O_{7-x}$ material in the as received, pre-irradiated, condition. (a) Low magnification image showing superconducting layer, buffers and bi-axially textured Ni-5%W substrate. (b) Two-beam image, g=001, of the conductor showing the presence of $(Y,Dy)_2O_3$ particles and $(Y,Dy)Ba_2Cu_4O_8$ intergrowths. The Ag layer on the top of the superconducting film was deposited for the current contact pad used in electrical testing.

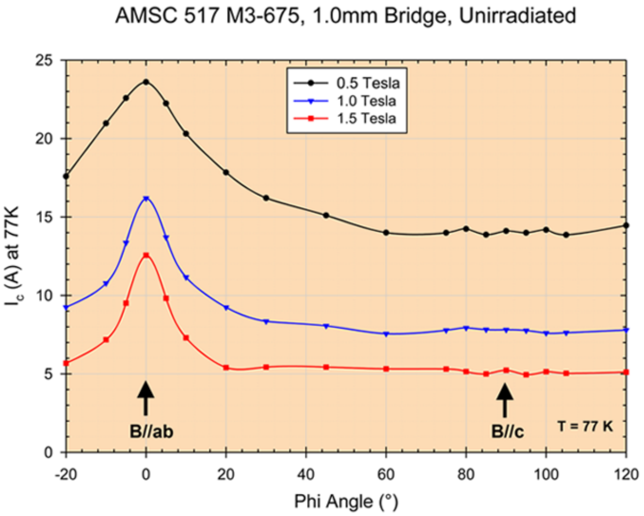

Figure 3. Pre-irradiation critical current versus applied angular field as a function of field strength for $(Y,Dy)Ba_2Cu_3O_{7-x}$, sample AMSC 517, using a 1 mm bridge.

The $GdBa_2Cu_3O_{7-x}$ conductor has a different defect structure than the $(Y,Dy)Ba_2Cu_3O_{7-x}$ conductor. The 123 growth domains create slight mismatches (less than one unit cell) between each other resulting in a threading defect or anti-phase domain running in the c-axis (tape normal) direction (Figure 4a). The high density of $(Y,Dy)_2O_3$ particles in the $(Y,Dy)Ba_2Cu_3O_{7-x}$ conductor remove these anti-phase domains. The anti-phase domain sites can provide some measure of H//c pinning, but are mainly a source for intergrowths into the 123 structures. These intergrowths, a type of stacking fault, are identified as Gd_2BaCuO_4, which are different than those observed in the $(Y,Dy)Ba_2Cu_3O_{7-x}$ conductor. In both cases the intergrowths provide additional H//ab pinning. The amount of intergrowths is greater in the $GdBa_2Cu_3O_{7-x}$ film than the other conductor types examined, as was evident in the observed streaking in the <001> between the diffracted intensities of the [100] zone axis pattern (not shown). The $GdBa_2Cu_3O_{7-x}$ conductor also contains Gd_2O_3 particles (Figure 4b) with an average size of 3.8 nm and density of $1x10^{22}$ m^{-3}. The Gd_2O_3 particles show an occasional disruption in the 123 stacking sequence resulting in faulted structures being generated. The length of the 211 faults created by the Gd_2O_3 particles is on the order of 10 to 20 nm while those originating at the domain boundaries well exceed these values.

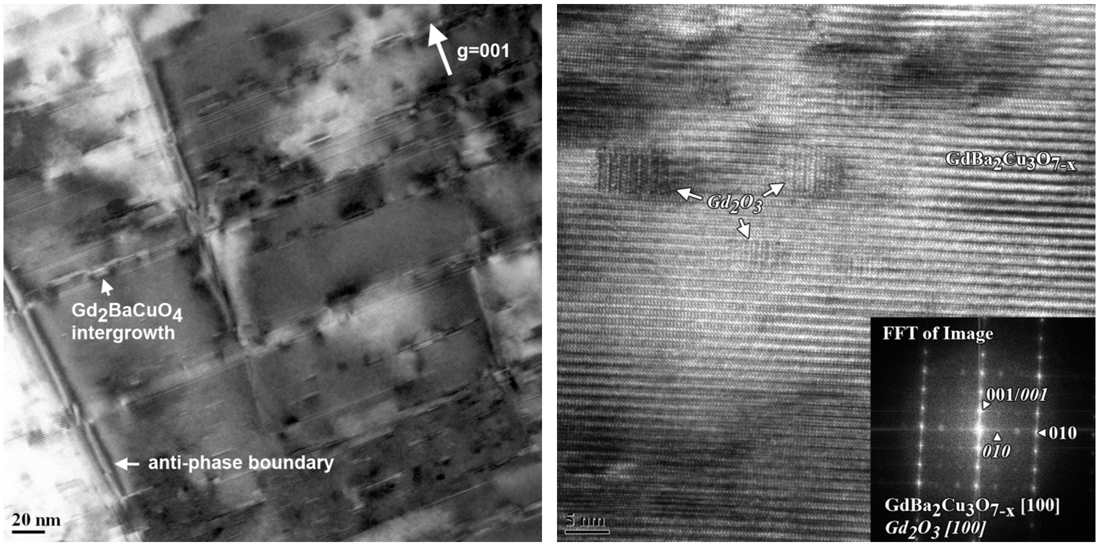

(a) (b)

Figure 4. Transmission electron micrographs of the $GdBa_2Cu_3O_{7-x}$ material in the as-received, pre-irradiated condition. (a) Two beam, g=001, image illustrating the defect structures created in the superconductor resulting in threading anti-phase defect boundaries between different growth domains of the conductor emanating from the buffer interface and Gd_2BaCuO_4 type intergrowths generated from them. (b) High resolution image on the $GdBa_2Cu_3O_{7-x}$[100] zone axis, showing the presence and orientation of Gd_2O_3 particles in the conductor.

The angular field dependence measurement for the pre-irradiated electrical properties of a $GdBa_2Cu_3O_{7-x}$ sample are shown in Figure 5, and similar to that of the $(Y,Dy)Ba_2Cu_3O_{7-x}$ conductor, reveal no enhanced J_c performance in the condition in the B//c condition. This is also not unexpected due to the dominance of the Gd_2BaCuO_4 intergrowths present in the microstructure. While the Gd_2O_3 particles show a strong orientation relationship to the 123 matrix, they are un-oriented in spatial distribution in the conductor. However, the role of the Gd_2O_3 particles appear to increase the amount of intergrowths and may be responsible for the stronger pinning forces appearing in the B//ab condition compared to the $(Y,Dy)Ba_2Cu_3O_{7-x}$ conductor. The positioning of the B//ab peak to f<0° is due to a slight tilt in the orientation of the $(Y,Dy)Ba_2Cu_3O_{7-x}$ conductor relative to the normal of the tape, and is observed in all conductors in this study that were deposited on the SP substrates.

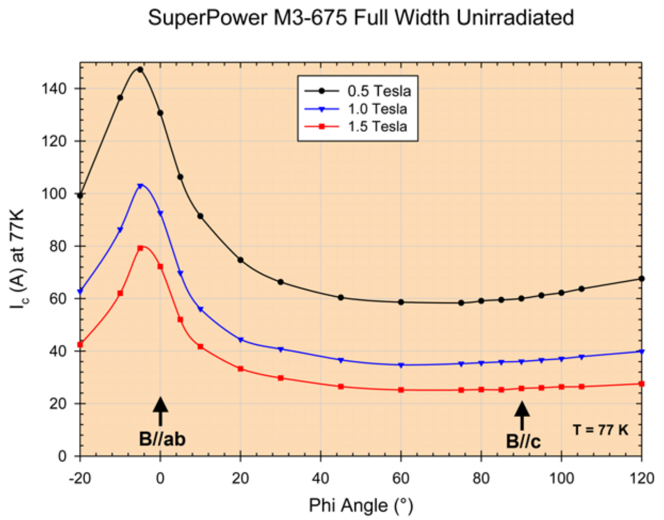

Figure 5. Pre-irradiation critical current versus applied angular field as a function of field strength for $GdBa_2Cu_3O_{7-x}$, sample SPM3-675, full width un-bridged.

The Zr-doping of the $(Y,Gd)Ba_2Cu_3O_{7-x}$ conductor results in a microstructure of $BaZrO_3$ (BZO) particles in the 123 matrix (Figure 6). However, it is apparent that an orientation of the BZO particles deviates at approximately 225 nm above the buffer, from particle alignments along the [100] direction in the 123 matrix to that of the [001]. The cause for this may be related to strain relief during the growth of the film during fabrication, or a change in elemental concentration occurring in the deposition process. Preliminary tilting experiments suggest that there may be a change in orientation relationship between the BZO and 123 structures at the two different levels, but this requires further confirmation through additional high-resolution imaging. The alignment of the BZO particles in the upper portion of the conductor creates a columnar defect structure in the [001] direction that is clearly evident in the g=001 two-beam image. Occasional stacking faults producing an intergrowth of the Y211 type structure are observed, as was also seen in the $GdBa_2Cu_3O_{7-x}$ film. High-resolution images were taken of the BZO particles from the lower (Figure 6c) and upper (Figure 6d) regions of the film. Unfortunately, the TEM foil was thicker than the size of the typical particles and therefore a clear lattice image of the BZO particles could not be easily obtained. One particle near the lower portion of the conducting film was thick enough to perform analysis on, and shows the particle displaying a $[010]_{YBCO}$//

$[100]_{BZO}$, $(001)_{YBCO}//(100)_{BZO}$ orientation relationship. For smaller particle sizes, as those observed in the upper portion of the film, a Moiré fringe pattern is imaged due to the overlapping of the matrix and BZO lattice images.

The amount of Gd substitution in the matrix is approximately 55% based on EDS analysis. While the size of the BZO particles made it difficult to eliminate contributions from the matrix in EDS measurements. A comparison of the ratio between the Gd_M and Cu_K characteristic X-ray intensities was made between spectra taken from BZO and matrix locations. If Gd does not substitute for Zr in the BZO structure, then the Gd_M/Cu_K ratio will remain the same as that of the matrix. However, a 20% average increase in the Gd_M/Cu_{Ka} ratio was observed for the BZO spectra over that of the 123 matrixes, suggesting the presence of Gd in the BZO structure. Further thinning of the TEM foil is required to confirm this data and to perform more conclusive high-resolution imaging of the BZO particles.

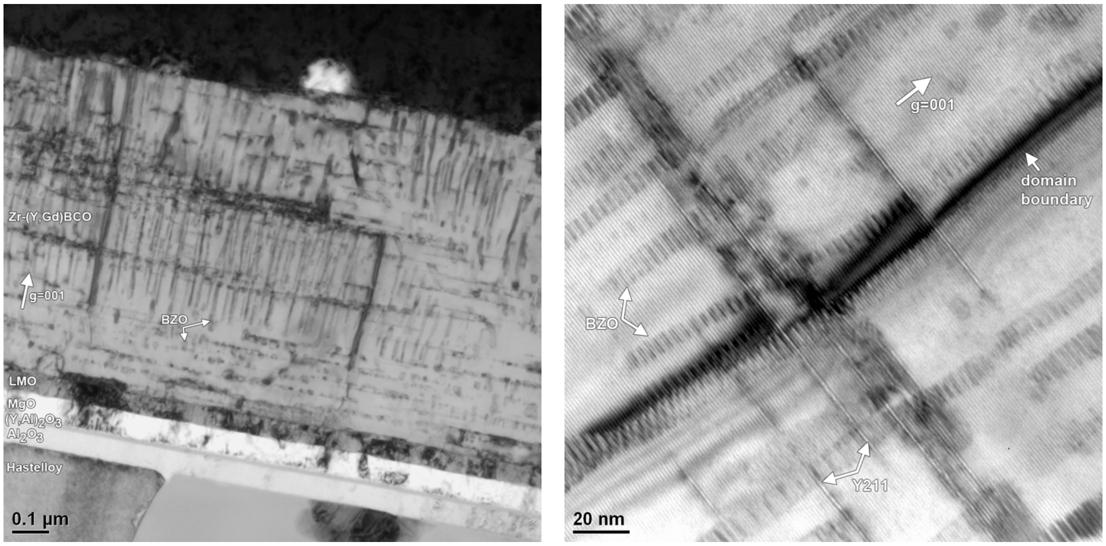

(a) (b)

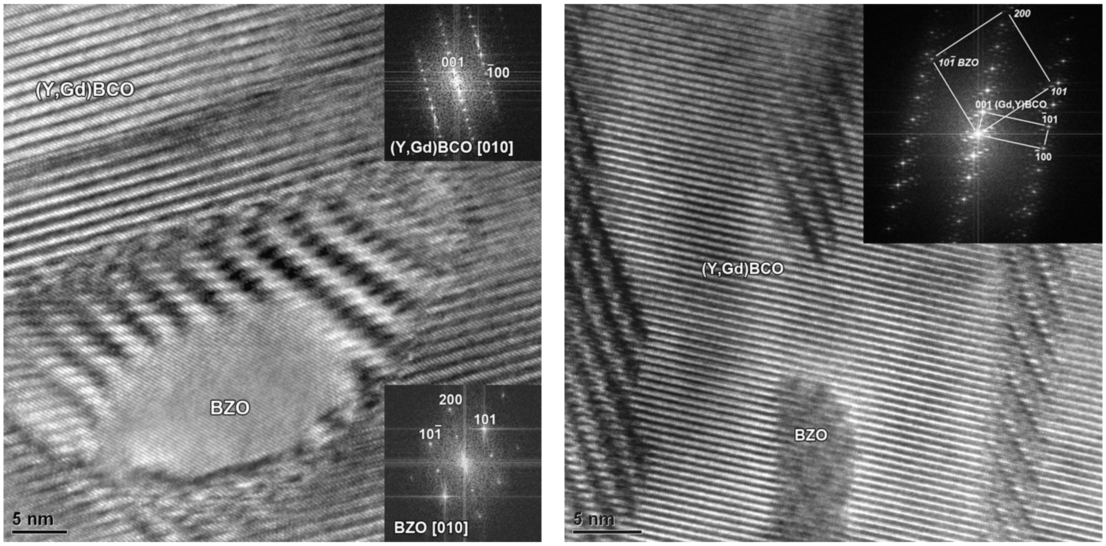

(c) (d)

Figure 6. Transmission electron micrographs of the Zr-doped $(Y,Gd)Ba_2Cu_3O_{7-x}$ material in the as-received, pre-irradiated, condition. (a) Two-beam, g=001 image, illustrating domain boundaries and $BaZrO_3$ (BZO) particle distribution in the superconducting film layer. (b) Higher magnification image under the g=001 condition showing a domain boundary with BZO particles aligned in the c-axis direction. Stacking faults in the conductor are identified as $(Y,Gd)_2BaCuO_4$ (Y211) type. High-resolution images, $B=[010]_{YBCO}$, of the BZO particles (d) near the buffer and (e) at the top of the film. The TEM foil is thicker than most particles, resulting in the Moiré fringe pattern where particles are located.

Due to the alignment of the BZO particles along the c-axis direction (normal to the tape surface), the Zr-doped $(Y,Gd)Ba_2Cu_3O_{7-x}$ material showed a strong increase in pinning in the B//c direction. A comparison of the angular field dependency of the three HTS materials investigated is shown in Figure 7a. The effect of the BZO particles provides near equal I_c measurement in the B//c direction as measured in the B//ab condition dominated by the Y211 intergrowths. It should be cautioned that while the angular field dependency curves for the three HTS materials illustrate the effect of the nanoparticle alignments, comparison between the three samples is not possible due to differences in batches and measurement conditions. However, it is clear that the field dependence of the HTS materials is reduced by the effect of the aligned BZO particles (Figure 7b).

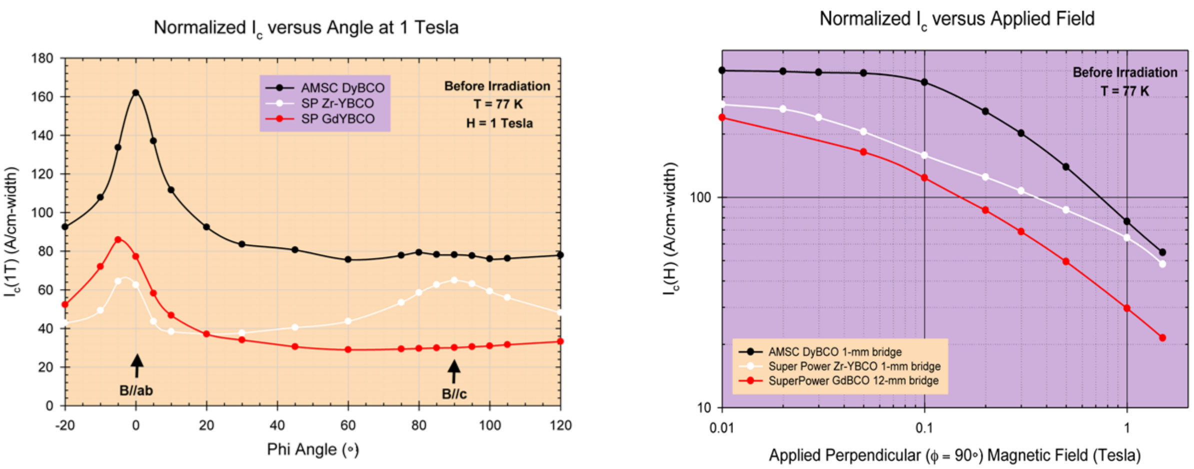

(a) (b)

Figure 7. (a) Comparison of the pre-irradiation critical current versus applied angular field as a function of field strength for the (Y,Dy)$Ba_2Cu_3O_{7-x}$, $GdBa_2Cu_3O_{7-x}$, and Zr-doped (Y,Gd)$Ba_2Cu_3O_{7-x}$ samples. (b) Normalized Ic values versus applied field measured under the B//c condition for the various HTS materials examined. Due to difference in sample batches, direct comparisons between sample types is not possible, but general trends in behavior can be observed.

FUTURE WORK

The first round of ion irradiation exposure, 25 MeV Au at 10^{12} ions/cm^2, and post-irradiation testing will begin shortly. Care was taken in measuring the pre-irradiation electrical properties of each HTS sample in order to asses the effects of irradiation damage on their properties and to avoid any variations that may appear in sample to sample batches. This work will provide a first investigation into the radiation effects on the most advanced HTS materials. The effects on superconducting properties through the changes to pre-existing flux pinning centers and the development of radiation-induced defects will be examined through both electrical and microstructural characterization. This work will expand later into low temperature irradiation testing of specific materials that will include *in situ* measurement of self-field superconducting properties as a function of dose, with a further analysis into defect annihilation and the effects of temperature excursions on conductor properties.

REFERENCE

1. H. W. Weber, *Physica C* **185-189** (1991) 309.
2. P. X. Zhang, et al., *Physica C* **282-287** (1997) 1607.
3. F. Vasiliu, V. Sandu, P. Nita, S. Popa, E. Cimpoiasu, and M. C. Bunescu, *Physica C* **303** (1998) 209.
4. D. V. Kulikov, Y. V. Trushin, F. M. Sauerzopf, M. Zehetmayer and H. W. Weber, *Physica C* **355** (2001) 245.
5. U. Topal, H. Sozeri, and H. Yavuz, *Physica C* **408-410** (2004) 636.
6. U. Topal, L. Dorosinskii and H. Sozeri, Physica C **407** (2004) 49.
7. S. Shojaei, R. Khoda-Bakhsh and H. Sedgi, and *J. Supercond. Nov. Magn.* **24** (2008) 387.
8. R. Fuger, M. Esterer, and H. W. Weber, *IEEE Trans. Appl. Supercond.* **19**, 3 (2009) 1532.

9. M. Chudy, R. Fuger, M. Eisterer and H. W. Weber, *IEEE Trans. Appl. Supercond*. **21**, 3 (2011) 3162.
10. T. Nishimura, S. Takeuchi, G. Nishijima, T. Shikama, K. Ochiai, and N. Koizumi, *Fusion Eng. Design* **84** (2009) 1425.
11. D. Larbalestier, A. Gurevich, D. M. Feldmann and A. Polyanski, *Nature* **414** (2001) 368.
12. R. M. Scanlan, A. P. Malozemoff and D. C. Larbalestier, *Proc. IEEE* **92**, 10 (2004) 1639.
13. A. Goyal, et al., *Supercond. Sci. Technol.* **18** (2005) 1533.
14. B. Maiorov, et al., *Nature Mater.* **8**, 5 (2009) 398.
15. S. H. Wee, et al., *Supercond. Sci. Technol*. **21**, 9 (2008) 92001.
16. P. Paturi, et al., *J. Appl. Phys*. **103**, 12 (2008) 123907.
17. S. Kang, et al., *Physica C* **457**, 1-2 (2007) 41.
18. K. Gutierrez, et al., *Nature Mater*. **6**, 5 (2007) 367.
19. D. C. van der Laan, X. F. Lu and L. F. Goodrich, *Supercond. Sci. Technol.* **24** (2011) 042001.
20. D. C. van der Laan, *Supercond. Sci. Technol*. **22** (2009) 065013.
21. N. M. Stickland, N. J. Long, J. Xia, J. Kennedy, A. Markwitz, A. Zondervan, M. W. Rupich, W. Zhang, X. Li, T. Kodenkandath and Y. Huang, *IEEE Trans. Appl. Supercond.* **17**, 2 (2007) 3306.
22. B. Hensel, B. Roas, S. Henke, R. Hopfengärtner, M. Lippert, J. P. Ströbel, M. Vildić and G. Saemann-Ischenko, *Phys. Rev. B* **42**, 7 (1990) 4135.
23. R. Wheeler, M. A. Kirk, A. D. Marwick, L. Civale, and F. H. Holtzberg, *Appl. Phys. Lett*. **63**, 11 (1993) 1573.
24. J. R. Liu, J. Kulik, Y. J. Zhao and W. K. Chu, *Nucl. Instr. Meth. Phys. Res. B* ***80-81*** (1993) 1255.

5.2. High Neutron Dose Irradiations of Dielectric Mirrors

— K. J. Leonard, G. E. Jellison, Jr., L. L. Snead (Oak Ridge National Laboratory), and A. P. K. K. Nimishakavi (University of Tennessee)

OBJECTIVE

The goal of this work is to evaluate the upper neutron irradiation dose and thermal limits of two promising dielectric mirror types, through an investigation of the radiation and thermally induced microstructural and optical property changes. While specifically of interest for use in laser control of inertial confinement fusion systems, the examination of the radiation induced structural changes in the films will be beneficial for the development of other thin-film based electronic components and sensors used in nuclear applications.

SUMMARY

Our experimental work to date on HfO_2/SiO_2 and Al_2O_3/SiO_2 dielectric mirrors indicate an impressive irradiation resistance. However, with increasing dose, chemistry and crystallinity changes in the film layers of the mirrors result in decreases in reflectivity of the HfO_2/SiO_2 mirror following post irradiation annealing. This contribution discusses the recent microscopy work on the 0.1 dpa-irradiated mirrors to assess the causes in optical property changes. Further work has been initiated this year for higher irradiation dose experiments to determine the upper neutron irradiation dose and thermal limits of the HfO_2/SiO_2 and Al_2O_3/SiO_2 mirrors. At the time of this writing, irradiation capsules have completed 1×10^{21} and 4×10^{21} n/cm^2 (E>0.1 MeV) exposures at 448 K, corresponding to approximately 1 and 4 displacements per atom (dpa). Post irradiation examination of the high dose mirrors will begin at the start of 2013.

PROGRESS

Introduction

The stability of the film layers in dielectric mirrors under combined thermal and neutron radiation environments were an early concern for applications in beam control and diagnostic systems of inertial confinement fusion energy systems. Improvements in deposition methods, quality of films, refinement of the number of bi-layers and choice of more radiation resistant substrates all provide an increase in radiation stability. Recent work by the authors on HfO_2/SiO_2 and Al_2O_3/SiO_2 mirror types has demonstrated radiation stability to displacement doses to 0.1 dpa [**Error! Reference source not found.**]. However, the upper thermal and radiation limits, as well as the structural changes in mirrors causing degraded optical properties are not well known. This work expands the neutron irradiation examination of two dielectric mirror systems based on alternating Al_2O_3/SiO_2 and HfO_2/SiO_2 films on single crystal sapphire substrates tuned for maximum reflectivity at 248 nm. New data on the 0.1 dpa samples examined this past quarter are discussed in the results section, while details on the irradiation testing to 4 dpa are presented in the experimental procedure section. The irradiation exposures to 4 dpa have just completed their time in the reactor, with post irradiation testing about to begin.

Experimental Procedure

Spectrum Thin Films Inc. manufactured the HfO_2/SiO_2 and Al_2O_3/SiO_2 mirrors tuned for maximum reflectivity at 248 nm examined in this study. The repeating bi-layer films were deposited by electron-beam deposition with ion-assist on alpha-Al_2O_3 (sapphire) substrates. Substrate size was 6 mm diameter by 2 mm thick. In addition to the mirrors, monolayer films of Al_2O_3, SiO_2 and HfO_2 were also deposited on the substrates and included in the same exposure testing as the mirrors. Film layer thicknesses were 26, 32 and 40 nm for the HfO_2, Al_2O_3 and SiO_2 layers, respectively. To achieve peak reflectivity at 248 nm, the HfO_2/SiO_2 mirror consisted of 11 bi-layers of the 1/4l films and 30 bi-layers for the Al_2O_3/SiO_2 mirror.

Previous work on these samples have involved the neutron irradiation of the mirrors and monolayer samples to 0.001, 0.01 and 0.1 dpa at 448 K. The current work involves the irradiation of a second set of samples to higher doses followed by similar post irradiation examination (PIE) of the optical and microstructural changes to the mirrors. Irradiations to $1x10^{21}$ and $4x10^{21}$ n/cm^2 (E>0.1 MeV) at 448 K, corresponding to approximately 1 and 4 displacements per atom (dpa), were completed in the peripheral hydraulic tube at the High Flux Isotope Reactor (HFIR) on November 3, 2012. The samples are encapsulated in specialized 1100 grade Al holders to eliminate damage to the mirror surfaces, while targeting the appropriate irradiation temperature. The sample holders will be unloaded at the LAMDA lab to ensure proper handling of the mirrors, this is to begin at the start of 2013.

Testing of the 1 and 4 dpa samples will include 1 hour post-irradiation thermal anneals of the mirrors with peak thermal annealing temperatures of 573 K for the HfO_2/SiO_2 mirror and at 673 K for the Al_2O_3/SiO_2 mirror to be considered based on earlier research work. Annealing studies of the unirradiated controls have already been performed.

Optical examination of the samples will include changes in the relative spectral reflectance versus wavelength and the absolute reflectivity at 248 nm for the irradiated and post-irradiated annealed specimens. The optical changes will be correlated to microstructural changes in the films examined through transmission electron microscopy (TEM). Ellipsometry will be performed on the irradiated HfO_2 and Al_2O_3 monolayer films deposited on the sapphire substrates for select conditions and compared to the unirradiated controls in order to elucidate strain effects at the film/substrate interface.

RESULTS

It was found in earlier work that irradiation to 0.1 dpa showed no change in absolute reflectivity of either the HfO_2/SiO_2 or Al_2O_3/SiO_2 mirrors and that no further decrease in optical properties of the Al_2O_3/SiO_2 mirrors was found after 1 hour annealing in vacuum up to 673 K. Examples of the reflectivity versus wavelength normalized to the measured absolute reflectivity are presented in Figure 1. The changes in the working range, the peak reflectivity range in the wavelength spectrum, with irradiation and thermal annealing is the result of changes in film thickness layers of the mirrors. The change in working range for the Al_2O_3/SiO_2 mirror is small and correlates to the nearly insignificant change in average film thickness (Figure 2a) for the different exposure conditions. The measured data range for the Al_2O_3/SiO_2 mirror layer thicknesses for the different exposure conditions are within the statistical measurement of error to that of the control. This was not the case for the HfO_2/SiO_2 mirror, as the changes in working range were greater as was the measured decrease in SiO_2 layer thickness (Figure 2b) in both the irradiated and thermal annealing conditions. The cause for the difference in behavior of the SiO_2 layers in the two mirrors may be related to both compaction of the SiO2 layer, but to the overall changes occurring in the other film layers in the mirrors. With increasing irradiation dose and thermal annealing temperature, the amount of interdiffusion between the Al_2O_3 and SiO_2 layers increases (Figure 3a). However, despite the measureable amount of composition change, no significant change in film thickness occurs and no interlayer appears in the Al_2O_3/SiO_2 mirrors (Figure 4). The stability of the Al_2O_3/SiO_2 mirror to irradiation and thermal heat treatment arises from the amorphous structure of the constituent layers that are more accepting of damage. Furthermore, the amorphous structure may be more accommodating to the Si/Al interdiffusion, which may also provide an added level of stability to the mirror. Increased stability to laser damage initiation threshold (LDIT) was reported in amorphous TiO_2/SiO_2 mirrors that incorporate 17% SiO_2 into the TiO_2 layer [1]. The modified mirrors showed an increase in thermal stability of the films with no degradation in LDIT measured at annealing temperatures 75% higher than that limiting the unmodified mirrors, which indicated signs of crystallization of the TiO_2 layer.

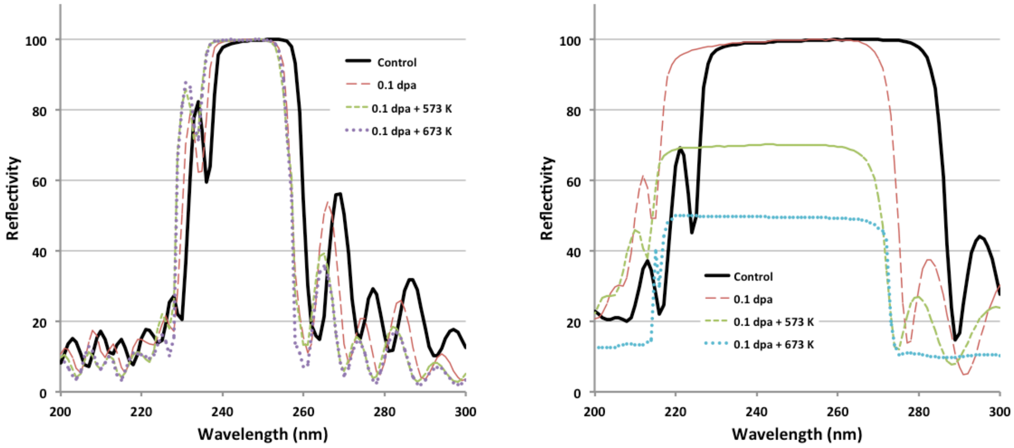

(a) (b)

Figure 1. Changes in the working range of the mirrors measured through specular reflectance normalized to the absolute reflectivity measured by excimer laser measurements at 248 nm. (a) The Al_2O_3/SiO_2 mirrors showing stability up to 0.1 dpa and in post irradiation thermal treatments to 673 K. (b) The HfO_2/SiO_2 mirror showing loss of reflectivity with post irradiation annealing of the 0.1 dpa irradiated samples.

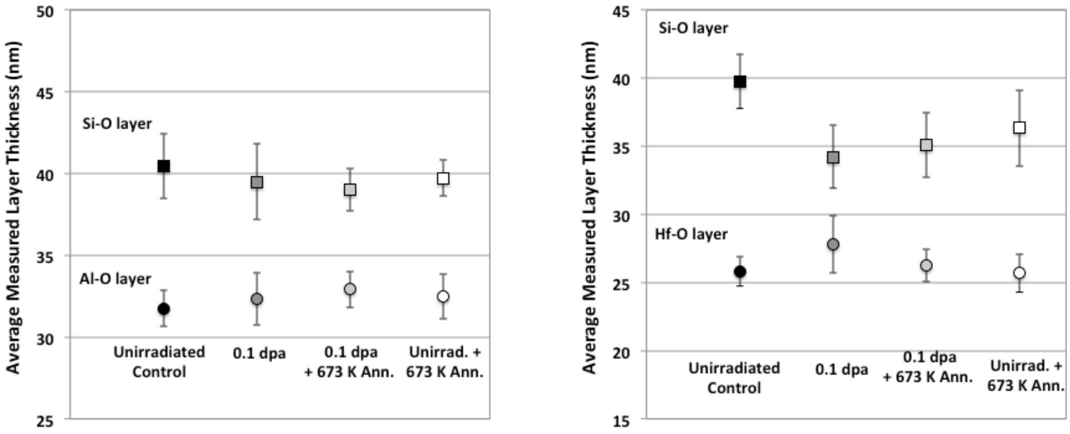

(a) (b)

Figure 2. The average measured thickness of constituent film layers in the (a) Al_2O_3/SiO_2 and (b) HfO_2/SiO_2 mirrors. Error bars represent the standard deviation in the data with each data point representing over 30 measurements of at least 5 different film layers, with the exclusion of the base layer at the sapphire substrate that is intentionally thicker than the subsequent layers.

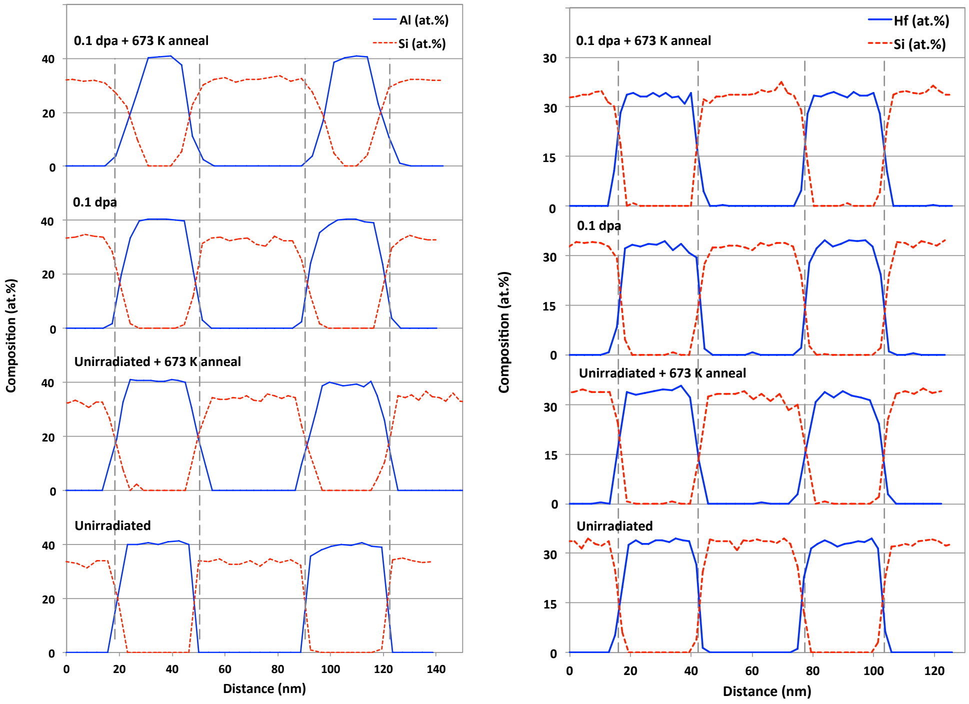

(a) (b)

Figure 3. The calculated compositions of the constituent layers measured through energy dispersive spectroscopy of the (a) Al_2O_3/SiO_2 and (b) HfO_2/SiO_2 mirrors. Showing the interdiffusion between the Al/Si bearing layers with increasing irradiation dose and thermal annealing for the Al_2O_3/SiO_2 mirror and the lack of interdiffusion in the HfO_2/SiO_2 mirrors.

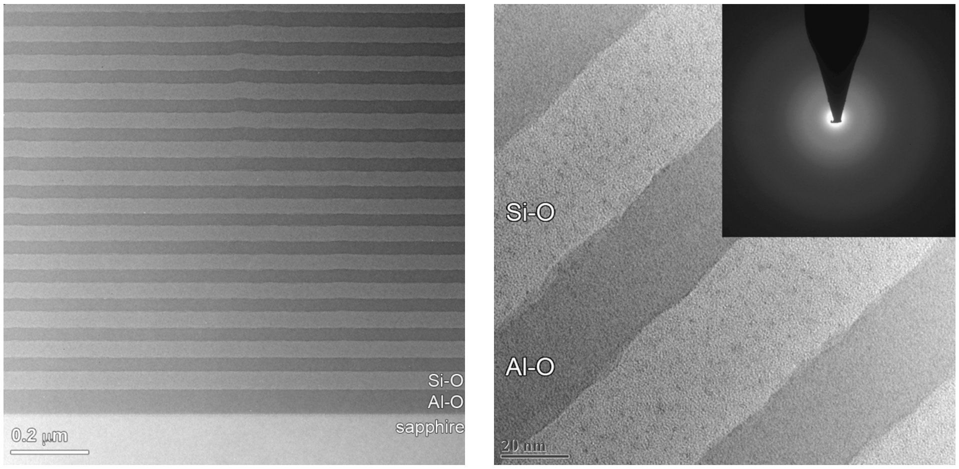

(a) (b)

Figure 4. TEM micrographs of the Al_2O_3/SiO_2 mirror irradiated to 0.1 dpa and annealed 1 hour at 673 K. (a) Low magnification image showing relatively smooth layers with limited perturbations that create repeating deviations in subsequently deposited layers. (b) Higher magnification image taken in a defocused condition showing some black spot defects in the amorphous layers and no interphase formations. Disturbances at the film interfaces are due to localized film roughness, the thickness of the sample at that location and the defocused conditions used.

Decreases in reflectivity of the HfO_2/SiO_2 mirror irradiated to 0.1 dpa with increasing annealing temperature (Figure 1b) was observed and attributed to changes in the crystallinity of the HfO_2 layer and the corresponding changes state of strain at the HfO_2 / sapphire interface. The 0.1 dpa irradiated HfO_2/SiO_2 mirror showed the largest shift in working range toward lower wavelengths, the result of substantial decrease in SiO_2 layer thickness (Figure 2b). This was also the case for the 673 K annealed control where a reduction in the SiO_2 layer was measured. As no significant interdiffusion of Hf and Si were measured between the constituent layers in the examined mirrors, Figure 3b, densification of SiO_2 is suspected.

Changes in the crystalline structure of the HfO_2 layer in the HfO_2/SiO_2 mirrors were observed through electron and X-ray diffraction following irradiation and subsequent annealing treatments. The as-deposited mirrors displayed polycrystalline monoclinic structured grains in the HfO_2 layers with an average grain size of 13 nm (Figure 5). However, the as-deposited HfO_2 layers showed some amorphous structuring around the crystalline grains when viewed under high-resolution imaging. The amorphous regions disappeared on irradiation to 0.1 dpa or with thermal aging of the unirradiated control material. With irradiation to 0.1 dpa, cubic or tetragonal HfO_2 reflections appear in electron and X-ray diffraction patterns (reflected peaks are too few to positively distinguish which of the two polymorphs are present), but fade away with subsequent annealing. The appearance of cubic structured grains in irradiated HfO_2 films have been observed in ion-irradiated films in both the electronic as well as nuclear stopping dominating conditions [3,4].

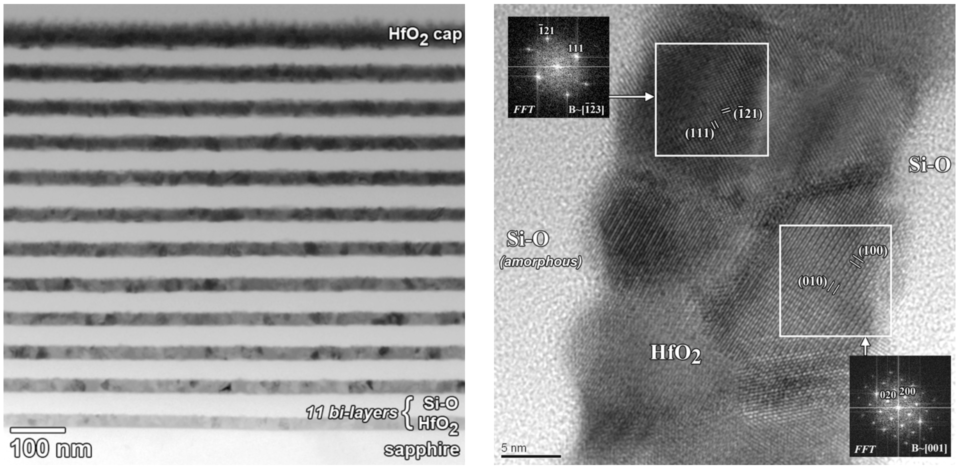

(a) (b)

Figure 5. Low (a) and (b) high magnification TEM micrographs of the unirradiated HfO_2/SiO_2 mirror, showing the polycrystalline grain structure of the HfO_2 and amorphous SiO_2 layers.

The loss in reflectivity with annealing was only observed in samples irradiated to 0.1 dpa and not observed in the unirradiated plus annealed material. The loss in reflectivity was linked to a delamination of the first HfO_2 layer at the sapphire substrate as observed in TEM examinations (Figure 6). The amount of delamination is approximately equal to the percent loss associated with the reflectivity. The precise cause for the delamination is difficult to identify, as no secondary phase or defects were observed at or near the delamination locations in either the HfO_2 layer or in the substrate. The cause is believed to be an effect of strain conditions at the interface, but the reason for appearing in the 0.1 dpa + annealed samples and not in the unirradiated control is not clear. Though an increase in average grain size to 16 nm was measured for the 0.1 dpa-irradiated sample (no further increase measured on annealing to 673 K), a similar grain size was measured for the 673 K annealed unirradiated control. However, the grain structure of the irradiated sample showed a more columnar grain structure that has more grains spanning the thickness of the film layer (compare Figure 5b and Figure 6b). However, there does not appear to be any common alignment of the grains to a particular direction, which could possible increase the strain condition on the adjacent substrate interface. Electron diffraction images taken of the polycrystalline HfO_2 layers in the 0.1 dpa + 673 K annealed and unirradiated plus annealed conditions shows well defined intensities with no diffuse amorphous or non-monoclinic intensities appearing and are indistinguishable from each other. The high-resolution images taken of the HfO_2/sapphire interface are being reviewed further to identify any changes in the orientation of the HfO_2 grains in the first layer with irradiation as compared to the control samples. A further analysis of the strain state between the HfO_2 layer and substrate through ellipsometry of the monolayer films irradiated at the same time are considered for the next stage of work. The monolayer films will allow for cleaner analysis of the ellipsometry data than the multi-layer mirrors.

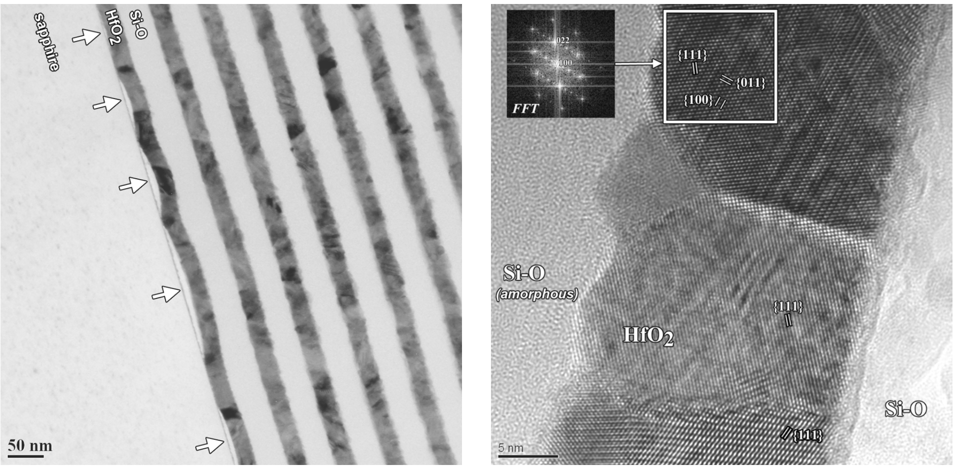

(a) (b)

Figure 6. TEM micrographs of the 0.1 dpa HfO_2/SiO_2 mirror post irradiation annealed 1 hour at 673 K. (a) Delamination of the HfO2 at the interface of the sapphire substrate (indicated by arrows). (b) High magnification image showing the polycrystalline grain structure of the HfO_2 and amorphous SiO_2 layers.

FUTURE WORK

The mirror and monolayer samples irradiated to 1 and 4 dpa have completed their exposures at HFIR and will undergo capsule disassembly at the start of 2013. The samples on unloading will be examined for any crazing, cracks or delamination through visual inspection. The mirrors will then undergo spectrometry analysis of the specular reflectivity followed by absolute reflectivity measurements performed using a 248 nm wavelength excimer laser. Examination of ellipsometry data for the higher dose irradiated monolayer films of HfO_2 and Al_2O_3 in comparison to unirradiated control material will be used to elucidate strain effects at the substrate film interfaces. Following optical testing, TEM examination of select specimens will be performed to determine structural changes in the films causing the observed optical changes.

REFERENCES

1. L. L. Snead, K. J. Leonard, G. E. Jellison Jr., M. Sawan and T. Lehecka, *Fusion Sci. Technol.* **56**, 2 (2009) 1069.
2. S. Chao *et al., Appl. Opt.* **40**, 13 (2001) 2177.
3. I. O. Usov, J. A. Valdez, J. Won, M. Hawley, D. J. Devlin, R. M. Dickerson, B. P. Uberuaga, Y. Q. Wang, C. J. Olson, G. D. Jarvinen, and K. E. Sickafus, *Nucl. Instr. Meth. Phys. Res. B* **267** (2009) 1918.
4. A. Benyagoub, *Nucl. Instr. Meth. B* **218** (2004) 451.

6.2 Compatibility of Materials Exposed to Isothermal Pb-Li — B. A. Pint, K. A. Unocic and S. J. Pawel (Oak Ridge National Laboratory)

OBJECTIVE

One proposed U.S. test blanket module (TBM) for ITER uses ferritic-martensitic alloys with both eutectic Pb-Li and He coolants at ~475°C. In order for this blanket concept to operate at higher metal temperatures (up to 700°C) for a DEMO-type reactor, several Pb-Li compatibility issues need to be addressed. Some of the issues currently being investigated are the compatibility of dispersion strengthened Fe-Cr alloys compared to conventional wrought material, the performance of Al-rich coatings to inhibit corrosion and dissimilar material interaction between SiC and ferritic steel. Planning is under way to transition the compatibility testing from isothermal capsules to thermal convection loops.

SUMMARY

Isothermal capsule experiments were completed on coated and uncoated Grade 92 (9Cr-2W) specimens for 5,000 h in Pb-Li to determine the long-term stability of the coating at 600° and 700°C. Thin ~50μm Al-rich diffusion coatings showed similar low mass changes at both temperatures. However, extensive Al loss was observed after 5,000h at 700°C. In contrast, a thicker diffusion coating where intermetallic aluminide phases formed showed a mass loss after 5,000h at 700°C due to partial spallation of the aluminide coating outer layer. Characterization of the 5,000h specimens is still in progress. These results indicate that (1) Al-rich coatings greatly reduce dissolution at 700°C in Pb-Li but do not prevent it and (2) the effectiveness of coating strategies to improve compatibility are limited. In order to further evaluate the coating concept and wrought and oxide dispersion strengthened (ODS) FeCrAl alloys, plans are being made to build a Pb-Li thermal convection loop of Fe-9Cr or FeCrAl tubing.

PROGRESS AND STATUS

Introduction

A current focus of the U.S. fusion materials program is to address issues associated with the dual coolant Pb-Li (DCLL) blanket concept[1] for a test blanket module (TBM) for ITER and enhanced concepts for a DEMO-type fusion reactor. A DCLL blanket has both He and eutectic Pb-17 at.%Li coolants and uses reduced activation ferritic-martensitic (FM) steel as the structural material with a SiC/SiC composite flow channel insert (FCI). Thus, recent U.S. compatibility research has examined issues with Pb-Li.[2-9] Compared to Li,[10] a wider range of materials can be compatible with Pb-Li because of the low activity of Li.[11] In particular, SiC readily dissolves in Li, but not Pb-17Li.[2,4,12] However, like Pb, Pb-Li dissolves Fe, Cr and especially Ni from many conventional alloys above 500°C.[13,14] This is not a concern for a DCLL TBM operating at <500°C. However, a DCLL blanket for a commercial DEMO-type reactor would be more attractive with a higher maximum operating temperature, perhaps >600°C if ODS ferritic steels[15-18] were used. Even at 550°C, a recent study of Eurofer 97 (Fe-Cr-W) showed a very high dissolution rate in flowing Pb-Li.[14] Therefore, preliminary Pb-Li compatibility capsule experiments are being conducted at 500°-800°C in order to investigate several concepts before flowing Pb-Li compatibility tests are conducted. The final coating capsule tests have been completed with 5,000h exposures at 600° and 700°C and the initial characterization of those specimens is reported. The next phase of this compatibility evaluation is to build a thermal convection loop where both Al-rich coatings and FeCrAl alloys can be evaluated at 550°C and higher Pb-Li temperatures.

Experimental Procedure

Static capsule tests were performed using Mo inner capsules and type 304 stainless steel (SS) outer capsules to protect the inner capsule from oxidation. The uncoated specimens were ~1.5 mm thick and 4-5 cm^2 in surface area with a 600 grit surface finish and were held with 1 mm diameter Mo wire. (Mo can be considered to be essentially inert under these conditions.) For coated specimens, the coupons were polished to a 0.3 μm alumina finish and cleaned ultrasonically in acetone and alcohol. Aluminizing was performed in a laboratory-scale chemical vapor deposition (CVD) reactor consisting of an inductively heated alumina tube with flowing H_2 carrying the $AlCl_x$ vapor. The reactor has been described in detail elsewhere.[19] The thinner coatings were deposited during 6h at 900°C and the thicker coating was deposited under the same conditions but with Al/Cr powder in the reactor to increase the Al activity.[6,19,20] The capsules were loaded with 125g of Pb-Li in an Ar-filled glove box. The Pb-Li was melted and cast at ORNL and had Li contents of 15.6-16.5 at%. The Mo and SS capsules were welded shut to prevent the uptake of impurities during the isothermal exposure. After exposure, residual Pb-Li on the specimen surface was removed by soaking in a 1:1:1 mixture of acetic acid, hydrogen peroxide and ethanol for up to 72 h. Mass change was measured with a Mettler-Toledo balance with an accuracy of 0.01 mg/cm^2. Post-test specimen surfaces were examined using x-ray diffraction (XRD) and secondary electron microscopy (SEM) equipped with energy dispersive x-ray (EDX) analysis. After surface characterization, the specimens were metallographically sectioned and polished and examined by light microscopy and electron microprobe analysis (EPMA) equipped with wavelength dispersive x-ray analysis.

Results and Discussion

Figure 1 shows the mass change for the coated and uncoated Gr.92 specimens reported previously with the most recent results after 5,000h isothermal exposures at 600° and 700°C. The specimens with a ~50μm CVD coating showed low mass changes at both temperatures after 5,000h. The uncoated specimens at both temperatures showed a reduced rate of mass loss compared to the previous 1,000h exposures. This may be due to Pb-Li becoming saturated with the dissolving Fe and Cr at longer times. The rate of dissolution in a capsule test should drop as the liquid becomes saturated, reaching zero at

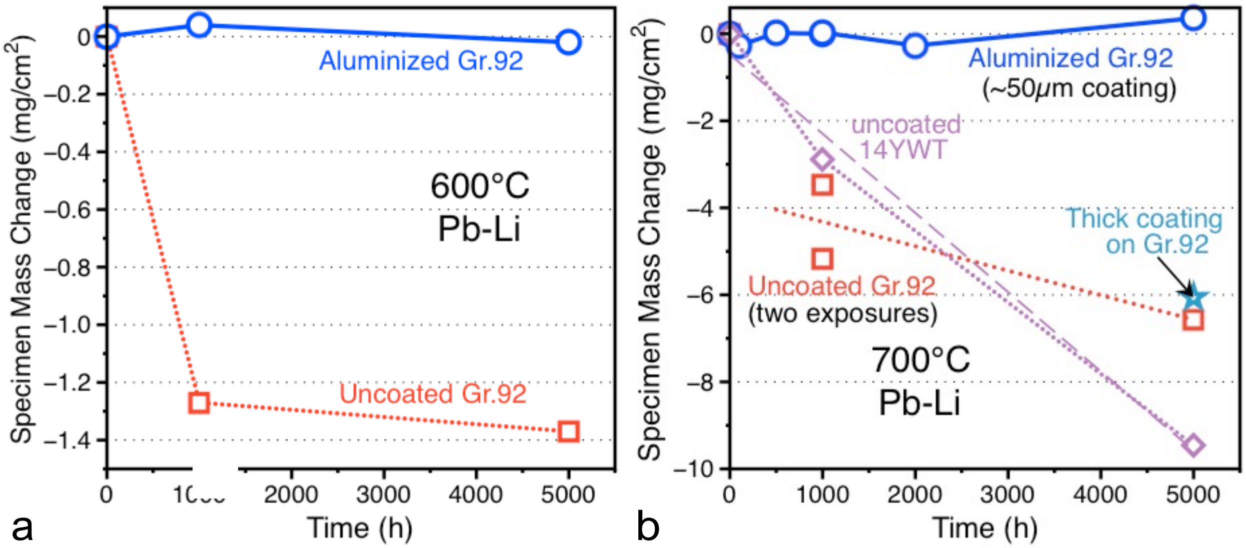

Figure 1. Specimen mass change as a function of exposure time in Pb-Li at (a) 600°C and (b) 700°C.

saturation (which is temperature dependent). This is a primary limitation of an isothermal capsule experiment and loop testing with a thermal gradient is needed to verify the Pb-Li compatibility.

Figure 2 shows polished cross-sections of the specimens exposed for 5,000h at 600° and 700°C with and without a ~50μm CVD coating. The uncoated specimens have a non-uniform surface and the roughness increased with exposure temperature. What appears to be oxide at the surface may be remnants from the cleaning process or partially due to poor adhesion of the Cu-plating. The coated specimens show a typical coating microstructure.[5,21] Especially at the coating-substrate interface, acicular AlN precipitates form due to reaction between Al in the coating and N (0.06 wt.%, 0.23 at.%) in the steel. The concentration of AlN particles marks the original coating-substrate interface in Figure 2d and, to a lesser extent, for the lower temperature exposure in Figure 2b. At both temperatures, a thin surface oxide is present which was identified as $LiAlO_2$ by XRD. In some cases, there are areas where the oxide appeared to be spalled, which may have occurred during cleaning but also could reflect poor adhesion of this oxide layer. For the coated specimen exposure at 700°C, this specimen is the fifth in a time series of specimens.[7] Figure 3 shows Al profiles from this specimen compared to the nominal as-coated composition (shaded area) and the shorter exposures at 700°C. It is obvious that the Al content continues to drop in the coating with increasing exposure time. It is also evident that the Al loss (area under the shaded curve) cannot be explained by back diffusion into the Grade 92 substrate or the small quantity of AlN precipitates. It appears that Al is slowly being lost into the Pb-Li suggesting that the $LiAlO_2$ surface layer is not a perfect barrier to dissolution. More likely the rate limiting dissolution step is now Al being lost from the $LiAlO_2$ layer and being replaced by Al from the substrate. A longer exposure would likely expend the Al reservoir in the coating.

A thicker coating (i.e. larger Al reservoir) was applied to one Grade 92 specimen. Surprisingly, this specimen showed a mass loss of -6.1 mg/cm^2 after 5,000h at 700°C, Figure 1b, a similar mass loss as the uncoated specimen. The reason for the mass loss appears to be coating spallation. For higher Al

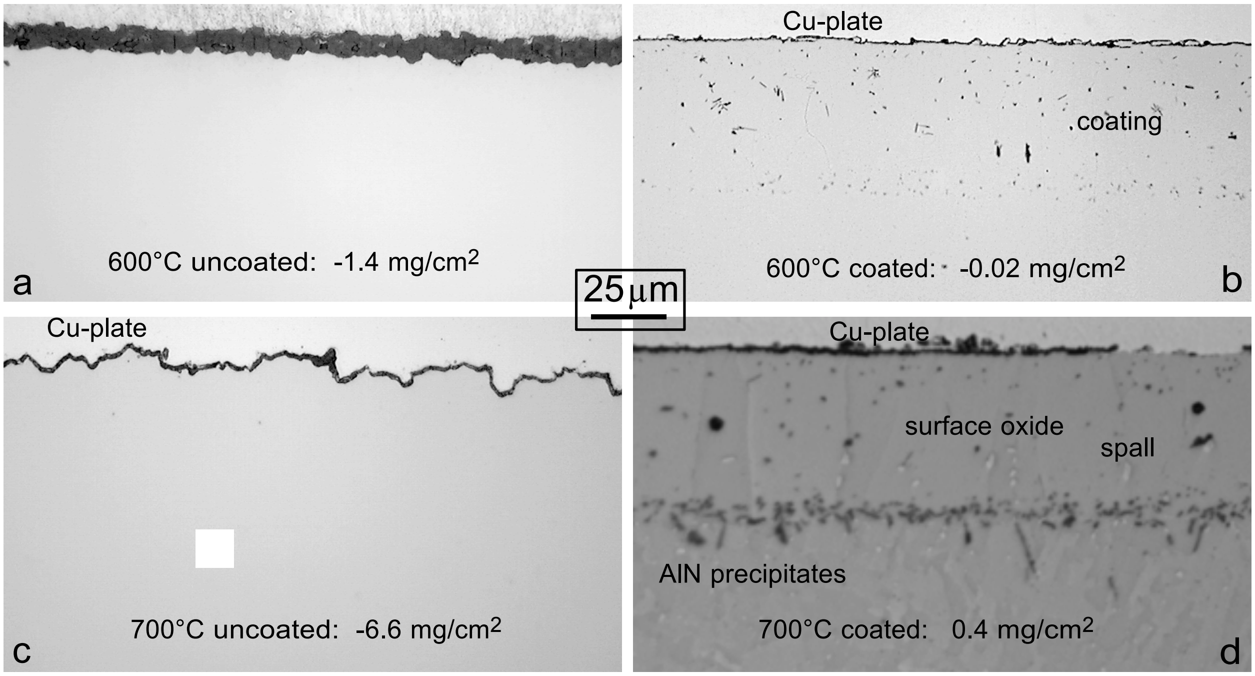

Figure 2. Light microscopy of Grade 92 specimens exposed to Pb-Li for 5,000h (a) uncoated 600°C, (b) coated 600°C (c) uncoated 700°C and (d) coated 700°C.

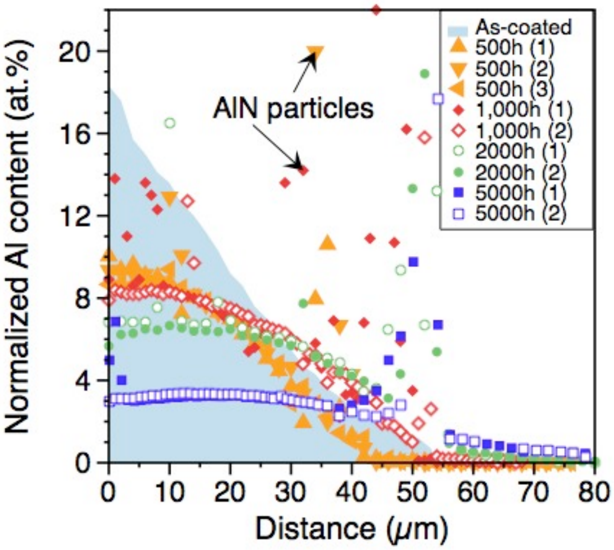

Figure 3. Normalized Al content by EPMA as a function of depth for coated Gr.92 specimens after exposure for 500-5,000h at 700°C in Pb-Li. A typical as-coated Al profile is shown in shaded area.

contents, intermetallic (Fe-Al) phases begin to form and an inner and outer layer is evident, Figure 4a. (Note that the magnifications in Figures 2 and 4 are different.) The outer layer likely grew by outward diffusion of Fe while the inner layer by inward Al diffusion.[19] In some locations, the outer layer was absent (e.g. Figure 4b), a likely explanation for the large mass loss. In addition to the AlN precipitates, this coating apparently contains a large number of voids, some filled or partially filled with oxide. The composition has not been evaluated but these voids are likely Kirkendall-type, formed due to the loss of Al during exposure. One advantage of the thinner coating is that the Fe(Al) coating phase has a similar coefficient of thermal expansion (CTE) as the substrate.[21] However, the intermetallic phases (particularly Fe_3Al and FeAl) all have significantly higher CTEs, thus thermal strains due to the CTE differential may have caused spallation. In Figure 4a, there also appears to be oxide formed at the interface between the inner and outer coating layers. This has been observed during steam and wet air oxidation of similar coatings and was attributed to cracking or other imperfections in the outer coating

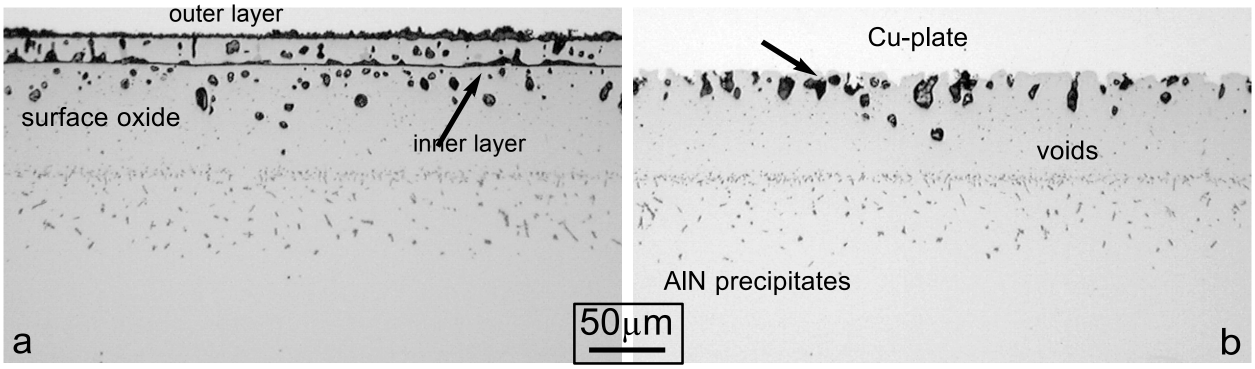

Figure 4. Light microscopy of high-Al content coating on Grade 92 specimen exposed to Pb-Li for 5,000h at 700°C. In (b), the outer coating layer has been lost during exposure.

allowing ingress of oxygen to this interface.[21] The combination of oxidation and void formation at the interface may have sufficiently weakened the interface between the inner and outer layer to cause the observed spallation. Based on this result, pursuing coatings with a larger Al reservoir does not appear to be a promising strategy. For the highest temperature compatibility, an Al containing alloy appears to be a more promising strategy for a structural alloy with long term Pb-Li compatibility.

Regarding construction of a Pb-Li thermal convection loop, Kanthal APMT (FeCrAl) tubing [22] has been purchased. At this time, a supplier has not yet been identified for 9Cr steel tubing because of the small (~50m) quantity of tubing required. A supplier is being identified for the needed Pb-Li. The first loop should be ready for operation in late 2013, targeting operation of 550°C peak temperature for 1000h with a temperature gradient of approximately 100°C. A similar harp shaped loop was designed and operated at ORNL in 2007 with V-4Cr-4Ti tubing and flowing Li.[23]

REFERENCES

[1] M. Abdou, D. Sze, C. Wong, M. Sawan, A. Ying, N. B. Morley and S. Malang, *Fus. Sci. Tech*nol. **47** (2005) 475.
[2] B. A. Pint, *Fus. Sci. Technol.* **52** (2007) 829.
[3] B. A. Pint and K. L. More, *J. Nucl. Mater*. **376** (2008) 108.
[4] B. A. Pint, *Mater. Sci. Forum* **595-598** (2008) 549.
[5] B. A. Pint, *J. Nucl. Mater*. **417** (2011) 1195.
[6] B. A. Pint, L. R. Walker and K. A. Unocic, *Mater. High Temp*. **29** (2012) 129.
[7] B. A. Pint and K. A. Unocic, *J. Nucl. Mater.* in press.
[8] B. A. Pint and K. A. Unocic, DOE/ER-0313/50 (2011) 115.
[9] B. A. Pint and K. A. Unocic, DOE/ER-0313/51 (2011) 73.
[10] J. E. Battles, *Intern. Mater. Rev.* **34** (1989) 1.
[11] P. Hubberstey, *J. Nucl. Mater*. **247** (1997) 208.
[12] T. Yoneoka, S. Tanaka and T. Terai, *Mater. Trans*. **42** (2001) 1019.
[13] O. K. Chopra, D. L. Smith, P. F. Tortorelli, J. H. DeVan and D. K. Sze, *Fusion Technol*. **8** (1985) 1956.
[14] J. Konys, W. Krauss, J. Novotny, H. Steiner, Z. Voss and O. Wedemeyer, *J. Nucl. Mater.* **386-88** (2009) 678.
[15] S. Ukai and M. Fujiwara, *J. Nucl. Mater.* **307** (2002) 749.
[16] G. R. Romanowski, L. L. Snead, R. L. Klueh, and D. T. Hoelzer, *J. Nucl. Mater.* **283-287** (2000) 642.
[17] R. L. Klueh, J. P Shingledecker, R. W. Swindeman, and D. T. Hoelzer, *J. Nucl. Mater*. **341** (2005) 103.
[18] D. A. McClintock, M. A. Sokolov, D. T. Hoelzer and R. K. Nanstad, *J. Nucl. Mater*. **392** (2009) 353.
[19] Y. Zhang, B. A. Pint, K. M. Cooley and J. A. Haynes, *Surf. Coat. Technol.* **202** (2008) 3839.
[20] A. Rouaix-Vande Put and B. A. Pint, *Surf. Coat. Technol.* **206** (2012) 5036.
[21] B. A. Pint and Y. Zhang, *Mater. Corros*. **62** (2011) 549.
[22] B. Jönsson, R. Berglund, J. Magnusson, P. Henning and M. Hättestrand, *Mater. Sci. Forum* **461-464** (2004) 455.
[23] B. A. Pint, S. J. Pawel, M. Howell, J. L. Moser, G. Garner, M. Santella, P. F. Tortorelli, F. W. Wiffen and J. R. Distefano, *J. Nucl. Mater.* **386-388** (2009) 712.

7.1 Progress on Developing an Atomistic Equation of State for Helium in Iron —

R. E. Stoller and Y. N. Osetskiy (Oak Ridge National Laboratory)

OBJECTIVE

The objective of this research is to develop the modeling and simulation tools necessary to improve our understanding of how helium interacts with other defects in iron-based alloys to produce changes in the microstructure and mechanical properties.

SUMMARY

A large series of molecular dynamics simulations have been completed to map out the pressure-temperature relationship for helium in iron to provide the basis for fitting of a new equation of state for helium bubbles. The behavior of helium is described by the three-body Fe-He potential developed at ORNL under the fusion program.

PROGRESS AND STATUS

Introduction

Because of the high helium levels generated by nuclear transmutation reactions, predictions of structural material performance under DT fusion conditions must account for how the helium influences microstructural evolution and the related mechanical properties. One of the primary issues that must be addressed is the behavior of He-vacancy clusters, which evolve, into finite-sized bubbles with the potential for growing into voids. In this case, a ‘bubble’ is defined as a cavity, which is stabilized by the helium pressure it contains. If helium is removed a bubble will shrink. In contrast, a ‘void’ is a cavity, which has grown large enough that growth can be maintained by the absorption of a net vacancy flux. The gas pressure plays essentially no role in voids stability. The properties of small He-vacancy clusters, such as the helium and vacancy binding energy are critical to predicting bubble stability. These processes can only be accurately described by atomistic simulations such as molecular dynamics (MD), which requires an interatomic potential to describe the behavior of both the metal and helium atoms. In order to improve our predictive capability for the Fe-based materials of most interest to fusion structural applications, a new Fe-He interatomic potential was developed based on ab initio calculations of the interactions between He and point defects in Fe [1-2]. Additional work using this potential has characterized the properties of small He-vacancy clusters and parameters such as the He-to-vacancy ratio as a function if cluster/bubble size and temperature [3-4]. The observations of that work are being extended to develop an atomistic equation of state for helium in iron, which can then be applied in a broad range of mesoscale to predict microstructural evolution [5].

Current Progress

In order to provide a basis for fitting the pressure-temperature relationship required for the equation of state (EOS), a series of MD simulations have been carried out covering the temperature range of 200 to 100K with bubble radii from 0.25 to 5 nm. For each of the bubble size, the helum-to-vacancy ratio was varied to produce a broad range of pressures, from highly over-pressurized to a void-like under-pressurized state. The pressure at mechanical equilibrium was also being determined.

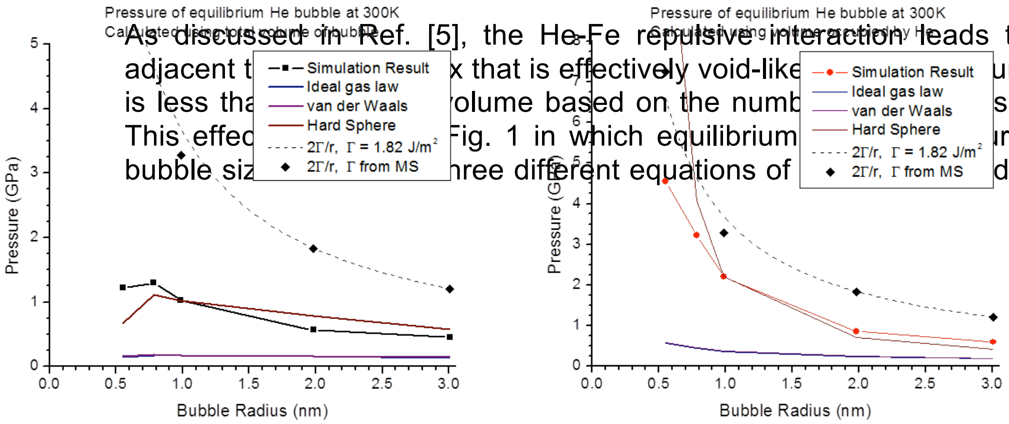

Fig. 1. Influence of gas-free region near the bubble surface on the equilibrium pressure calculated for helium bubbles in iron.

As discussed in Ref. [5], the He-Fe repulsive interaction leads to a region of the bubble adjacent t x that is effectively void-like ume occupied by the helium is less tha olume based on the numb s that comprise the bubble. This effec Fig. 1 in which equilibrium re is shown for a range of bubble siz hree different equations of d to calculate the pressures and are compared with the pressure obtained in the MD simulations. For part (a) the pressure was calculated using the total bubble volume and in part (b) using only the volume occupied by helium. The difference is dramatic for the smaller bubble sizes in which the helium-free volume is a significant fraction of the total volume. Note that the equilibrium pressure predicted by the capillarity model (2G/r) is generally much higher than that obtained in the MD simulations. The hard sphere EOS of Brearley and MacInnes [6] is reasonably consistent with the MD results and will be used as the basis for developing the MD-based EOS.

The influence of gas pressure or He/vacancy ratio is illustrated in Fig. 2, which compares the He atom, pair correlation functions obtained at different pressures at 600K. More liquid or solid-like behavior observed for at the higher He/vacancy ratios, i.e. there is clear evidence of the formation of a He atom lattice in the curve for a He/vacancy ratio of 1.5. The helium atoms are more gas-like and randomly distributed at lower He-vacancy ratios.

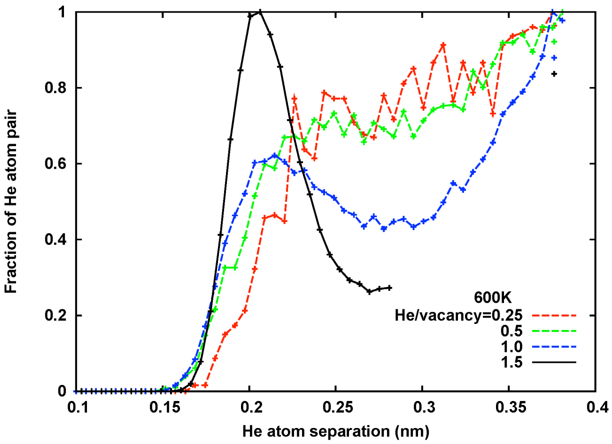

Fig. 2. He atom pair correlation function in bubbles at 600K for different pressures (He/vacancy ratios).

REFERENCES

1. T. Seletskaia, Yu. N. Osetsky, R. E. Stoller, and G. M. Stocks, “Development of a Fe–He Interatomic Potential Based on Electronic Structure Calculations,” *J. Nucl. Mater.* **367-370** (2007) 355-360.
2. R. E. Stoller, S. I. Golubov, P. J. Kamenski, T. Seletskaia, and Yu. N. Osetsky, “Implementation of a New Fe-He Three-body Interatomic Potential for Molecular Dynamics Simulations,” *Phil. Mag.* **90** (2010) 923-934.
3. D. M. Stewart, Yu. N. Osetsky, R.E. Stoller, S. I. Golubov, T. Seletskaia, P.J. Kamenski, “Atomistic Studies of Helium Defects Properties in BCC Iron: Comparison of He–Fe Potentials,” *Philos. Mag.* **90** (2010) 923.
4. D. M. Stewart, Yu. N. Osetskiy and R. E. Stoller, “Atomistic Studies of Formation and Diffusion of Helium Clusters and Bubbles in BCC Iron,” *J. Nucl. Mater.* **147** (2011) 1110-1114.
5. R. E. Stoller and Y. N. Osetskiy, in Fusion Reactor Materials Semiannual Progress Report, DOE/ER-0313/52, June 30, 2012 (Oak Ridge National Laboratory), pp. 134-136.
6. I. R. Brearley and D. A. MacInnes, “An Improved Equation of State for Inert Gases at High Pressures,” *J. Nucl. Mater.* **95** (1980) 239-252.

7.2 Atomistic Studies of Helium Bubble Nucleation at Grain Boundaries in α-Fe —

L. Yang, F. Gao, H. L. Heinisch and R. J. Kurtz (Pacific Northwest National Laboratory)[1]

OBJECTIVE

To simulate the nucleation and growth of He bubbles at grain boundaries (GBs) in α-Fe using the newly developed Fe-He potential and to study the evolution of the GB structures due to the accumulation of He atoms and the nucleation and growth of He bubbles.

SUMMARY

Experimental results and atomistic calculations demonstrate that GBs act as sinks to trap He atoms in α-Fe. The nucleation and growth of He bubbles at GBs are likely to determine the extent of embrittlement which is potentially one of the most serious material problems related to the development of fusion power. The nucleation of He bubbles in the bulk and at GBs in α-Fe have been previously studied [1-3] using molecular dynamics with our newly developed Fe-He potential [4]. It was found that the evolution of the GB configurations, the accumulation of He atoms and the nucleation of He bubbles all depend on the He concentration, temperatures and the GB configurations. In the bulk of α-Fe, the computational results showed that complexes consisting of a dislocation loop with helium-vacancy (He-V) clusters are formed at high He concentrations [2]. In order to understand the formation and evolution of interstitial dislocation loops due to the growth of He bubbles in the helium-rich vacancy-poor situation, the clustering of He and the growth of He bubbles at two GBs in α-Fe is currently being investigated. It has been found that within the S3 GB, when the size of a He cluster is large enough, a 1/2 <111> dislocation loop is formed, accompanied by the emission of the dislocation loop. However, in the S73b GB the sequential insertion of He atoms induces the emitted self-interstitial atoms (SIAs) to rearrange at the core of the inherent dislocation, leading to the propagation of the dislocation along the [-1 -1 12] direction. The small He bubbles form longitudinal shapes along the dislocation line in the S73 GB, a shape commonly observed at GBs in experiments.

PROGRESS AND STATUS

Introduction

It is well known that helium atoms are expected to be produced at a high rate by (n, α) transmutation reactions in a fusion reactor first wall under irradiation. Because of the extremely low solubility of He in materials, a high concentration of helium will tend to be trapped at defects, such as vacancies, dislocations, and grain boundaries (GBs), which leads to void swelling and produces low-temperature intergranular embrittlement, surface roughening, blistering, and premature creep rupture at high-temperatures. These phenomena can significantly degrade the mechanical properties of materials. Therefore, understanding of the He accumulation and the growth of He bubbles both in the bulk and GBs are of fundamental importance within a fusion reactor environment. Atomistic studies of the nucleation and growth of He bubbles within the Σ3 and Σ73b GBs in α-Fe are being performed. In the present simulations the pair interaction and the many-body function for Fe−Fe interactions are those of Ackland [5], while the pair potential for He−He interaction is the Aziz potential [6]. The new Fe−He potential developed at PNNL [4] is used

---

[1] This work was supported by the U.S. Department of Energy, Office of Fusion Energy Sciences. PNNL is operated by Battelle Memorial Institute for the U.S. DOE under Contract DE-AC-06-76RLO 1830.

to describe the Fe−He interaction. This set of potentials was used previously to investigate the nucleation of He clusters and bubbles in the bulk and at the GBs in α-Fe, and the formation and evolution of defects, as well as to study the effects of these phenomena on microstructural changes [3]. That investigation found that the evolution of the GB configurations, the accumulation of He atoms and the nucleation of He bubbles all depend on the He concentration, temperatures and the GB configurations. It is of interest to note that <100> dislocation loops are directly formed at the peripheries of these large He clusters in the Σ3 GB at 600 K and 800 K. At high He concentrations, the large number of SIAs that are emitted can rearrange to form an extra atomic plane within the Σ3 GB, resulting in the self healing of the deformation induced by He accumulation and the GB climbing along the [-112] direction. However, a large number of SIAs emitted by He atoms can cause the climb of the GB dislocations along the $[1112]$ direction in the ∑73b GB, and the climb is more significant with increasing temperature. In the bulk, at low He concentrations SIA clusters (or the dislocation loops that are formed from the SIA clusters) are attached to He-V clusters, while at high He concentrations He-V cluster-loop complexes with more than one He-V cluster are formed. In the work mentioned above [2], He atoms were inserted at random positions within the bulk or the stressed region around the GB plane of α-Fe, mimicking the He accumulation at different concentrations. In the present work the nucleation and growth of small He bubbles and the formation and evolution of SIAs and dislocation loops are investigated at both the ∑3 and ∑73b GBs in α-Fe as He atoms are inserted one by one into each GB.

Simulation Methods

Two symmetric tilt GBs with a common <101> tilt axis (Σ3 and Σ73b) were created to investigate the nucleation and growth of small He bubbles in the GBs. The block sizes of the Σ3 and Σ73b GBs are 84.07Å × 79.00Å × 80.69Å and 103.50 Å × 70.00 Å × 80.76 Å, consisting of 45,560 and 48,000 Fe atoms, respectively. Periodic boundary conditions are imposed along the x and z directions, but fixed boundary conditions are applied along the y direction, where the x, y and z represent the [1-11], [-112] and [-1-10] directions in the Σ3 GB model, and the [1 12 -1], [-616] and [101] directions in the Σ73b GB model.

The NVT (constant number of atoms, volume and temperature) ensemble is chosen in the present simulations with a time step of 1 fs. He atoms are inserted one by one into the simulation boxes. After each helium atom insertion, the configuration is quenched to 0 K, followed by a temperature rescaling to 300 K and an additional 100 ps to anneal at the same temperature. For the insertion of the next He atom, the configuration is quenched back to 0 K, the temperature is rescaled to 300 K, and the simulation block is equilibrated for 100 ps. A similar procedure is repeated during the simulations.

Results and Discussion

The first He atom is inserted into a most favorable interstitial site in the GB plane. After inserting 4 He atoms in the ∑3 GB, the He cluster moves slightly away from the GB plane and a <111> crowdion SIA is created within the GB plane. The emitted SIA quickly migrates along the <111> direction within the GB plane during the annealing process because of its small migration energy (0.01 eV). After the ninth He is inserted, the displacements of the Fe atoms around the He cluster increase, leading to a few Fe atoms near the He cluster being displaced from their original sites along the <111> and <112> directions, which releases the pressure accumulated during the insertion of He atoms. However, the maximal displacement of the Fe atoms around the He cluster is less than 1 Å. The insertion of the 11th He atom results in forming the second

<111>crowdion SIA. The addition of the 13th He atom leads to the formation of the third <111> crowdion SIA, and most of the displaced Fe atoms around the He cluster return to their original positions. With further insertion of He atoms, more SIAs are formed, but all the SIAs are collected at the periphery of the He cluster.

It is of interest to note that after inserting 45 He atoms, a dislocation loop with a Burgers vector of b = 1/2<111> is clearly formed. Fig. 1 shows the structures and atomic configurations of the ∑3 GB in α-Fe before and after annealing for the 45 He atoms inserted.

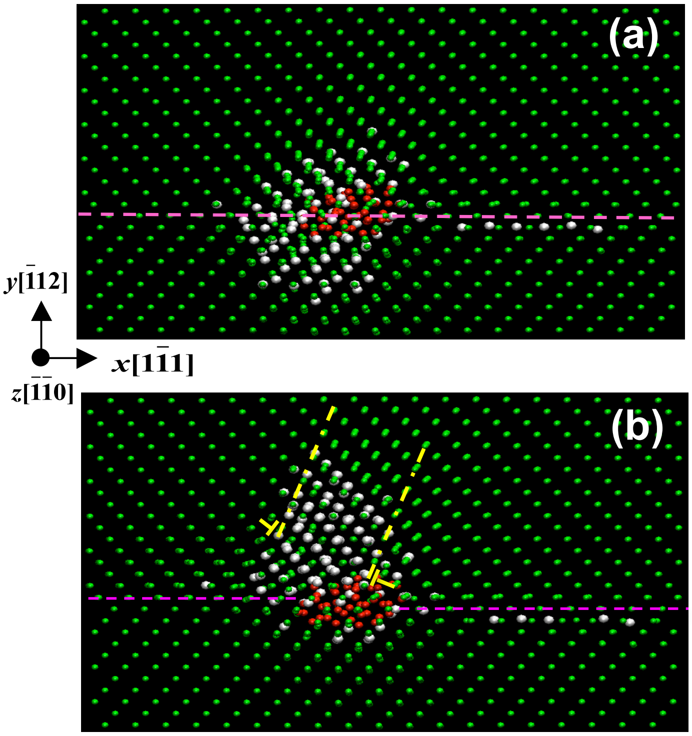

Fig. 1. Atomic configurations of the Σ3 GB together with the cluster of 45 He atoms in α-Fe: (a) before annealing and (b) after annealing 0.1ns at 300 K, where red spheres are He atoms, white spheres represent the Fe atoms with the stress of 8 GPa and larger, green spheres represent the Fe atoms with the stress of less than 8 GPa, purple dashed lines indicate the grain boundary plane.

It is clearly seen that the large number of SIAs formed at the periphery of the He cluster are distributed on both sides of the GB plane. However, during the annealing process, most SIAs move along the [-112] direction from the bottom of the GB plane to the top of GB plane after 27,000 MD steps. Within a short time (about 17 ps), a ***b*** = 1/2<111> dislocation loop is formed and attached to the He cluster on one side of the GB plane. Also, it can be seen that the GB plane on the right of the He cluster remains the same after the formation of the dislocation loop, but that on the left of the He cluster the GB climbs up one atomic layer along the [-112] direction. This might be attributed to the interaction of the GB plane with the SIAs as they migrate through the GB plane. With further insertion of He atoms, the dislocation loop is observed to grow larger by collecting more SIAs. Finally, the dislocation loop with a total of 45 SIAs is emitted from the He bubble after inserting 97 He atoms.

In order to more generally understand the effects of GB structure on the growth of He bubbles and the formation of SIAs in α-Fe, the same approach is applied to study the nucleation and growth of He clusters or bubbles in a ∑73b<110>{661} GB. The nucleation and formation of He clusters and SIAs in the ∑73b GB is significantly different from that observed in the ∑3 GB, primarily because the ∑73b GB is a low angle GB containing intrinsic dislocations distributed along the [-1 -1 12] direction. The first He in the ∑73b GB is inserted in a most favorable interstitial site near the dislocation core, such that an Fe atom is pushed away from its lattice site and the He shares the lattice vacancy with the Fe atom, forming a Fe-He dumbbell along the <111> direction within the dislocation core. When the second, third and fourth He atoms are inserted, the Fe atoms near the He atoms are displaced slightly, but they are still associated with their sites. After the insertion of the 5th He atom, a second Fe is emitted from the He_5 cluster. It is of interest to note that the two SIAs prefer to distribute along the [-1 -1 12] direction within the dislocation core, evidently being attracted by the excess volume within the dislocation core. During further insertion of He atoms, more Fe atoms around the He cluster are pushed out from their lattice sites and aggregate at the dislocation core. Fig. 2 shows the configurations of the Σ73b GB projected on different planes, along with the cluster of 83 He atoms. It is clear that many SIAs are formed within the dislocation core, and they prefer staying within the core due to the strong interaction of the SIAs and the core.

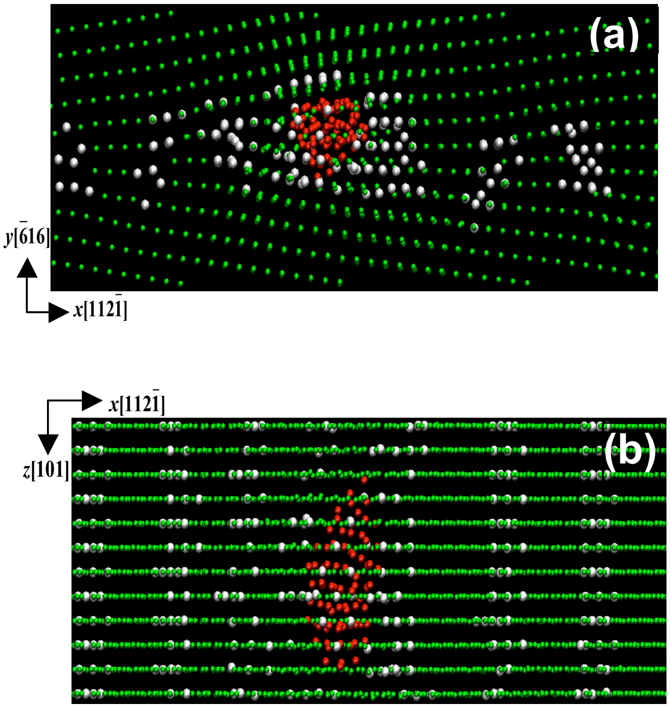

Fig. 2. Atomic configurations of the Σ73b GB together with the cluster of 83 He atoms projected on: (a) the (101) plane and (b) the (-616) plane, where the representation of spheres are the same as those in Fig. 1.

The He atoms are distributed along the dislocation line in the ∑73b GB, forming a longitudinal platelet-like shape that is often observed in experiments. Most of the SIAs at the periphery of the He cluster are reconstructed along the [-1 -1 12] direction, leading to the migration of the dislocation along the [-1 -1 12] direction.

CONCLUSION

The nucleation and growth of He bubbles in the S3 and S73b GBs in α-Fe are studied using molecular dynamics, and the evolution of the material structures due to the He accumulation and the growth of He bubbles is analyzed in detail. It was found that the nucleation and growth of He bubbles, as well as the formation of SIAs, at the different GBs is significantly different. In the S3 GB a 1/2 <111> dislocation loop is formed and emitted by the increasing size of the He bubble. However, in the S73b GB the insertion of He atoms induces the intrinsic dislocation to migrate along the [-1 -1 12] direction. Also, it is observed that in the S3 GB the He bubble is almost spherical, but in the S73b GB it has a longitudinal shape along the dislocation line.

REFERENCES

[1] L. Yang, F. Gao, H. L. Heinisch, and R. J. Kurtz, In *DOE/ER-0313/50-Volume 51 Semiannual Progress Report December 31, 2011*.

[2] L. Yang, H. Q. Deng, F. Gao, H. L. Heinisch, R. J. Kurtz, S. Y. Hu, Y. L. Li, and X. T. Zu, to be published in *Nucl. Instr. Meth. B*.

[3] N. Gao, H. Van Swygenhoven, M. Victoria, and J. Chen, *J. Phys.: Condensed Matter* **23** (2011) 442201.

[4] F. Gao, H. Q. Deng, H. L. Heinisch, and R. J. Kurtz, *J. Nucl. Mater.* **418** (2011) 115.

[5] G. J. Ackland, M. I. Mendelev, D. J. Srlolovitz, S. Han, and A. V. Barashev, *J. Phys.: Condensed Matter* **16** (2004) s2629.

[6] R. A. Aziz, A. R. Janzen, and M .R. Moldover, *Phys. Rev. Lett.* **74** (1995) 1586.

7.3 Theory of a Quodon Gas with Application to Precipitation Kinetics in Solids Under Irradiation

— V. I. Dubinko, R. V. Shapovalov (NSC Kharkov Institute of Physics and Technology), S.Y. Hu, Y.L. Li, C.H. Henager, Jr. and R.J. Kurtz (Pacific Northwest National Laboratory)

Extended abstract based on results that will be reported in the Springer Series on Wave Phenomena- Special Volume LENCOS [1] and NIMB_PROCEEDINGS-D-12-00109R1 [2].

OBJECTIVE

The rate theory of microstructure evolution in solids has been modified to account for the production of Schottky defects at surfaces of extended defects due to their interaction with the radiation-induced lattice excitations that primarily affect one-dimensional transport mechanisms. These modifications appear to be necessary in order to understand important radiation-induced rate processes, such as irradiation creep, radiation-induced annealing of voids, saturation of void growth under high dose irradiation, and void lattice formation.

SUMMARY

The difference in the ability to absorb point defects by extended defects is a main driving force of microstructural evolution under irradiation [3]. Another driver for radiation-induced microstructural evolution is based the forced atomic relocations resulting from nuclear collisions, a.k.a. ballistic effects [4] that have been taken into account for the explanation of the dissolution of precipitates under cascade damage. Later on it was recognized that the so-called “thermally activated” reactions may be strongly modified by irradiation resulting in the radiation-induced production of Schottky defects [3, 4-8], which has essentially the same physical nature as the ballistic effects, but, in contrast to the latter, it operates under both cascade and non-cascade damage conditions, including sub-threshold electron irradiation that does not produce stable Frenkel pairs. The underlying mechanisms for these processes are based on the interaction of extended defects with unstable Frenkel pairs, focusing collisions (a.k.a. focusons) and with lattice solitons. The latter can be mobile, and these are referred to below as quodons, which are stable quasi-particles that propagate one-dimensionally and transfer energy along the close packed directions of the lattice. Quodons may have more technological significance than focusons due to much longer propagation ranges expected from the nonlinear theory and demonstrated experimentally [8, 9]. This points to the necessity of the modification of the chemical rate theory to account for the quodon-induced energy deposition to the reaction area. Accordingly, the rate theory of microstructure evolution in solids has been modified to account for the production of Schottky defects at surfaces of extended defects due to their interaction with the radiation-induced lattice excitations [3, 5-8]. The modified theory predictions include important phenomena, which have not been properly understood before, such as irradiation creep [5, 6], radiation-induced annealing of voids [3, 7], saturation of void growth under high dose irradiation and void lattice formation [8].

PROGRESS AND STATUS

Introduction

Until recently the evidence for the existence of lattice solitons provided by molecular-dynamics simulations was restricted mainly to one and two-dimensional networks of coupled nonlinear oscillators with simple “toy” potentials (see e.g. [10]), whereas reports on their observation in three-dimensional systems using “realistic” molecular-dynamics potentials were scarce and restricted to alkali halide crystals [11]. The lattice solitons found in these simulations always drop down from the optical band(s) into the phonon gap, and hence become unstable. Consequently, it has been assumed that the softening of atomic bonds with increasing vibrational amplitude is a general property of crystals, and therefore lattice solitons with frequencies above the top phonon frequency cannot occur. However, in their recent paper, Haas et al [1] have provided a new insight on this problem by demonstrating that the anharmonicity of metals appears to be very different from that of insulators. As a result, in some metals, lattice solitons may exist with frequency *above the top of the phonon spectrum*. Using the known literature values of the pair potentials, Haas et al have found that in Ni and Nb this condition is fulfilled. Their molecular-dynamics simulations of the nonlinear dynamics of Ni and Nb confirmed that high-frequency lattice solitons may exist in these metals, and their corresponding energies may be relatively small, starting from threshold energy of 0.2 eV, just above the phonon band. These results allow us to look at the modification of the rate theory based on the quodon dynamics from a different perspective as compared to the one proposed in refs [3, 5-8]. Initially it has been assumed that the main difference between quodons and focusons is in their path lengths. Accordingly, it was postulated that (i) the quodon production rate was equal to the focuson production rate; and (ii) similar to focusons, quodons could eject vacancies from extended defects provided that their energies exceeded the vacancy formation energy. This mechanism is close to the classical ballistic mechanism of the precipitate dissolution under cascade damage [1]. However, in view of the new results [12], one can assume that irradiation may produce quodons with energies almost as low as that of phonons, which are lower than typical focuson energies by orders of magnitude. This assumption is the basis of the model proposed in [2], which has been applied in [1] for modeling of the nucleation and growth of copper precipitates in *FeCu* binary alloys under electron irradiation [13].

Theory

It is known that even in the case of displacement damage, only a small part of the energy of impinging particles is spent on generation of stable Frenkel pairs (that require 20-40 eV each) and their clusters (in energetic displacement cascades), while the major part of energy is dissipated into heat, or in other words, it is spent on generation of phonons.

The first main assumption made in [1, 2] is that *quodons are the transient form of the heat generation under irradiation*, which means that they are constantly generated by irradiation, and subsequently lose energy by generating phonons. Let K_q be the average rate of quodon generation (per atomic site per second), which should be proportional to the flux of impinging particles, F_{irr}, and the energy deposition density by one particle, dE_{irr}/dx, and inversely proportional to the mean quodon energy,

$\langle E_q \rangle$:

$$K_q\left(F_{irr}\right)=k_{eff}^q F_{irr}\left(\frac{dE_{irr}}{dx}\right)\frac{w}{\langle E_q\rangle}, \tag{1}$$

Where w is the atomic volume, and k_{eff}^q is the quodon production efficiency that depends on material and irradiation conditions and can range from zero (no quodon generation) to unity (e.g. under sub-threshold irradiation that does not produce stable defects).

Then the mean density of quodon gas under steady-state irradiation (the number of quodons per unit volume) will be given simply by the product of their mean generation rate and the lifetime, τ_q:

$$N_q\left(F_e,T_{irr}\right)=\frac{K_q\left(F_e,E_e\right)\tau_q}{w},\ \tau_q\left(T\right)=\frac{l_q\left(T\right)}{c_q}, \tag{2}$$

Where c_q is the quodon propagation speed, which is assumed below to be close to the sound velocity, c_s, and $l_q\left(T\right)$ is the quodon propagation range before decay.

From a quantum theory of intrinsic localized modes it is known that they decay by generating phonons. Similar to that, quodons are assumed to lose energy in quodon-phonon collisions *by portions (or quanta)* ΔE_{qp}. Then the mean quodon propagation range may be written as

$$l_q\left(T,\langle E_q\rangle\right)=\frac{\langle l_{qp}\left(T\right)\rangle}{\varepsilon_{pq}},\ \varepsilon_{pq}\equiv\frac{\Delta E_{qp}}{\langle E_q\rangle}, \tag{3}$$

where $\langle l_{qp}\left(T\right)\rangle$ is the mean length of quodon free path between collisions with phonons, which is determined by a well known formula for a 1-D propagating particle in a medium with scattering centers of a given density and cross-section:

$$\langle l_{qp}\left(T\right)\rangle=\frac{1}{\pi R_{qp}^2\langle N_p\left(T\right)\rangle},\ \langle N_p\left(T\right)\rangle=\frac{1}{w}\frac{1}{\exp\left(\frac{\hbar\omega_D}{k_B T}\right)-1}, \tag{4}$$

Where R_{qp} is the effective quodon-phonon cross-section radius, $\langle N_p\left(T\right)\rangle$ is the density of phonons having a high-frequency ω_D (a.k.a. Debye phonons), k_B is the Boltzmann constant and *T* is the temperature. We assume here for simplicity that Debye phonons are the main contributors to the quodon decay due to the loss of energy in each collision between them represented by the energy coupling parameter $\Delta E_{qp}\approx\hbar\omega_D$. These and other material parameters used in the calculations are listed in ref [1].

The quodon-phonon cross-section radius is extremely small (~10^{-12} m), and so the quodon propagation range can reach tens of centimeters (Fig. 1), which agrees with experimental data on tracks produced by quodons in mica muscovite [9]. These enormous ranges in real crystals that contain structural defects can be understood only assuming that quodons can both lose and gain energy in the scattering process with extended defects. So the second main assumption of the model [1, 2] is that in the collision events between quodons and extended defects, *quodons lose and gain energy with equal probability*.

As can be seen from Fig. 1, the quodon generation rate under irradiation conditions [13] can exceed the displacement rate by 6 orders of magnitude, and the density of quodon gas becomes comparable to that of Debye phonons at the electron flux of $10^{24} m^{-2} s^{-1}$, which corresponds to the displacement rate of ~5 x 10^{-3} s^{-1} that is a typical value for radiation damage studies using electron beams. So we may conclude that under irradiation a crystal contains a mixture of "gases" of quasi-particles, namely, almost equilibrium phonons and strongly non-equilibrium quodons, the densities of which may be comparable. After irradiation is switched off, quodons transfer their energy to phonons and disappear over a short relaxation time $\sim \tau_q \approx 7 \times 10^{-5}$ s, as the crystal attains a thermal equilibrium state. In the following section, we consider the effect of quodon gas on chemical reaction rates under irradiation.

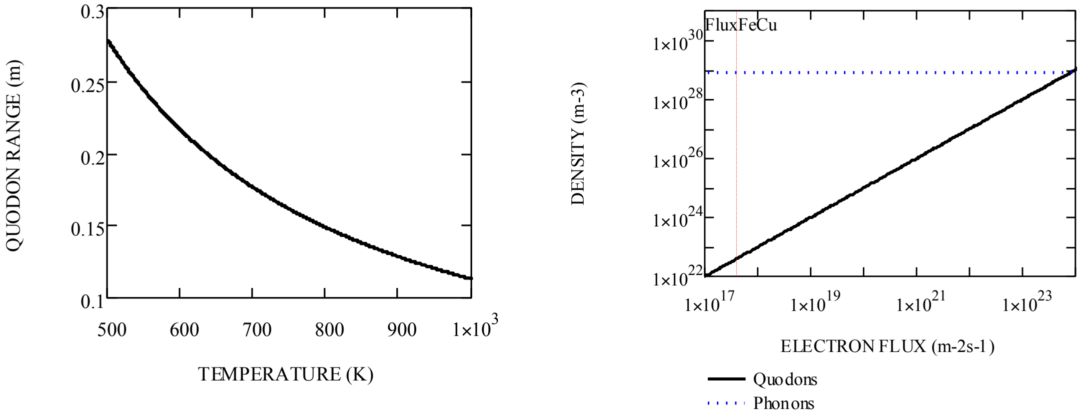

Figure 1. The temperature dependence of the quodon propagation range $l_q(T)$ and the density of quodon gas vs. electron flux, $F_{irr} = F_e$ at the irradiation temperature 563 K. The vertical dotted line corresponds to irradiation flux [13]. Density of the gas of Debye phonons at 563 K is shown for comparison.

RESULTS

It is known that the "gas" of phonons is responsible for the temperature effect on the reaction rates, $\dot{R}$, which is expressed by Arrhenius' law:

$$\dot{R} = \omega_p \exp\left(-\frac{E_a}{k_B T}\right), \tag{5}$$

Where ω_p and E_a are the frequency factor and the activation barrier, respectively. The reaction activation barrier is determined by the maximum *free energy change* of the system imposed by reaction (a.k.a. the free energy barrier). Phonons represent thermal fluctuations acting on a system (e.g. point defect and its surrounding) and helping it to overcome the barrier.

On the other hand, unlike phonons, which are delocalized, quodons are strongly localized on several lattice sites, and in the collision event between a quodon and an extended defect (ED), the latter can gain (or loose) some portion of energy at the place of collision, and so the resulting energy of the system including the ED will undergo stochastic deviations from its average value. Accordingly, the Arrhenius' law (5) can be rewritten with account of the energy exchange between quodons and the "reaction area":

$$\dot{R} = \omega_0 \exp\left(-\frac{E_a^q}{k_B T}\right),\ E_a^q \equiv \left\langle E_a \right\rangle - \Delta E_a,\ \Delta E_a \equiv \frac{\left\langle V_q^2 \right\rangle - \left\langle V_q \right\rangle^2}{2k_B T}, \tag{6}$$

Where the brackets $\langle\ \rangle$ designate the integration over the Gibbs ensemble so that $\langle E_a \rangle$ is simply the average activation energy, while the second term in eq. (6) is <u>always negative</u> and it is proportional to the square of the energy dispersion due to quodon-induced fluctuations. This result means that under irradiation <u>all reaction barriers</u> in a crystal may be decreased by a value that depends on the statistics of the "gas" of quodons and their coupling with structural defects. It can be shown that at steady state the energy dispersion in eq. (6) can be expressed via the quodon propagation range l_q and generation rate K_q, which is proportional to the <u>flux</u> of impinging particles F_{irr} (see eq. (1)). Accordingly, one can express the modified reaction rate as follows [1, 2]:

$$\dot{R} = \dot{R}_0 A\left(f_{irr}\right),\ A\left(f_{irr}\right) = \exp\left(\frac{k_{mat} F_{irr}}{\left(k_B T\right)^2}\right), \tag{7}$$

where $\dot{R}_0$ is the reaction rate in the ground state (no irradiation) and $A\left(f_{irr}\right)$ is the reaction <u>amplification factor</u> due to the interaction with quodon gas, while k_{mat} is the coefficient determined by quodon statistics and material parameters.

The modified rate theory is applied to modeling of copper precipitation in *FeCu* binary alloys under electron irradiation characterized quantitatively by Mathon et al. [13] who described not only evolution of copper precipitates but also the time dependence of the concentration of copper atoms in the matrix, $C_{Cu}(t)$, both under thermal annealing at 773 K and under electron irradiation at 563 K. It appears that C_{Cu} at the end of the precipitation process, which corresponds to the copper *solubility limit*, is of the same order of magnitude in both cases. This result is in a marked disagreement with Arrhenius law that predicts the copper solubility limit at 563 K to be several orders of magnitude lower than observed.

In the present view, this contradiction is a very principal one, since the solubility limit value practically determines the rate of the nucleation and growth, and a failure to evaluate it in the classical rate theory makes it impossible to describe correctly the precipitation kinetics under irradiation. In all up to date models, the solubility limit under irradiation is assumed to be determined only by temperature, similar to the thermal case (see e.g. [14, 15], which is a <u>misleading assumption</u>.

In ref. [1], the rate theory of the precipitation kinetics is modified to account for non-equilibrium thermodynamics of “quodon gas” and its results are compared with results of the classical model (without quodon-induced effects) and with experimental data [13] as shown in Figs. (2, 3). One can see that the classical model disagrees strongly with experimental data on all precipitation parameters, and this discrepancy is especially pronounced for the copper solubility limit (Fig. 3). In contrast, the quodon-modified model describes quite well both the evolution of precipitates and the matrix concentration of copper measured by different methods. The latter fact seems to be of particular importance, since it reflects the principal difference between the two concepts, namely, the “classical” and the new one, in relation to the mechanisms of production of Schottky defects. In the classical theory they are assumed to be emitted by ED’s exclusively due to thermal fluctuations, which, in our language, are driven by phonons. In the modified rate theory we have taken into account essentially athermal fluctuation mechanisms based on the interaction of ED’s with radiation-induced quodons.

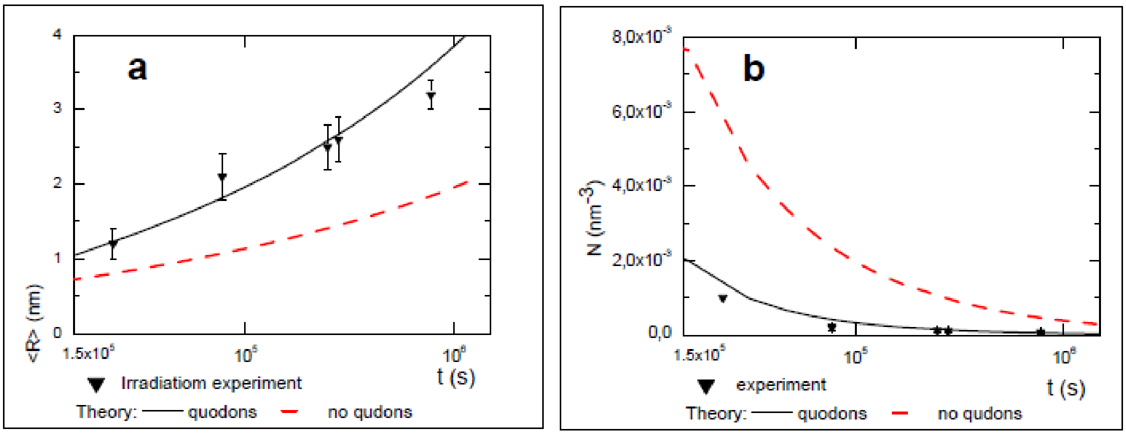

Figure 2. Time evolution of the Cu precipitate mean radius <R> and concentration N under irradiation vs. experimental data [13].

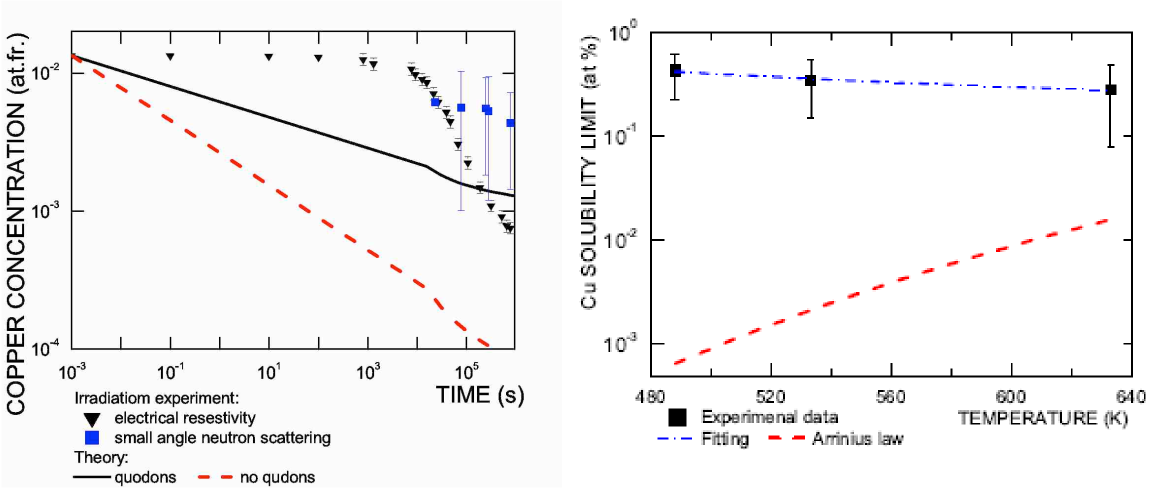

Figure 3. Time evolution of the concentration of copper atoms (left) and temperature dependence of the copper solubility limit under irradiation vs. Arrhenius law (right).

From a methodological side, the proposed concept of the radiation-induced "gas" of quodons offers a new insight on the radiation-induced processes in solids. It appears that *quodons are the transient form of the heat generation under irradiation* that subsequently transfers energy to phonons. The quodon gas may be a powerful driver of the chemical reaction rates under irradiation, the strength of which exponentially increases with irradiation flux and may be comparable with strength of the phonon gas that exponentially increases with temperature. Phonons obey the lows of equilibrium thermodynamics, such as the minimization of a system free energy, and the latter could not be defined for a crystal under irradiation in the classical framework. The proposed method of the free energy modification by taking into account non-equilibrium fluctuations of the potential landscapes for chemical reactions offers a new insight on the phase-field modeling (PFM) of radiation-induced processes in solids. Until now, PFM could not be applied to strongly non-equilibrium systems such as a crystal under irradiation, because it is based on minimization of a system free energy, which could not be defined for an irradiated crystal. Our method of the free energy modification by taking into account non-equilibrium fluctuations of potential energy landscapes for chemical reactions offers a way for development of a modified PFM, which will be able to describe the radiation-induced evolution of the microstructure.

REFERENCES

1. V. Dubinko and R. Shapovalov, Springer Series on Wave Phenomena- Special Volume LENCOS 2012, to be published.
2. V. I. Dubinko and A. V. Dubinko, NIMB Proceedings-D-12-00109R1.
3. V. I. Dubinko, S. Hu, Yu Li, C. H. Henager, Jr. and R. J. Kurtz, *Philos. Mag.* **92** (2012), doi:10.1080/14786435.2012.704425.
4. G. Martin, *Phys. Rev. B* **30** (1984) 1424.
5. V. I. Dubinko, *Radiat. Eff. and Defects Solids* **160** (2005) 85.
6. V. I. Dubinko and V. F. Klepikov, *J. Nucl. Mater.* **362** (2007) 146.
7. V. I. Dubinko, A. G. Guglya, and S. E. Donnelly, *Nucl. Instrum. Methods Phys. Res. B* **269** (2011) 1634.
8. V. I. Dubinko and F. M. Russell, *J. Nucl. Mater.* **419** (2011) 378.
9. F. M. Russell and J. C. Eilbeck, *Europhys. Lett.* **78** (2007) 10004.
10. J. F. R. Archilla, J. Cuevas, M. D. Alba, M. Naranjo, and J. M. Trillo, *J. Phys. Chem. B* **110** (2006)24112.
11. V. Hizhnyakov, D. Nevedrov, and A. J. Sievers, *Phys. B* **316–317**(2002)132.
12. M. Haas, V. Hizhnyakov, A. Shelkan, M. Klopov, and A. J. Sievers, *Phys. Rev. B* **84** (2011)144303.
13. M. H. Mathon, A. Barbu, F. Dunstetter, F. Maury, N. Lorenzelli, and C. H. de Novion, *J. Nucl. Mater.* **245** (1997) 224.
14. A. V. Barashev, S. I. Golubov, D. J. Bacon, P. E. J. Flewitt, and T. A. Lewis, *Acta Mater.* **52** (2004) 877.
15. Q. L. Wang and J. Z. Zhao, *Mater. Sci. Eng. A* **528** (2010) 268.

8.1 Molecular Dynamics Modeling of Atomic Displacement Cascades in 3C-SiC —

G. D. Samolyuk, Y. N. Osetskiy, and R. E. Stoller (Oak Ridge National Laboratory)

OBJECTIVE

The objective of this research is to investigate the damage in 3C-SiC induced at fusion irradiation condition and describes microscopic origin of these experimentally observed phenomena.

SUMMARY

A set of atomic displacement cascades was simulated using popular SiC Tersoff interatomic potentials. The types of created defects and their dynamics were analyzed. The validity of existing interatomic potentials was investigated by comparison of typical point defect diffusion barriers obtained using these potentials with first principles results.

PROGRESS

The purpose of this work is to develop a basic understanding of defect formation and evolution SiC. Initial 10 keV cascade simulations were carried out at a range of temperatures and indicated that in-cascade recombination seemed to be much lower than in metals. Simulations at 50 keV have shown the same behavior as indicated in Fig. 1. Fig. 1a shows the time dependence of defects obtained in a 50 keV SiC cascade at 600, and Fig. 1b shows typical results for similar simulations in iron. Note that the ratio of the peak defect count to the stable defect count at t>10 ps is less than a factor of two in SiC and almost two orders of magnitude in iron.

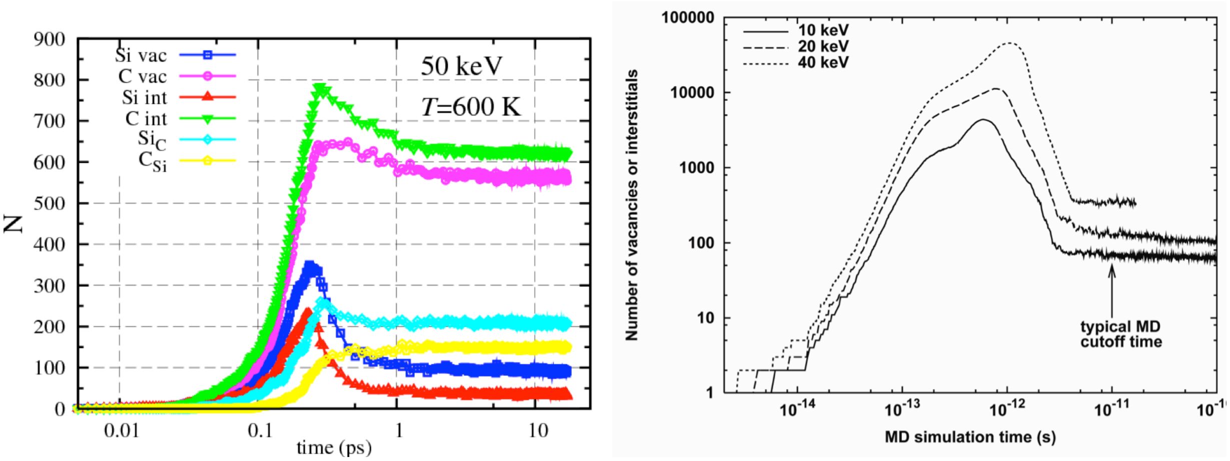

Fig. 1. Time dependence of the number of point defects observed in MD displacement cascade simulations: (a) 50 keV SiC cascade at 600 K and (b) 10, 20, and 40 keV cascades in iron.

Point defects in SiC consist of interstitials (I) and vacancies (V) of both carbon and silicon, as well as antisite defects of C on an Si site (C_{Si}) and Si on a C site (Si_C). The carbon defects predominate as shown by the green and purple symbols in Fig. 1a. Half of these V-I pairs are separated by a distance less than lattice parameter, and would normally be expected to recombine. Examples of these close-pair C(V)-C(I) are shown in Fig. 2 as large (I) and small (V) green spheres.

In order to understand this lack of recombination, the energy landscape in the region of a carbon interstitial was analyzed using the interatomic potential employed in these MD simulations and compared with first principles calculations using density functional theory (DFT). Some of the results are shown in Fig. 3, which plots the energy of a carbon atom moving in the [111] direction. Both the Tersoff potential used in this work and an alternate modified embedded atom method (MEAM) potential reveal a barrier to recombination which is much higher than the DFT results. The barrier obtained with a newer potential by Gao and Weber (GW) is closer to the DFT result but the overall energy landscape is significantly different.

These results suggest that essentially all of the cascade simulations that have been carried out previously for SiC are not representative of how the material will respond to irradiation. A new potential needs to be created using the whole set of defect properties obtained by DFT.

FUTURE WORK

In the next three months we are planning to simulate the cascades in SiC with GW potential in order to further assess the impact of the recombination barrier on stable defect formation. This will provide further insight that can be used to correct the current generation of interatomic potentials for SiC.

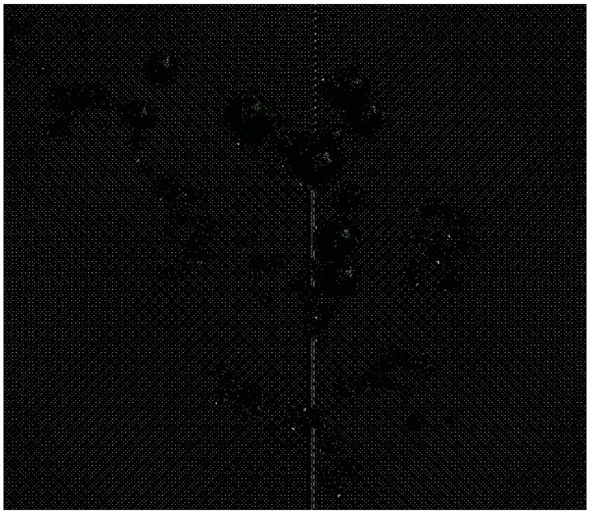

Fig. 2. Carbon (green) and silicon (red) interstitials (large spheres) and vacancies (small spheres) at the end of 50 keV Si recoil event in SiC. Blue and purples spheres correspond to Si_C and C_{Si} antisites, respectively.

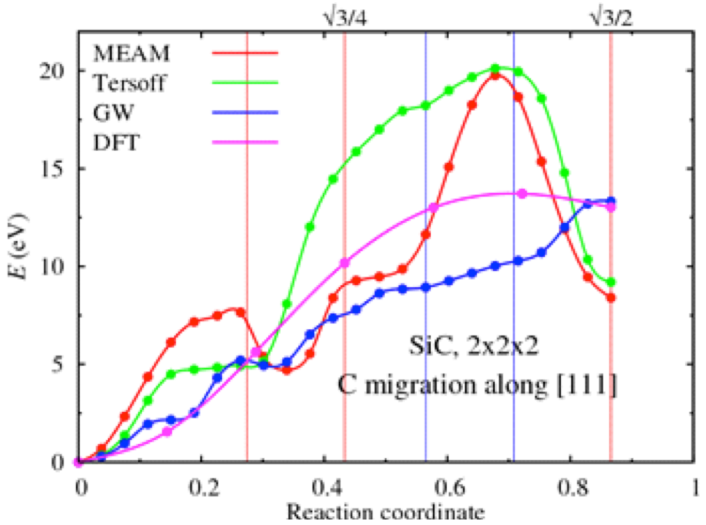

Figure 3. Carbon atom migration barrier in [111] direction.

8.2 Thermal Conductivity of SiC/SiC Composites – Porting PNNL EMTA Code for Fusion Analyses

— C. H. Henager, Jr. and Ba Nghiep Nguyen (Pacific Northwest National Laboratory,[1] Richland, WA 99336, USA)

OBJECTIVE

An existing modeling method, the EMTA (Eshelby-Mori-Tanaka approach) modeling approach [1], is applied to the study of SiC/SiC 2D woven composites for fusion reactor applications for the first time, to the best of our knowledge, with excellent results. We compare EMTA model results to existing thermal conductivity data for these materials and suggest that in the future this approach can be beneficial by providing us with tools to further optimize these composite materials for fusion energy applications since the EMTA method and code can address both thermal and mechanical properties with the same framework.

SUMMARY

The study, measurement, prediction, and control of thermal conductivity of SiC/SiC composites is a critical issue for Fusion. Both high conductivity (first wall) and reduced conductivity (flow channel insert) materials appear to be required for specific fusion reactor applications so that low-activation goals are achieved. This study has applied an Eshelby-Mori-Tanaka approach (EMTA) implemented in PNNL EMTA software to predict thermal conductivities of SiC/SiC composites. The EMTA homogenization procedure is structured in three steps to capture the effects of the constituent materials including the fiber-coating layer on the thermal conductivities of the as-formed composites. The results show that when perfectly bonded to the fibers a thicker fiber coating layer with higher thermal conductivity than that of the fibers leads to increased thermal conductivities for the composite. EMTA can be effectively used to identify the interfacial thermal conductance by correlating the EMTA predicted thermal conductivities with the measured values. A reverse engineering procedure in EMTA is useful to determine the thermal conductivities of the constituents if the actual measured values are not available or are unknown.

PROGRESS AND STATUS

Introduction

SiC/SiC continuous fiber composites are under consideration as structural materials for first wall or breeder blanket applications in advanced fusion power plants and advanced nuclear fission reactors. In such applications the materials in a high-temperature neutron radiation environment or non-radiation environment are subjected to a high heat flux that imposes extremely stringent requirements on the thermal conductivity of the components. These requirements must be satisfied concurrently with other thermomechanical requirements. The focus of this paper is on the prediction of the thermal conductivities of two-dimensional (2D) woven SiC/SiC and unidirectional (UD) SiC/SiC composites for fusion reactor applications. To this end, a Mori-Tanaka type model combined with the Eshelby's equivalent inclusion method has been explored to predict the thermal conductivities of these composites as a function of temperature and the constituent parameters such as thermal properties of the fiber and matrix phases, fiber volume fraction, fiber orientation, and fiber/matrix interfacial thermal conductance [2-5]. A computational tool named EMTA (Eshelby-Mori-Tanaka approach) was developed to

---

[1] PNNL is operated for the U.S. Department of Energy by Battelle Memorial Institute under Contract DE-AC06-76RLO 1830.

implement the EMTA models for the computation of thermal conductivities of fiber-reinforced composites [1].

Computational Procedures

Figure 1 provides a schematic of the multiscale computational procedure that is adopted in this paper. The computation considers the UD composite containing aligned coated fibers from which the first EMTA homogenization is performed to obtain the homogenized thermal conductivity of the fiber/coating layer system. Next, the second EMTA homogenization is carried out to determine the thermal conductivity of the UD composite containing aligned equivalent fibers and embedded in a matrix material. Finally, a fiber orientation averaging technique [6] is applied to compute the thermal conductivity of the as-formed composite having a fiber orientation distribution. The computational procedure assumes perfect bonding between the fibers, the fiber coating layer and the matrix material. Thus, it does not include explicit modeling of the physical debonding that affects the thermal conduction from the fibers and their surrounding materials. If debonding occurs, this will be accounted for by an equivalent layer with associated thermal properties. A computer code named EMTA was developed that implements the Eshelby-Mori-Tanaka approach to predict the thermoelastic properties and thermal conductivities of fiber-reinforced composites [1].

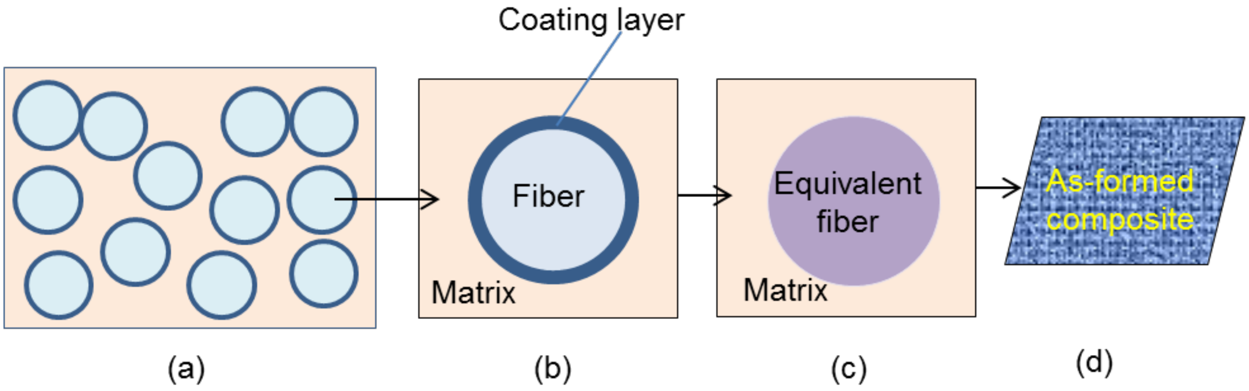

Figure 1. Schematic of the EMTA computational procedure for composite homogenization.

RESULTS

Figure 2 shows a typical computation using EMTA for the in-plane and transverse thermal conductivities of DuPont 2D woven SiC/SiC composites made using Hi-Nicalon Type-S fibers and isothermal CVI SiC matrix infiltration. The EMTA results match the measurements with excellent agreement when the matrix and fiber thermal conductivities are known but the interfacial, or coating, thermal conductivity is not known and must be determined from the experimental data via a fitting procedure. In this case, Youngblood et al. measured the matrix and fibers individually and used typical analytical models of composite conductivity for their results [7]. Here EMTA is used to duplicate this research but with the added benefit of being a robust code that can handle any composite layup and also can be used to model mechanical properties.

EMTA also has a reverse engineering feature that can be used to predict individual constituent properties given some knowledge or understanding of the other conductivities. These will be demonstrated in a separate publication.

Future work will involve 1) addition of radiation damage mechanics into EMTA so that thermal conductivity as a function of dose can be predicted and 2) demonstrating the simultaneous modeling of mechanical and thermal properties so that composite design can be integrated and tailored for specific applications in a more general and robust manner.

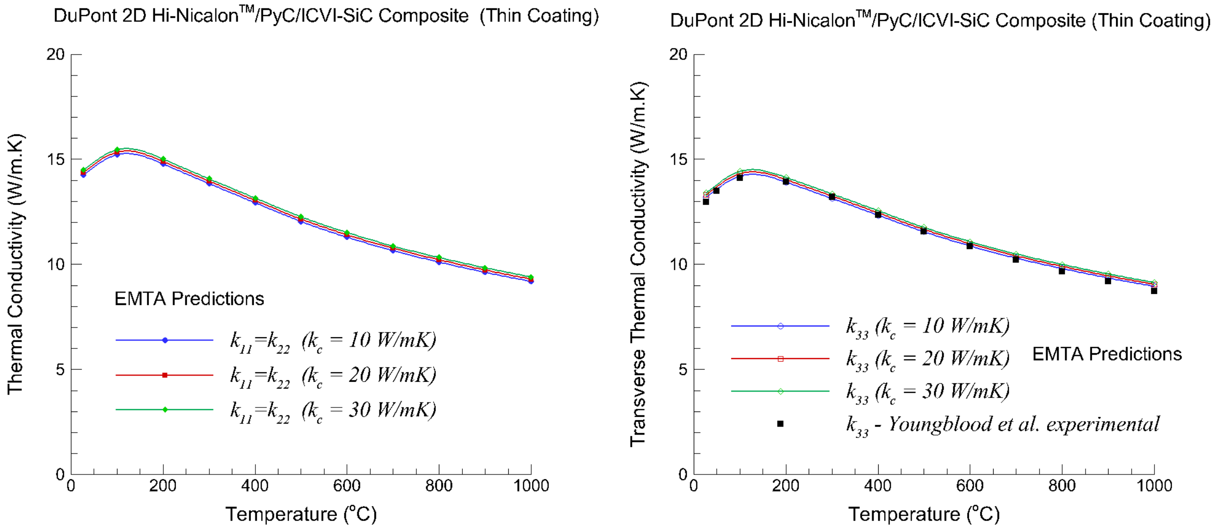

(a) (b)

Figure 2. Thermal conductivities predicted by EMTA for the DuPont 2D SiC/SiC woven composite with the thin fiber coating layer: (a) In-plane thermal conductivities, k_{11} and k_{22}, and (b) transverse thermal conductivity k_{33} compared to Youngblood et al.'s experimental results [7].

REFERENCES

1. B. N. Nguyen, EMTA User's Guide, 2010, Pacific Northwest National Laboratory: Richland, WA.
2. T. Mori and K. Tanaka, "Average stress in matrix and average elastic energy of materials with misfitting inclusions," *Acta Metall.* **21,** 5 (1973) 571-4.
3. J. D. Eshelby, "The determination of the elastic field of an ellipsoidal inclusion and related problems," *Proc. R. Soc. Lond. A* **241 (**1957) 376-396.
4. Y. Benveniste, "A new approach to the application of Mori-Tanaka's theory in composite materials," *Mech. Mate.* **6,** 2 (1987) 147-157.
5. H. Hatta and M. Taya, "Equivalent inclusion method for steady state heat conduction in composites," *Int. J. Eng. Sci.* **24,** 7 (1986) 1159-72.
6. S. G. Advani and C.L. Tucker, III, "The use of tensors to describe and predict fiber orientation in short fiber composites," *J. Rheol.* **31,** 8 (1987) 751-784.

7. G. E. Youngblood, D. J. Senor, R. H. Jones, and W. Kowbel, "Optimizing the transverse thermal conductivity of 2D-SiC_f/ SiC composites, II. experimental," *J. Nucl. Mater.* **307-311,** Pt. B (2002)1120-1125.

8.3 Nanofeature-Dislocation Associations and a Fitted Long Term Thermal Aging Pipe Diffusion Model for MA957 — Y. Wu, N. J. Cunningham, G. R. Odette and D. Klingensmith (University of California - Santa Barbara)

OBJECTIVES

The objective of this work is to determine and model the high-temperature nanofeature coarsening mechanism in nanostructured ferritic alloys.

SUMMARY

Nanostructured ferritic alloys (NFAs) have applications in advanced fission and fusion reactors and are strengthened by a high number density of Y-Ti-O nanofeatures (NFs) that are very stable up to 1000ºC [1]. Previously reported long and short-term aging studies from between 800ºC and 1400ºC on NFA MA957 for times up to 32.4 kh were used to develop a coarsening model in the form:

$$[d(t)^p - d_o^p] = [k_p(T)t] \tag{1}$$

Here t is the aging time and d is the average NF diameter starting at d_o. Simple models predict p ranging from 2 to 5, depending on the operative coarsening mechanism. Our data is most consistent with a pipe diffusion mechanism (p=5) [2]. However, a least square fit of all the data gives a higher p values of 6.26, possibly suggesting that combinations of complex phenomena operate during aging; for example, rather than random pipe diffusion processes, coarsening and other stages of NF evolution may involve highly correlated multispecies mechanisms.

In this short report we present TEM data for 1000ºC aging to 21.9 kh that provides strong support for pipe diffusion coarsening (p = 5), since most of the NFs are associated with dislocations. Additional aging studies at intermediate temperatures (1075ºC to 1200ºC) and times (<10 kh) are underway to help more accurately identify the coarsening mechanisms and kinetics.

BACKGROUND

NFAs have a unique combination of high temperature strength and radiation damage tolerance. These important attributes are primarily due to an ultrahigh density of oxide NF with average diameters in the range of 2-3 nm. Thus a critical issue is the high temperature long-term thermal and radiation stability of the NFs and the balance of the NFA microstructures. We have previously reported long-term thermal aging (LTTA) studies of NFA MA957 to derive fits by semi-empirical models of the coarsening kinetics [2]. All fitted models predicted that the NFs are stable up to 900ºC for long times (>10^5 h). The data are most consistent with a pipe diffusion mechanism (p = 5), although the best statistical fit yields p = 6.26. Here we propose a new coarsening concept that yields a p = 6.

STATUS AND PROGRESS

Equation 1 can be expressed as:

$$[d(t)^p - d_o^p] = k_{po}[\exp(-Q_p/RT)]t \tag{2}$$

This equation was non-linear least square fit (LSF) to all the data between 950 and 1400°C simultaneously. Here, Q_p is the activation energy for coarsening, R is the universal gas constant, T is the aging temperature, and k_{po}, p, (and Q_p) are fitting parameters. Alternately, Equation 1 was fit at individual aging temperatures with imposed model based p values of 3 (lattice diffusion) and 5 (pipe diffusion) to derive corresponding $k_{3/5}(T)$. Plots of $\ln[k_{3/5}]$ versus 1/T were fit to obtain the corresponding $Q_{3/5}$. The fitting results, reported previously, are summarized in Table 1 [2].The simultaneous data fitting yielded a p = 6.26 and a corresponding Q_p = 764±46 kJ/mole, with a standard deviation (SD) in the predicted versus measured [d - d_o] of 0.63 nm. Fixing p gave the overall predicted versus measured [d - d_o] SD of 1.07 and 0.67 nm for p = 3 and 5, respectively. The difference between the two fixed order kinetics models is statistically significant and sufficient to eliminate the p = 3 case. However, the differences in the fits p = 5 and 6.26 models are not statistically significant, and both strongly support a pipe diffusion related mechanism. For p = 5, Q_5 = 673±12 kJ/mole.

Table 1. Fit Q_p ,k_p and SD of the measured versus predicted [d - d_o] for various p.

Order of Aging Kinetics	p = 6.26	p=3	p=5
Q_p (kJ/mole)	764±46	554±11	673±12
k_p or k_{po} $(nm/h)^p$	7.3×10^{29}	6.0×10^{19}	4.4×10^{25}
Pred. vs. meas. SD [d - d_o] nm	0.63	1.07	0.67

We can further analyze the results as follows. As shown elsewhere, the NFs in MA957 are primarily a pyroclore-type $Y_2Ti_2O_7$ complex oxide [3]. Thus for near-equilibrium conditions, the matrix solubility of Y, X_y, would be controlled by this phase and the matrix Ti and O activities. Assuming O is in equilibrium with Cr-oxide and Ti is in equilibrium with a metallic reference state, $X_m \approx 10^{-25}$ [4]; that is, the solubility of Y is extremely low. Indeed this is the case under almost any set of plausible thermodynamic assumptions. Thus Y dissolution from the $Y_2Ti_2O_7$ oxide is expected to be the rate controlling mechanism. For purposes of comparison, assuming lattice diffusion controlled kinetics (p = 3), the NF coarsening rate is given by

$$[d(t)^3 - d_o^3]/t] = k_3 \approx [7\gamma V D_y X_y/RT] \text{ [nm/h]} \qquad (3)$$

D_y is the matrix diffusion coefficient, γ is the NF-matrix interface energy, and V is the molar volume, taken as that for Fe. At 1000°C, D_y is experimentally estimated to be $\approx 8 \times 10^{-16}$ m^2/s. Taking nominal values of $\gamma = 2$ J/m^2, $V = 7 \times 10^{-6}$ m^3/mole and $X_y = 10^{-25}$, yields a predicted coarsening rate of $[d(t)^3 - d_o^3]/t]^{1/3} \approx 1.4 \times 10^{-6}$ $nm/h^{1/3}$, compared to the measured value of 1.1×10^{-3} $nm/h^{1/3}$. A first principles diffusion model predicts $D_y = 9 \times 10^{-16}$ at 1000°C with an activation energy of $Q_{md} \approx 218$ kJ/mole [5]. The $X_y = 10^{-25}$ represents an effective Y dissolution energy of $Q_{ys} \approx 609$ kJ/mole. Thus the overall activation energy for matrix diffusion NF coarsening is ≈ 827 kJ/mole, which is substantially higher than for the p = 3 model fit of 555 kJ/mole. Clearly the lattice Y dissolution-diffusion mechanism is not consistent with the observed NF coarsening rates.

The data is better fit by a dislocation pipe diffusion model (p = 5), which is also qualitatively consistent with a much higher value of the product of the Y diffusion coefficient and solubility at a dislocation, D_dX_d. The TEM micrographs in Figure 1a and b for 1000°C-21.9 kh aged MA957 provide strong support for the dominant role of dislocations in coarsening, since most of the NFs are seen to be associated with dislocations.

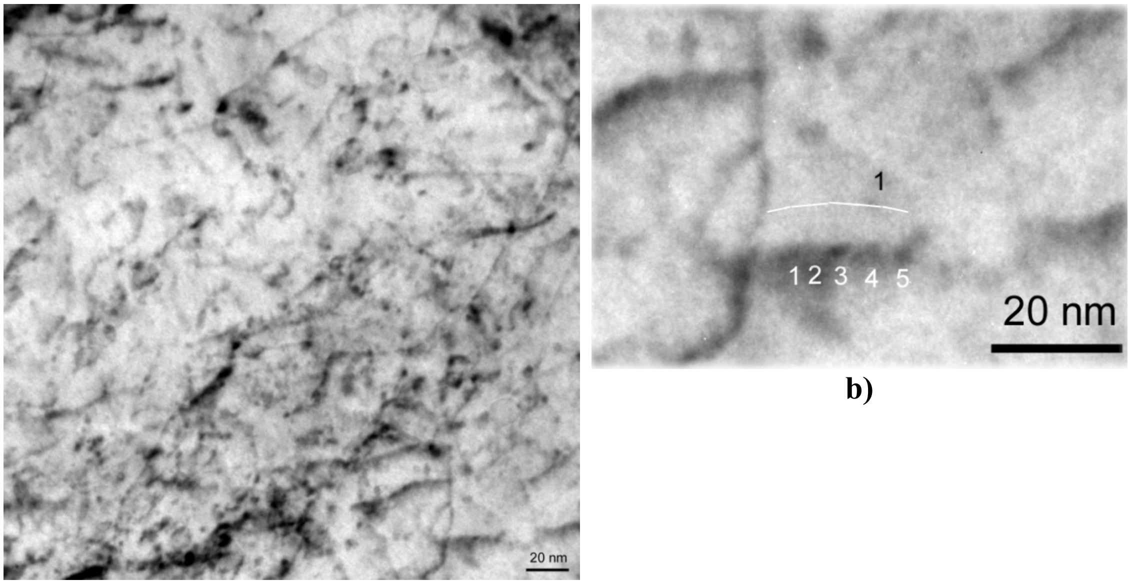

a) **b)**

Figure 1. TEM micrographs showing high concentration of NF on dislocations.

In the case of NF coarsening by dislocation pipe diffusion,

$$[d(t)^5 - d_o^5]/t]^{1/5} = k_5^{1/5} = [C_oA\gamma VD_{yd}X_{yd}/RT]^{1/5} \qquad (4)$$

Here, C_o (≈ 0.1) is the product of a constant times a factor that depends of the volume fraction of the coarsening feature and A (≈ $4b^2$, where b is the Burger's vector) is the cross section area for pipe diffusion [6]. The measured activation energy of 673 kJ/mole can be used to estimate the $D_{yd}X_{yd}$ product at dislocations using a nominal pre-exponential D_{od} of 10^{-6} m^2/s, $D_{yd}X_{yd} \approx 10^{-6}\exp(-673{,}000/RT)$ or 2.4×10^{-34} m^2/s at 1000°C. The resulting predicted coarsening rate of 1.65×10^{-3} $nm/h^{1/5}$ is 51.5 times lower compared to the measured rate of 0.085 $nm/h.^{1/5}$ Note that the ratio of the fitted pipe diffusion to the estimated matrix coarsening activation energies 673/827 kJ/mole ≈ 0.81 is not unreasonable, and might be expected to be even lower. However, even a rollup of upper bound uncertainties in the temperature insensitive parameters $C_oA\gamma VD_{od}$ in Eq. 4, is probably not sufficient to quantitatively account for the difference between the predicted and measured coarsening rates. But the simple p = 5 pipe diffusion model is certainly qualitatively better than that for p = 3. Figure 4 plots the predicted time needed to double $d_{o,}$ t_2, as a function of temperature evaluated as:

$$t_2 = 31d_o^5/k_5(T) \qquad (5)$$

Here the $k_5(T)$ are the fit values so these results demonstrate the excellent fit by the model over a wide range of temperature.

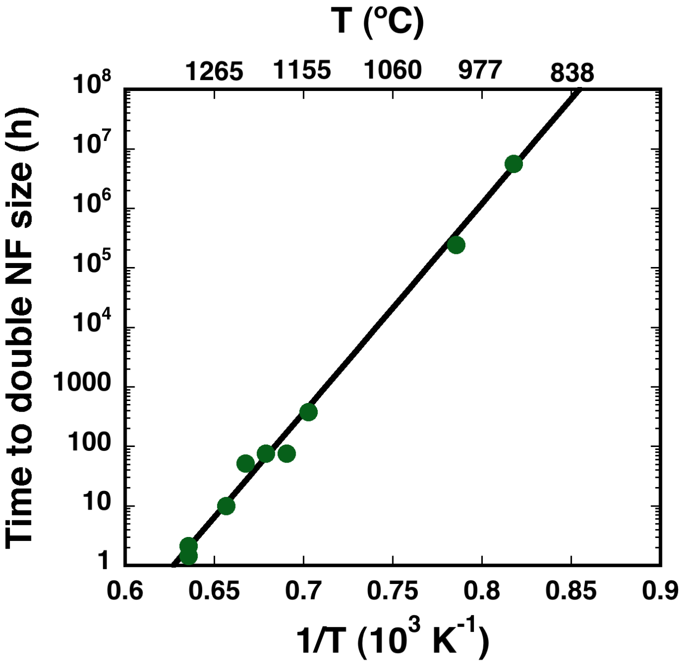

Figure 4. Predicted times to double d_o as a function of T based on the P = 5 pipe diffusion model.

The best empirical fit to the coarsening data was p = 6.26, with an activation energy of 764 kJ/mole. Conceptually this dimensionality could be associated with a p ≈ 6 model that involves pipe diffusion combined with detachment and climb of dislocations, which then intersect a new set of previously isolated NFs. It is postulated that the increase in p from 5 to ≈ 6 could be associated with a detachment stress controlled by NF spacing on a dislocation line, Λ, and a non-dimensional factor h, relating Λ to the detachment mechanism. The resulting kinetics can be dimensionally represented by

$$[d(t)^6 - d_o^6]/t]^{1/6} = k_6^{1/6} = [C_oA\gamma V\eta\Lambda D_dX_d/RT]^{1/6} \qquad (6)$$

Additional TEM studies would be needed to test and parameterize p = 6 model. However, it is not clear that this would lead to full quantitative agreement as the actual coarsening mechanisms are likely to be even more complex. For example, rather than random pipe diffusion processes, coarsening and other stages of NF evolution may involve highly correlated multispecies mechanisms.

The failure of simple models to predict quantitatively the observed coarsening rates may suggest the need for new ways of thinking about far from equilibrium material states, where classical near equilibrium concepts no longer apply. In this case the pre-precipitated NFA-NF system has been pushed to the ultrahigh free energy state by what can be considered the mechanical work of alloying. The free energy reduction during the initial precipitation is also very large, so that the system is effectively trapped and *almost* frozen in a metastable state. However, the free energy still decreases slowly by complex processes that do not normally operate for near-equilibrium conditions.

FUTURE WORK

LTTA studies are under way that will be used to observe coarsening at intermediate time and temperature spanning the previous studies. Table 2 show predicted average NF d after aging at 1075°C and 1200°C for up to 4000 h for different p values. The aged alloys will be examined after 500, 1000, 2000, and 4000 h using SANS, TEM, and APT. The 1075°C aging will add valuable data points between the previous long term thermal aging at and below 1000°C and the shorter term aging above 1200°C. A careful examination of medium term aging at 1200°C should reveal the coarsening mechanism at play. Note, significant differences between the p values are not apparent until after 1000 h.

Table 2. Predicted d after 500, 1000, 2000, and 4000 h at 1075 and 1200°C for p = 3, 5, and 6.26.

d_o = 2.68 nm	d (nm) at 1075/1200°C			
t (h)	500	1000	2000	4000
p = 3	3.57/8.98	4.15/11.27	4.98/14.16	6.12/17.83
p = 5	3.71/7.98	4.18/9.09	4.7410.44	5.42/11.99
p = 6.26	3.70/7.47	4.09/8.35	4.54/9.33	5.06/10.42

REFERENCES

1. G. R. Odette, M. J. Alinger, and B. D. Wirth, *Annu. Rev. Mater. Res.* **38** (2008) 472.
2. N. J. Cunningham, M. J. Alinger, G. R. Odette, and D. Klingensmith, "On Nanofeature Coarsening Kinetics in MA957: Fitted Lattice and Dislocation Pipe Diffusion Models," Fusion Materials Semiannual Progress Report for period ending June 30, 2012, 116-121, DOE-ER-0313/52.
3. Y. Wu, E. M. Haney, N. J. Cunningham, and G. R. Odette, *Acta Mater.* **60** (2012) 3456-3468.
4. L. Barnard and D. Morgan, Personal communication.
5. D. Murali, B. K. Panigrahi, M. C. Valsakumar, and C. S. Sundar, *J. Nucl. Mater.* **419** (2011) 208-212.
6. A. J. Ardell, *Acta Metall.* **20** (1972) 601-609.

9.1 Fusion Material Irradiation Test Facility (FMITS) at SNS — M. W. Wendel and P. D. Ferguson (Oak Ridge National Laboratory)

OBJECTIVE

The objective of this work is to investigate building an irradiation facility for fusion materials at the Spallation Neutron Source (SNS). The Fusion Materials Irradiation Test Station (FMITS) is a design concept (completed in FY 2012) for installation at the SNS. The design study showed that the first SNS high-energy irradiations on fusion materials specimens could occur in less than 3 years from project start at a cost of $10M. The project is currently unfunded.

SUMMARY

The impact of He and H transmutation products on material damage from 14.1 MeV neutrons is a critical unresolved issue which is being addressed by combining numerical models and specialized ion and neutron irradiation experiments. Because of the uncertainties associated with both modeling and ion irradiation experiments, there is a clear need for an accessible irradiation facility that can provide near prototypic levels of transmuted helium and hydrogen. The scientific understanding obtained would also enable more effective use of a future large-volume fusion engineering irradiation facility (such as IFMIF) when it becomes available.

A design study [1,2,3] for a fusion materials irradiation test station (FMITS) for installation at the Spallation Neutron Source (SNS) has been completed. Samples would be located within two horizontal tubes in front of the mercury target. For these specimen locations, the back-scattering neutron flux spectra should be close to the ITER fusion spectrum. The PKA spectra at the FMITS samples were also compared to those for ITER, and the results show good agreement. Material damage rates would be 1.6–5.5 dpa/yr for steel, and 1.8–3.4 dpa/yr for SiC.

PROGRESS AND STATUS

Introduction

Computational modeling and experimental studies provide compelling evidence that displacement damage formation induced by fission neutrons and the 14.1 MeV neutrons representative of D-T fusion are quite similar [4,5]. These data largely validate the use of fission reactor experiments to explore the basic radiation stability and radiation-induced microstructural and mechanical property changes of candidate fusion reactor materials. However, helium and hydrogen production levels due to nuclear transmutation reactions are significantly higher, ~a factor of 10 to 100, with a DT neutron energy spectrum than with a fission neutron spectrum. The ratio of helium or hydrogen production to displacement damage production, e.g. He/dpa ratio, is a convenient parameter for characterizing irradiation environments. The impact of these gaseous transmutation products remains a critical unresolved issue for the use of fission reactor data in the design of future fusion reactors. The interaction of helium with both vacancy and interstitial type defects [5] may have substantial implications for radiation damage accumulation at high doses. High helium levels can lead to accelerated cavity growth on grain boundaries, which can significantly reduce creep life and fracture resistance at elevated temperatures [7].

A combination of modeling and specialized ion and neutron irradiation experiments have been and are being used to explore the sensitivity of materials to irradiation at different He/dpa ratios

[7]. In addition, experiments have been conducted using a spallation neutron source in Switzerland [8,9]. For the current fusion prime candidate ferritic-martensitic steels containing 8 to 14% Cr, some of this data suggests a strong effect of helium on fracture properties when the total helium reaches a few 100 appm [9] which would be reached in about 20 dpa in steel in a DT fusion reactor. This is much lower than the desired target dose of >100 dpa. Although ion irradiations can explore a range of He/dpa ratios, they have significant limitations: (1) only a thin region of the sample (up to a few micrometers) is irradiated, and (2) the damage rate is about 100 to 1000 times higher than DT fusion reactor irradiation. The thin irradiated region does provide microstructural information, but mechanical property information is limited to very low-load hardness measurements. The effects of high dose rate can be investigated by computational modeling, but all such modeling is also limited by the use of uncertain parameter values and is subject to our current understanding of the mechanisms by which helium and hydrogen interact with the other radiation-induced defects.

Because of the uncertainties associated with both modeling and ion irradiation experiments, there is a clear need for an accessible irradiation facility, such as that proposed here for the Spallation Neutron Source (SNS) accelerator, that can provide near prototypic levels of helium and hydrogen for screening candidate fusion materials. For the Fusion Materials Irradiation Test Station (FMITS) a modest range of He/dpa ratios would be accessible to help calibrate and verify the modeling studies. In Fig. 1, the 2-4 year irradiation at SNS running at 1 and 1.4 MW is compared with data from other facilities (Rotating Target Neutron Source, RTNS; Material Test Station, MTS; International Fusion Materials Irradiation Facility, IFMIF). An SNS facility would provide the opportunity for the US program to take the scientific lead in this critical area of fusion structural materials development. The scientific understanding obtained would enable more effective use of a future large volume fusion engineering irradiation facility when it becomes available. By exploiting the understanding gained from low-to-intermediate dose data and from modeling, the US program could optimize material choices for use in future machines. More fundamental experiments could be employed in concert with fission reactor data and modeling to confirm the expectation that the high-energy tail in the neutron energy spectrum has only limited impact on material properties.

System Design and Key Performance Measures

An initial set of requirements was established for the design study representing the optimal use of the existing SNS configuration, operating at 1 or 1.4 MW and 1 GeV proton energy, to benefit fusion materials irradiation while minimizing the impact on the main mission of neutron science. The performance described here complies with those requirements.

The primary goals for irradiation at the sample locations (based on iron samples) are for up to 5 dpa/year, 10–80 appm-He/dpa ratio, and less than 150 W/cc thermal power dissipated within the sample. Two sample regions would be provided, typically of a size 12-mm-diam by 175-mm-long which has proven useful for metallurgical test specimens irradiated at the High Flux Isotope Reactor (HFIR) [11]. The sample environment control will use similar methods developed for HFIR with temperature ranges from 25–600°C, and 50°C temperature temporal and spatial uniformity required on any given sample.

Instrumentation would be based on the instrumentation in HFIR irradiation capsule designs to be compatible with the SNS EPICS control/data acquisition system with up to five

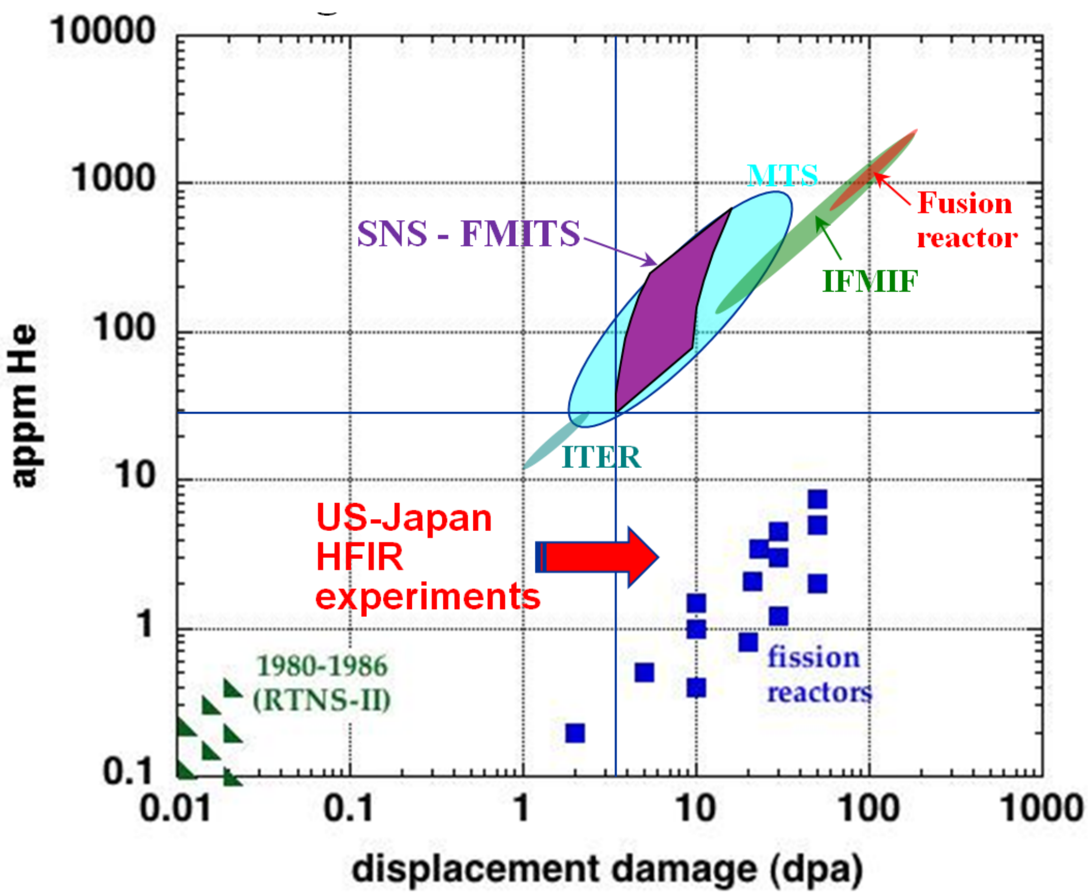

FIG. 1. Comparison of 2-4 year helium and displacement damage levels for ferritic steels for candidate irradiation facilities (adapted from [10]).

thermocouples in each of the two sample regions. Temperature would be thermocouples in each of the two sample regions. Temperature would be controlled by thermocouples in each of the two sample regions. Temperature would be controlled by varying the gas composition (thermal conductivity) in a precisely specified gap between the constant-temperature sample region and the water-cooled heat sink. The design would allow for unmanned operation with machine failure protection and no impact to the safety and reliability of the SNS facility. A comprehensive failure mode overview shows that the Credited Engineering Controls (CECs) or safety basis for SNS would not be impacted.

The FMITS assemblies would be compatible with existing SNS Target Service Bay remote handling equipment and systems and amenable after irradiation for reuse, sample extraction and waste disposal. Multiple irradiation periods on consecutive targets would be possible in order to increase exposure on a given sample arrangement. An option for quick removal of the irradiation system from the target would be available in case of failure. Normal target replacement downtime would not be extended due to the FMITS installation/replacement operations. The initial installation of the FMITS hardware including replacement shield block and gas utilities would not require any shutdown period beyond the normal bi-annual scheduled SNS outages.

This study also provides options for sample extraction from the irradiated FMITS assembly, which depend on the time available for the extraction at SNS. The most expedient option would likely be selected in a conceptual design, keeping the samples within their stainless steel coolant tubes for shipment and extraction offsite. The sample sections would be shear cut and placed into a 110-gallon drum with lead shielding. A suitable drum is already available at SNS and has been used for removing post-irradiated stainless steel target samples.

Experimental Design

FMITS sample regions are contained within a harness that wraps around the existing SNS target as shown in Fig. 2. The two sample regions may be located in different irradiation zones depending on their offset from the proton beam centerline which could vary from 2 to 5 cm. Figure 3 shows the contents of the FMITS tubes in detail. The test specimens would be spring-loaded into holders that would be stacked within an inner stainless steel tube, which would then be welded into the assembly. This inner tube would be flooded with inert gas mixture to control the temperature by varying the mixture thermal conductivity. Cooling water would flow from the target water shroud through the annulus between the inner and outer FMITS tubes. The thermocouples would be threaded down the centerline through the specimen holders and terminated within the holder test zones.

The water shroud that surrounds the mercury target module would be modified to accommodate the FMITS inlet and outlet tubing that is routed through the target/core-vessel seal (circular ring in Fig. 2). The modified shroud is necessary because of the tight fit of the shroud rear section (shown in grey in Fig. 2) to the outer reflector assembly. All of the FMITS hardware shown in Fig. 2 is removable and reusable on subsequent targets if required.

The supply of the two inert gas constituents for each of the two capsule regions is provided by the four connections on the backside of the target seal (Fig 2). The gas supply and control system would be located in a basement room and piped in through existing ports in the target process bay which are currently unused. Only two exhaust lines are necessary since the gases are mixed just upstream of the capsules. The irradiated exhaust gases would be discharged into the process bay air, which is controlled and released out of the stack. It is possible that a delay tank would be necessary before releasing the gases into the process bay. The cooling water would be pulled from the existing target shroud coolant system (a 10% effect) and monitored with a flow sensor on the backside of the target seal.

At FMITS, the back-scattering neutron flux spectra from the mercury target closely resemble the ITER fusion spectrum as shown in Fig. 4. The agreement is limited to neutron energies less than 10 MeV, and the ITER spectrum spikes at 14.2 MeV before abruptly ending at 15.7 MeV. The neutron flux in the FMITS spectrum, however, continues to decline with the increasing neutron energy unto the incident proton energy 1 GeV. The neutron flux spectrum at 3 cm off the centerline at FMITS shows higher neutron fluxes for neutron E > 10 MeV than that at 5 cm due to the higher incident proton flux at that location. The PKA spectra at the FMITS samples also show good agreement with those at ITER.

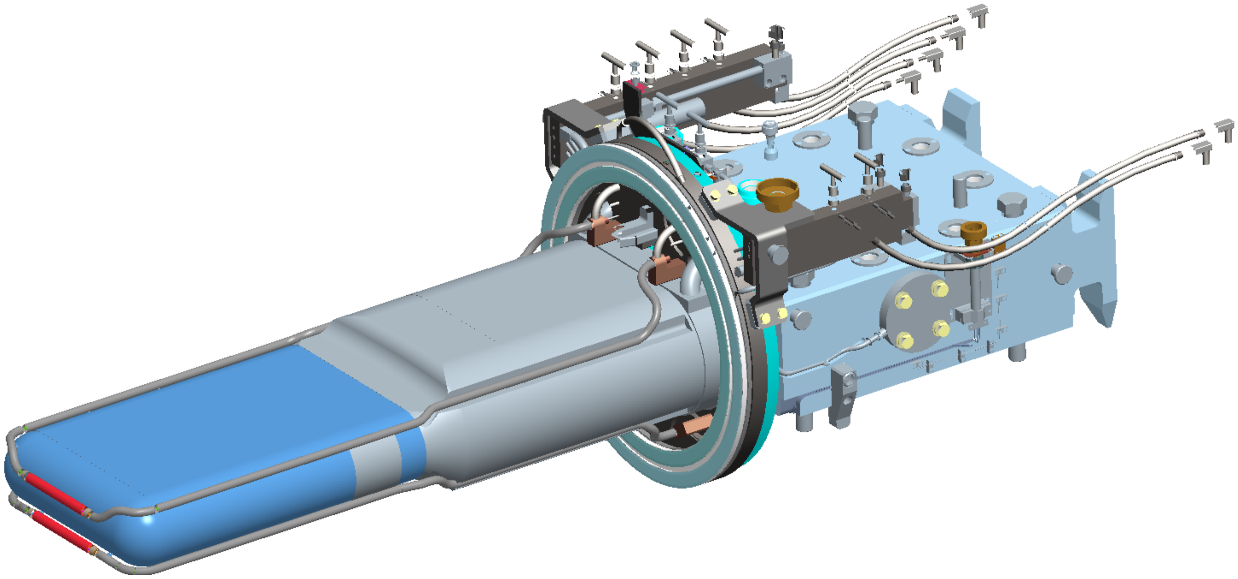

FIG. 2. FMITS assembly installed onto an SNS target module.

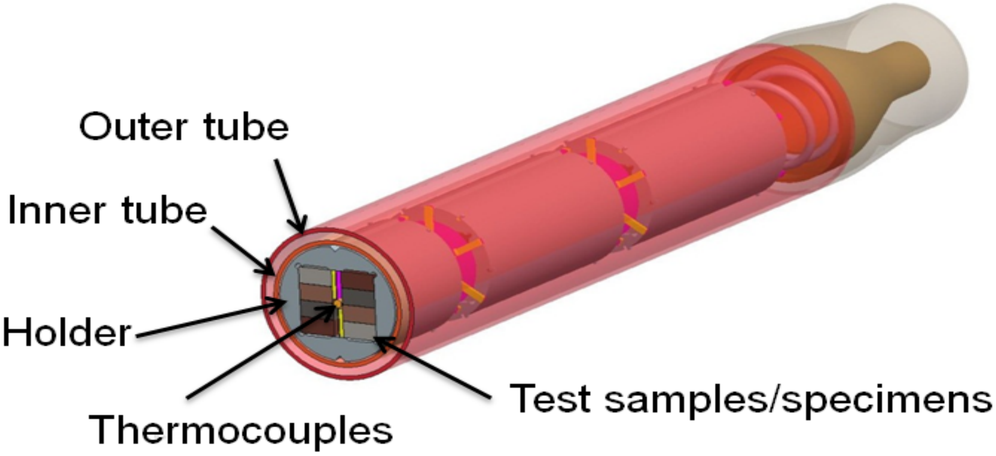

FIG. 3. FMITS test section containing irradiation material samples.

Neutronics Analysis

The FMITS peak displacement production rate is 5.5 dpa/yr for steel and 3.4 dpa/yr for SiC, where the neutron contribution is 58% and 90% for steel and SiC, respectively. Figure 5 shows that the peak helium production rate is 409 appm/yr for steel (7.5% neutron contribution) and 334 appm/yr for SiC (31% neutron contribution). The peak hydrogen production rate is 1700 appm/yr for steel (12% neutron contribution) and 492 appm/yr for SiC (18% neutron contribution). In a spallation spectrum the helium/displacement or hydrogen/displacement production ratio exhibits a very wide range. For the majority of the sample locations, the helium/displacement production ratio in steel is 75 and 20 appmHe/dpa for vertical offsets from the target centerline of 3 cm and 5 cm, respectively. The same numbers are 98 and 37 appmHe/dpa for SiC samples at 3 cm and 5 cm offsets.

The neutron contribution to a certain radiation damage production (displacement, helium or hydrogen) depends on the incident neutron and proton flux spectra and its production cross sections for a certain material. Generally, the neutron contribution is lower at the sample rod closer to the target centerline, where it is bombarded with more intensive proton fluxes. The neutron contribution is generally lower in steel than in SiC.

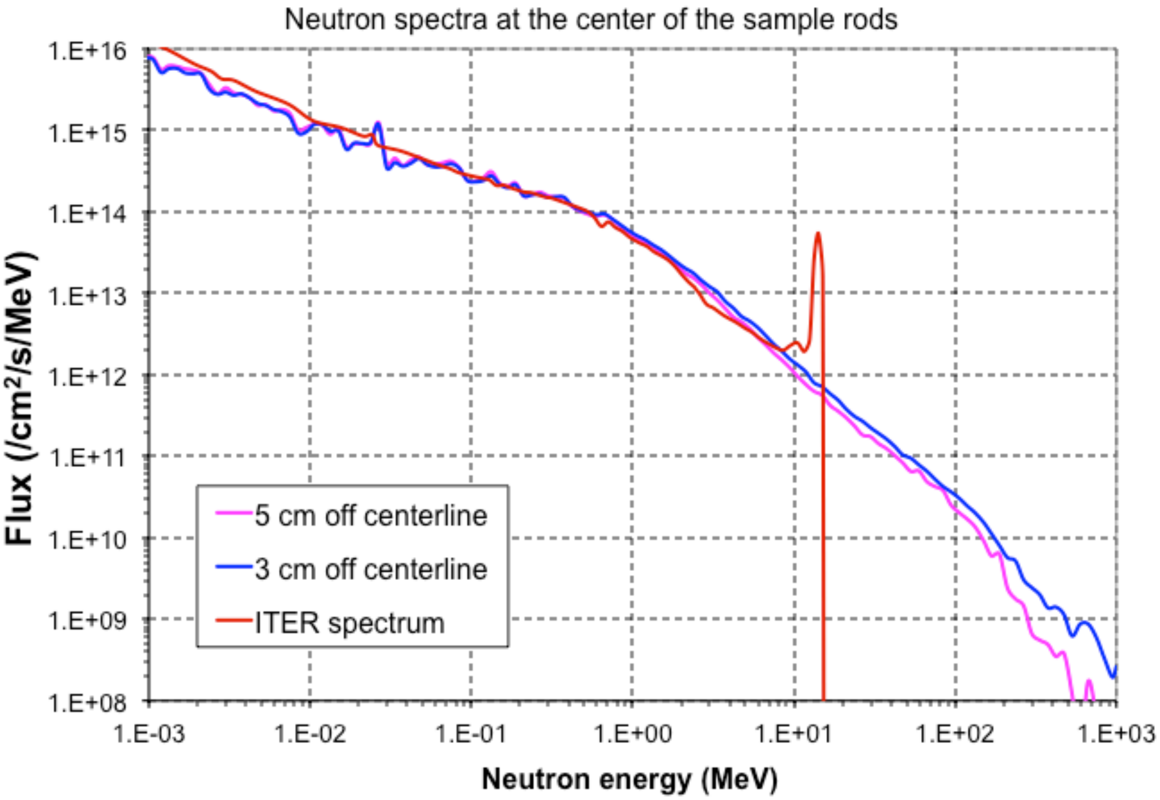

FIG. 4. Comparison of neutron flux spectra for FMITS and ITER.

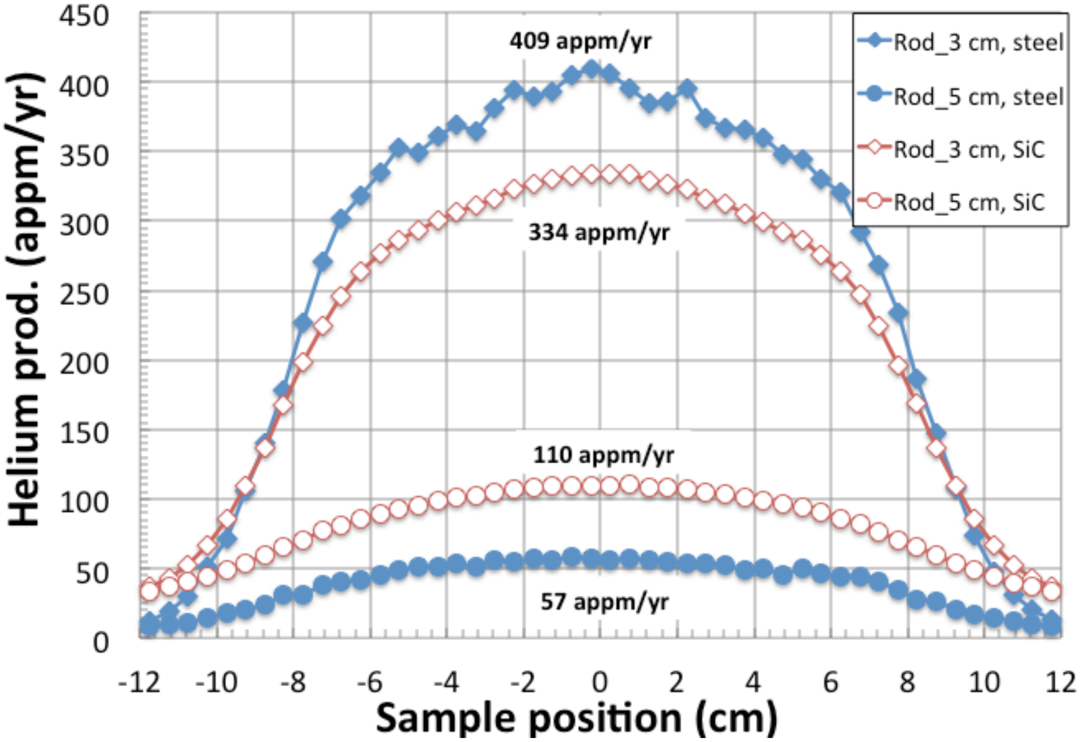

FIG. 5. Helium production rates for steel and SiC samples at FMITS at a nominal beam power of 1.4 MW at SNS.

Safety, Off-normals, and Potential Impacts on SNS Mission

A comprehensive evaluation (including some engineering analysis) of off-normal events was performed. The hazard analysis in the SNS safety documentation was also revisited, and no major problems were identified. Hypothetical hazards in the FMITS system were categorized as: (1) water system hardware failures, (2) gas system hardware failures, and (3) remote handling mishaps. A quantified risk assessment remains to be done in the final design phase.

Based on comments made by the FMITS Design Study Review Committee, The Accelerator Advisory Committee, and discussions with key staff in the ORNL Fusion Materials Program and at SNS, the potential impacts to SNS/ORNL operations can be summarized as follows:

1. An unscheduled target replacement will be prolonged by as much as 4 days.

2. Possible 1-2 weeks down time will be required to remove FMITS following potential unanticipated hardware malfunctions.

3. There exists an incremental increase in the frequency of remote handling equipment failures and human errors due to increased operational load.

4. Rare events may occur that can be imagined but cannot yet be excluded.

It is expected that as the actual design proceeds, the potential for these impacts will be significantly reduced or eliminated altogether. In order to minimize potential operational outages due to the presence of FMITS, the following precautions have been included in the proposed cost/schedule:

1. A remote handling mockup of FMITS with be used for procedural development and technician training.

2. Improvements will be made to the design concepts of FMITS to reduce the installation time, such as quick-disconnect fittings.

3. Contingency strategies will be developed for given scenarios such as choosing not to reinstall FMITS during an unscheduled outage, or in a scheduled outage if some sensors have already failed.

4. The sensors and connections will be qualified to 100% compliance criteria immediately prior to installation of FMITS.

Costs and Schedule

The total estimated one-time cost for the test facility is $6.7 million, nearly equally divided between labor and materials. Because the design is still at a conceptual level and vendor quotes have not been obtained, a 50% contingency was applied, giving a total estimated project cost of $10 M.

Design time and hardware costs were estimated at the component level and by project phase. The costs for remote handling were based on the experience over the last 5 years of SNS remote handling operations, including 5 target and 2 proton beam window replacements. The target modules are relatively expensive and it is assumed that the FMITS project would pay for the changes to the target module required to attach the FMITS assembly.

The schedule is for 30-months of design, fabrication, and installation, but could be prolonged if funding is provided at a slower rate. The plan requires 18 months of design and a midway review before procurement begins. In parallel with the design work, mockup testing for hydraulic performance and remote handling would be necessary. The 14-month target fabrication is on the critical path for the FMITS schedule, so an early release to begin the target fabrication is very beneficial.

It is possible to complete all of the installation work without affecting the SNS beam-time operational plan. The FMITS assembly would be installed with its utilities and connections during a normal 6-week shutdown. Waste disposal from the installation would occur during beam operations. Installation of the gas system in the basement of the target building is accomplished ahead of time while neutron production is occurring. The existing remote handling staff would be utilized to perform all operations within the target process bay.

A preliminary estimate is also provided for the cost of performing a specific irradiation experiment at the new FMITS facility. For a given experiment there is a cost for fabrication, installation and irradiation of the experimental hardware on a single target module. There is an additional, incremental cost for the assembly use with subsequent targets. The total for the first irradiation is $850K including 25% contingency. For each following target cycle the cost is $127K including 25% contingency.

CONCLUSIONS

Sufficient design work has been completed in this study to give the design team confidence that FMITS can be operational within $10M and as little as 30 months. Subsequently, each FMITS experiment would cost $850K to be used at the new facility. Findings from a Design Review Committee corroborate this conclusion. Design, fabrication, installation and operation all appear to be within known capabilities. No “showstopper” safety issues have been identified. The similarity to HFIR irradiation experiments and conditions allows much of the expertise developed there to be incorporated at SNS. The proposed design has no significant impact on the neutronic performance of the moderators, and therefore should not affect the quality of the neutron science. Installation activities can be accomplished without any additional shutdown periods beyond normal schedule plans.

REFERENCES

[1] A. Abdou, R. Battle, M. Dayton, D. Freeman, W. Lu, T. McManamy, P. Rosenblad, R. Stoller, and M. Wendel, SNS Fusion Materials Irradiation Test Station (FMITS) Design Study, December 30, 2011, SNS-NFDD-ENG-TD-0003-R00, Oak Ridge National Laboratory.

[2] M. Wendel, M. Dayton, W. Lu, T. McManamy, P. Rosenblad, and R. E. Stoller, IAEA 2012 Fusion Energy Conference, FTP/P1-27, October 8-12, San Diego, CA.

[3] W. Lu, T. J. McManamy, P. D. Ferguson, and F. X. Gallmeier, 11th International Workshop on Spallation Materials Technology (IWSMT-11), Gent, Belgium, Nov. 5-9 2012.

[4] R. E. Stoller and L. R. Greenwood, *J. Nucl. Mater.* **271–272** (1999) 57–62.

[5] A. Horsewell, B. N. Singh, S. Proennecke, W. F. Sommer and H. L. Heinisch, *J. Nucl. Mater.* **179–181** (1991) 924–927.

[6] D. M. Stewart, Yu. N. Osetskiy, and R. E. Stoller, *J. Nucl. Mater.* **417** (2011) 1110–1114.

[7] D. N. Braski, H. Schroeder, and H. Ullmaier, *J. Nucl. Mater.* **83** (1979) 265–277.

[8] G. R. Odette and D. T. Hoelzer, *JOM* **62** (2010) 84–92.

[9] P. Spaetig, R. Stoenescu, P. Mueller Pablo, G. R. Odette, and D. Gragg, *J. Nucl. Mater.* **386–388** (2009) 245–248.
[10] T. Yamamoto, G. R. Odette, H. Kishimoto, J-W. Rensman, and P. Miao, *J. Nucl. Mater.* **356** (2006) 27–49.
[11] FESAC Panel Report on Materials Science Opportunities, DOE/SC-0149, (2012) 69.
[12] A. Hishinuma and S. Jitsukawa, *J. Nucl. Mater.* **169** (1989) 241–248.

9.2 HFIR Irradiation Experiments — Y. Katoh, J. K. McDuffee (Oak Ridge National Laboratory)

Summary of Recent, Current and Planned Fusion Materials Program Experiments

Experiment Designation	Primary Materials	Specimen Types*	Irradiation Temperature (°C)	Max Exposure (dpa)	Number of Reactor Cycles	Irradiation Period (month/year)		
Beryllium reflector (RB) irradiation positions								
RB-15J	F82H	T, F, FT	300, 400	6	10	6/08	–	12/09
Target zone full-length capsules								
JP-25	F82H	T, FT	300, 500	20	10	2/99	–	1/01
JP-26	F82H	T, FT	300,400,500	9	5	12/03	–	11/04
JP-27	F82H	T, FT	300, 400	21	13	12/03	–	1/08
JP-28	F82H	T, FT	300,400,500	80	~50	4/05	–	
JP-29	F82H	T, FT	300,400,500	80	~50	1/05	–	
12-DCT	F82H	DCT	50	1.6	1	8/11	–	8/11
JP-30	F82H	T, FT	300,400,650	20	~10	11/11	–	
JP-31	F82H	T, FT	300,400,650	20	~10	11/11	–	
Target zone rabbit capsules (DOE-JAEA)								
F8A1	F82H	T, FT	300	50	28	2/09	–	
F8A2	“	“	“	“	“	“	–	
F8B1	“	“	“	“	“	“	–	
F8B2	“	“	“	“	“	“	–	
JCR-1	SiC/SiC	Bend bars	800	30	15	10/04	–	1/09
JCR-2	“	“	“	“	“	“	–	“
JCR-3	“	“	“	“	“	“	–	“
JCR-4	“	“	“	“	“	“	–	“
JCR-5	“	“	“	>50	>25	10/04	–	
JCR-6	“	“	“	“	“	“	–	
JCR-7	“	“	“	“	“	“	–	
JCR-8	“	“	“	“	“	“	–	
JCR-9	“	“	500	30	15	10/04	–	1/09
JCR-10	“	“	“	“	“	“	–	“
JCR-11	“	“	“	“	“	“	–	“
JCR-12	“	“	“	“	“	“	–	“
F11A3	F82H	T, FT	300	20	12	5/11	–	
F11A4	“	“	“	“	“	“	–	
F11B3	“	“	“	“	“	“	–	
M4-TEN	F82H	DCT	50	1.6	1	8/11	–	8/11

Target zone rabbit capsules (TITAN)								
T8A1	SiC	BSR	300	0.01	HT**	10/09	–	10/09
T8A2	SiC	BSR	300	0.1	HT	10/09	–	10/09
T8B1	SiC	BSR	500	0.01	HT	10/09	–	10/09
T8B2	SiC	BSR	500	0.1	HT	10/09	–	10/09
T8C1	SiC	BSR	500	~1	1	5/09	–	6/09
T8D1	SiC	BSR	800	0.1	HT	3/11	–	10/09
T8E1	SiC	BSR	800	~1	1	8/09	–	8/09
T8F1	SiC	BSR	1200	~1	1	8/09	–	8/09
T9A1	W, Ni	Discs	90	0.1	HT	1/09	–	10/09
T9A2	W, Ni	Discs	90	1.2	1	1/09	–	1/09
T9C1	Steels	T, MC	500	5.5	3	11/09	–	2/10
T9C2	Steels	T, MC	500	9.6	5	11/09	–	6/10
T9G1	Steels	T, MC	300	1.2	1	6/09	–	8/09
T9G2	Steels	T, MC	300	9.6	8	6/09	–	8/11
MTTN01	Steels	T, MC	300	4.8	4	1/12	–	
300-LD-1	Steels	SSJ, MC	300	2	1	5/12	–	6/12
300-HD-1	Steels	SSJ, MC	300	12	6	5/12	–	
500-LD-1	Steels	SSJ, MC	500	2	1	5/12	–	6/12
500-HD-1	Steels	SSJ, MC	500	12	6	5/12	–	
500-HD-2	Steels	SSJ, MC	500	12	6	5/12	–	
500-HD-3	Steels	SSJ, MC	500	12	6	5/12	–	
650-LD-1	Steels	SSJ, MC	650	2	1	5/12	–	6/12
650-LD-2	Steels	SSJ, MC	650	2	1	5/12	–	6/12
650-HD-1	Steels	SSJ, MC	650	12	6	5/12	–	
650-HD-2	Steels	SSJ, MC	650	12	6	5/12	–	
300-LD-2	Steels, W	SSJ, MC	300	2	2	7/12	–	8/12
300-LD-4	W	Disc 6D	300	2	2	TBD	–	
300-MD-1	Steels, W	SSJ, MC	300	7	4	7/12	–	
300-MD-2	W	Disc 6D	300	7	4	TBD	–	
500-LD-2	Steels, W	SSJ, MC	500	2	2	10/12	–	
500-LD-4	W	Disc 6D	500	2	2	TBD	–	
300-LD-3	Steels, W	SSJ, MC	300	2	2	7/12	–	11/12
300-HD-2	Steels, W	SSJ, MC	300	12	8	7/12	–	
500-LD-3	Steels, W	SSJ, MC	500	2	1	7/12	–	8/12
500-HD-4	Steels, W	SSJ, MC	500	12	6	7/12	–	
650-LD-3	Steels, W	SSJ, MC	650	2	2	10/12	–	
650-HD-3	Steels, W	SSJ, MC	650	12	8	7/12	–	
PC1	Various	SSJ, MC	80/100	0.02	HT	6/12	–	6/12
PC1A	Various	SSJ, MC	80/100	0.02	HT	6/12	–	6/12
PC2	Various	SSJ, MC	80/100	0.1	HT	6/12	–	6/12
PC2A	Various	SSJ, MC	80/100	0.1	HT	6/12	–	6/12
PC3	Various	SSJ, MC	80/100	0.5	HT	6/12	–	7/12
PC3A	Various	SSJ, MC	80/100	0.5	HT	6/12	–	7/12
PC4	Various	SSJ, MC	80/100	2	1	6/12	–	7/12

PC4A	Various	SSJ, MC	80/100	2	1	6/12	–	7/12
PC5	Various	SSJ, MC	80/100	20	9	6/12	–	
TB-300-1	Steels, W	SSJ, MC	300	0.02	HT	8/12	–	8/12
TB-300-2	Steels, W	SSJ, MC	300	0.1	HT	8/12	–	8/12
TB-300-3	Steels, W	SSJ, MC	300	0.5	HT	8/12	–	8/12
TB-300-4	Steels, W	SSJ, MC	300	7	5	7/12	–	
TB-500-1	Steels, W	SSJ, MC	500	0.1	HT	8/12	–	8/12
TB-500-2	Steels, W	SSJ, MC	500	0.5	HT	8/12	–	8/12
TB-500-3	Steels, W	SSJ, MC	500	7	4	7/12	–	
TB-650-1	Steels, W	SSJ, MC	650	0.1	HT	8/12	–	8/12
TB-650-2	Steels, W	SSJ, MC	650	0.5	HT	8/12	–	8/12
TB-650-3	Steels, W	SSJ, MC	650	7	5	7/12	–	
TB-650-4	Steels, W	SSJ, MC	650	20	11	7/12	–	
TTN09	SiC	Joint	500	3.4	2	8/11	–	11/11
TTN10	SiC	Joint	500	4.1	2	8/11	–	11/11
TTN11	SiC	Joint	800	4	2	3/12	–	5/12
TTN01	SiC	BSR	300	1	1	2/11	–	3/11
TTN02	SiC	BSR	300	10	6	2/11	–	12/11
TTN03	SiC	BSR	300	20	11	2/11	–	
TTN04	SiC	BSR	500	10	6	5/11	–	4/12
TTN05	SiC	BSR	500	20	11	5/11	–	
TTN06	SiC	BSR	800	10	6	5/11	–	4/12
TTN07	SiC	BSR	800	20	11	5/11	–	
TTN08	SiC	BSR	1200	10	6	5/11	–	8/12
TTN16	SiC	Fiber BSR	500	1	1	11/11	–	12/11
TTN17	SiC	Fiber BSR	500	10	6	8/11	–	6/12
TTN18	SiC	Fiber BSR	500	20	11	8/11	–	
TTN19	SiC	Fiber BSR	1200	1	1	3/12	–	4/12
TTN20	SiC	Fiber BSR	1200	10	6	3/12	–	11/12
Target zone rabbit capsules (US-TITAN-JAEA)								
T11-01J	V-4Cr-4Ti	BTC	425	2	1	11/12	–	12/12
T11-02J	V-4Cr-4Ti	BTC	425	6	3	1/13	–	
T11-03J	V-4Cr-4Ti	BTC	425	2	1	11/12	–	12/12
T11-04J	V-4Cr-4Ti	BTC	425	6	3	1/13	–	
T11-05J	SiC	BTC	600	2	1	11/12	–	12/12
T11-06J	SiC	BTC	600	6	3	1/13	–	
T11-08J	SiC	BTC	600	6	3	1/13	–	
T11-09J	SiC	BTC	600	2	1	11/12	–	12/12
T11-11J	SiC	BTC	600	2	1	11/12	–	12/12
T11-13J	Graphite	BTC	600	2	1	11/12	–	12/12
T11-14J	Graphite	BTC	600	6	3	1/13	–	
J12-01	F82H	BTC	300	1.5	1	1/13	–	
J12-02	F82H	BTC	300	6	3	5/13	–	
J12-03	F82H	BTC	300	1.5	1	5/13	–	
J12-04	F82H	BTC	300	6	3	1/13	–	

J12-05	F82H	BTC	300	1.5	1	1/13	–	
J12-06	F82H	BTC	300	6	3	5/13	–	

*T = Tensile, F = Fatigue, FT = Fracture Toughness, MC = Multipurpose Coupon, BSR = Bend Stress Relaxation Creep, DCT = Disc Compact Tension, BTC: Bellows-loaded Tensile Creep. Most experiments also contain TEM disks, other special purpose specimens, and monitors occupying small spaces.
**Hydraulic tube – fractional cycle exposures.